School of Engineering and Technology

Tennessee State University

Nashville, Tennessee 37203

Pulse Analysis

of

Acoustic Emission Signals

FINAL REPORT
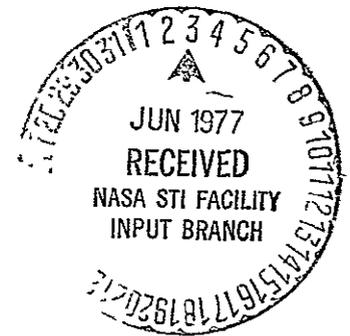
J. R. HOUGHTON, Principal Investigator
P. F. PACKMAN, Co-Principal Investigator

TENNESSEE STATE UNIVERSITY

NASHVILLE, TENNESSEE 37203

Department of Mechanical Engineering

May~~March~~ 24, 1977

NASA Scientific & Technical Information Facility
P. O. Box 8757
Baltimore/Washington International Airport
Baltimore, MD   21240

Dear Sir:

Please find enclosed three copies of the following reports

and publication that have been published under NASA Grant No.

NSG-8012:

A) Pulse Analysis of Acoustic Emission Signals, Final Report,
   J. R. Houghton and P. F. Packman.

B) "Optimal Design and Evaluation Criteria for Acoustic Emission
   Pulse Signature Analysis", by J. R. Houghton, P.F. Packman,
   M. A. Townsend, Journal of Acous. Soc. Am. March 1977.

C) "A Technique for the Deconvolution of the Pulse Shape of
   Acoustic Emission Signals Back to the Generating Defect Source'
   by J. R. Houghton, P. F. Packman and M.A. Townsend, Proceedings
   of Eighth World Conference on Nondestructive Testing. Sept.
   1976.

Sincerely yours,
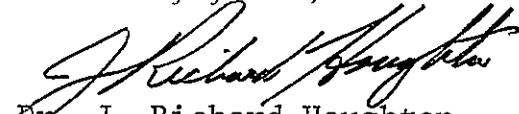
Dr. J. Richard Houghton,
Assistant Professor

SCHOOL OF ENGINEERING AND TECHNOLOGY

TENNESSEE STATE UNIVERSITY

Nashville, Tennessee   37203

PULSE ANALYSIS OF ACOUSTIC EMISSION SIGNALS

Final Report

June 1, 1974 to May 31, 1976

.NASA Grant No. NSG 8012

J. R. Houghton, Principal Investigator

P. F. Packman, CO-Principal Investigator

Date: February 1977

PULSE ANALYSIS OF ACOUSTIC EMISSION SIGNALS

J. R. Houghton and P. F. Packman

ABSTRACT

A method for the signature analysis of pulses in the frequency
domain and the time domain is presented. Fourier spectrum, Fourier
transfer function, shock spectrum and shock spectrum ratio were
examined in the frequency domain analysis and pulse shape deconvo-
lution was developed for use in the time domain analysis. Comparisons
of the relative performance of each analysis technique are made for
the characterization of acoustic emission pusles recorded by a
measuring system. To demonstrate the relative sensitivity of each of
the methods to small changes in the pulse shape, signatures of com-
puter modeled systems with analytical pulses are presented. Opti-
mization techniques are developed and used to indicate the best
design parameters values for deconvolution of the pulse shape.
Several experiments are presented that test the pulse signature
analysis methods on different acoustic emission sources. These in-
clude acoustic emissions associated with: a) crack propagation, b)
ball dropping on a plate, c) spark discharge and d) defective and
good ball bearings. Deconvolution of the first few micro-seconds
of the pulse train are shown to be the region in which the signifi-
cant signatures of the acoustic emission event are to be found.

ACKNOWLEDMENTS

TABLE OF CONTENTS

LIST OF TABLES

LIST OF FIGURES

CHAPTER I

INTRODUCTION

Nondestructive Testing

Nondestructive testing has been one of the most rapidly growing technical fields. Increasingly, design engineers are specifying nondestructive evaluations of elements and are accepting the additional cost of nondestructive testing (NDT) particularly where there is danger to a structure of fatigue stress, stress corrosion or catastrophic crack growth. Fracture critical analysis of designs is an important area of attention at NASA, in the armed forces, and in the nuclear power industry. A fracture critical component is one where premature failure would result in loss of the total structure or shut-down of the total system. These components must be designed and verified safe by two different design processes: standard design and fracture mechanics design procedures. An interest in improving the sensitivity, reliability and ease of nondestructive testing methods accompanies the growth of fracture critical analysis in designs (1).

Acoustic emission techniques are relatively new in the field of nondestructive testing and promise to be among the most reliable techniques for in situ determination of structural integrity. Following is a summary of the most

1

important techniques of nondestructive testing, including
their methods and their limitations.

X-ray photography

This method utilizes electromagnetic radiation trans-
mission through the test piece. The resolution for detection
of a crack or void is limited by: 1) the grain size of the
x-ray film, 2) the orientation of the crack relative to the
x-ray film plane, and 3) the thickness of the material
through which the x-rays pass. The sensitivity limit of
crack detection is approximately 3 mm. The 90 percent prob-
ability of detection with a 95 percent confidence level
(90/95 limit) is a 12 mm crack length (2).

Dye penetrants

This method is used primarily for surface crack detec-
tion by applying a penetrating dye solution, wiping the ex-
cess off the surface, and then applying a developer solution
to draw the penetrating dye from the defect. The sensitivity
of this NDT method varies with the crack length, 2C, and the
crack depth, a. For an a/2C ratio of 0.5, the detectable
limit is on the order of a 2 mm crack length and the 90/95
limit is 4 mm.

Eddy currents

Eddy current methods detect flaws by permeability
changes on the surface and in the near subsurface. The
field of view is less than given by both the x-ray and

dye methods; it is limited to the diameter of the field pro-
jected by the detector. The detectable limit of void length
is approximately 1 mm and the 90/95 limit is a 3 mm void
length.

Ultrasonic detection

This method of detecting flaws uses a high frequency
pressure radiation transmitted into the test piece. The
radiation may be received by the transducer as through
transmission or as reflected transmission. The flaws are
detected either by a loss of energy with respect to the
energy received on either side of the flawed area or by the
reflected energy. The detectable limit of cracks is 1 mm
and the 90/95 limit is approximately 2 mm.

Magnetized particles

A solution with a finely dispersed suspension of mag-
netic particles is used to detect surface flaws and near
subsurface flaws. The solution is poured over the surface
and a magnetizing field is applied to the specimen. At a
flaw location, there will be a perturbation of the flux lines
and the particles in solution will gather around the pertur-
bation. The detectable limit of cracks is approximately
1 mm and the 90/95 limit is 2 mm.

Acoustic emission

The acoustic emission (AE) method of NDT is used to
detect high frequency pressure waves emitted by the growing

defects. This method has been used to locate the area where a crack is growing, but it has not been used to estimate the crack size. The sum of the acoustic emission bursts and the time rate of the emissions has been correlated with crack growth rate in many materials. The AE signals from crack growth have been associated with dislocation movement as the plastic zone is growing and is on the order of 2 to 60 x 10^{-6} mm. A 90/95 limit has not been established for the ability of this method to locate cracks. Location of cracks within ± one wall thickness of a pressure vessel has been reported from overload proof tests (3).

There are several reasons why AE measurements are preferable over other types of NDT tests. The AE signals are detectable in both the working situation and during the periodic proof testing. Also, the signals can be detected remotely from the growing crack by using an array of transducers. Thus costly disassembly is deferred or even avoided until it is necessary to view the defect directly with other NDT tools. Additional reasons for selecting AE measurements are the low cost of the equipment and results are immediately available at the time of testing. Because of the potential for this particular type of inspection, this study concentrates on the AE method for flaw characterization.

Background of Acoustic Emission Research

Researchers are continually developing new methods
for increasing the range of application of acoustic emission,
e.g., in 'the fields of flaw detection, indirect mechanical
measurement of flow and monitoring the performance of rotat-
ing equipment. Present acoustic emission emphasis has been
directed toward the understanding of pulses generated during
the propagation of material defects. The equipment, elec-
tronic techniques, and associated science can easily be ex-
tended to the study of acoustic pulses produced by other
types of generating mechanisms, such as rotating equipment
and wearing surfaces.

It has been established by prior research that acoustic
emissions result from slip-produced pressure waves during
dynamic processes within a material. In other words, the
acoustic emission is a transient elastic wave generated by
the rapid release of energy within the material from a local-
ized source.

The first serious investigation of the acoustic
emission phenomenon was performed by Kaiser (4). In 1950
he reported the results of his study on several metals, all
of which exhibited the acoustic emission phenomenon upon
loading. He attributed the acoustic emissions emanating from
polycrystalline specimens to slip originating in the grain
boundary interface. Stresses in the specimens were believed
to cause interactions at the interfaces of adjacent grains,

resulting in the emissions. He also observed that the frequency and amplitude of the emissions had characteristic spectra and were related to the stress level for a given material.

Investigation of the acoustic emission phenomenon in the USA was begun by Schofield (5,6) who did extensive research in the area of deformation mechanisms as sources of emissions after 1955. Schofield did most of his work on single crystals which were good producers of acoustic emissions. Numerous sources of acoustic emission in metals have subsequently been identified. Table 1 lists typical material factors that influence acoustic emission generation. Studies also indicate that there are no simple characteristic spectra of frequency and amplitude emitted for a material, and that these were not the important parameters to be used for study of a material.

Recently, studies have been conducted to again analyze the frequency spectra of acoustic emissions in metals and nonmetals (7-11). Beattie (11) suggests that the acoustic pulse contains much more information than has been extracted by conventional ring-down count analysis and that more refined signal processing techniques can be applied to the pulse to obtain additional information about the nature of the signal.

In a recent special publication by the Acoustic Emission Working Group, ASTM-STP 505, many authors presented

TABLE 1

FACTORS THAT INFLUENCE ACOUSTIC EMISSION GENERATION

Higher Amplitude AE Pulses	Lower Amplitude AE Pulses
Large grain size	Small grain size
Cleavage fracture	Shear deformation
Anisotropy	Isotropy
Flawed material	Unflawed material
Thick section	Thin section
Twinning material	Nontwinning material
Martensitic phase transformations	Diffusion controlled transformations
Low temperature	High temperature
High strength	Low strength
High strain rate	Low strain rate

state-of-the-art papers covering applications of acoustic
emission (12). The transient stress waves generated by the
rapid release of energy within a material have been applied
to fundamental studies of the deformation of materials, mate-
rial evaluation, nondestructive testing, and evaluation of
structural integrity. Modern instrumentation, electronics,
and data processing techniques have overcome many of the dif-
ficulties encountered in the past so that it is no longer
necessary to isolate the mechanical loading system from the
specimens under study to obtain the significant AE signals.

Present AE measurement systems

In order to understand and identify the pulses gener-
ated by defects in materials and to associate the pulses with
specific phenomena within the material, an analysis of the
acoustic signal must be performed. Usually this analysis is
approached from one of two directions: signal (or pulse)
counting or signature (or frequency) analysis.

Signal counting. Much of the research today in acous-
tic emission non-destructive testing is in counting pulses
emanating from a source undergoing plastic deformation (3).
All pulses whose amplitude is greater than some preselected
baseline noise signal level are counted as a function of
time. Either the total number of pulses or the pulse rate
is used as one variable, and stress or strain and/or some
other mechanical variable are recorded on an X-Y-Y recorder

to get a characteristic curve. A family of characteristic curves is collected and judged for the influence of the variable under investigation, such as load or specimen geometry.

Liptai (3) has given a very useful summary of AE techniques using pulse counting for materials examination. For unflawed specimens of beryllium in a creep test, the following relation has been found between the AE count rate, N, time, t, and steady state applied stress, σ:

$$N = D\ t^M\ exp^{B\sigma} \tag{1}$$

where D, M and B are constants.

AE pulse counting has been shown to be useful for the detection of growing cracks. Flaws and cracks act as stress concentration zones, and plastic deformation will occur before the average stress reaches the yield stress. In fracture mechanics theory it has been demonstrated that the stresses near the tip of a crack in an idealized solid are completely controlled by a stress intensity factor K.

$$K = \sigma\ \sqrt{\pi a} \tag{2}$$

where σ equals applied stress and 2a is the crack length, i.e., central type of crack in infinite plate. Thus experiments have been conducted to define the dependence of the acoustic emissions generated in the plastic zone of a crack tip and K. The relation found is:

$$\Sigma N = C\ K^A \tag{3}$$

where ΣN is the total number of counts, and C and A are constants. The exponent A varies from 4 for 7075-T6 aluminum specimens (13) to approximately 8 for beryllium (14).

There are many other examples where AE pulse counting is being applied in research on materials failure. In the bulk of this work the variables ΣN and $\dot{N}$ are measured and correlated with a physical measurement such as creep, corrosion, crack growth, etc.

Signature analysis. In this procedure, the total available frequency range of the signals is examined. Specific frequency peaks are analyzed, after their preprocessing (filtering and shaping) and their storage on a magnetic tape. A 'typical' frequency of the generating process is sought, which can then be used for future identification.

Graham and Alers (8) developed an experiment for the analysis of a single AE burst from a growing defect in metal. The frequency signature from 0 to 2 mHz of a burst was computed and found to be similar to acoustic 'white noise' with slight perturbations from pulse to pulse. They reported differences in signatures between tensile crack growth, stress-corrosion induced crack growth, and plastic flow.

Frequency analysis techniques used for signal identification and signature analysis present several fundamental problems. There are two major sources of misinterpretation: 1) the frequency response of the transducer and 2) frequency shifts and mode conversion within the geometry of the

structure. It is therefore important to consider alternative methods of signal analysis. In particular, a signature analysis that models the nature of the pulse in the time domain is desirable.

One powerful technique for signature analysis is called pulse testing (15). In this process Fourier transfer functions are developed from the Fourier transforms of both the input amplitude (disturbance source) and the output amplitude of the measured signal. If the transducer transfer function could be described adequately, it is anticipated that noise and errors produced by the measuring system and external generators could be minimized.

The Present Study

This dissertation is an investigation of acoustic emission (AE) measurement methods for use in nondestructive evaluation. The primary objective is to develop a technique for examining AE pulses which could reliably discriminate between AE pulses from noncritical sources and AE pulses from a growing crack.

Different methods for analyzing individual pulses by examination of signatures in the frequency domain and in the time domain are developed and examined. The time domain signature uses a deconvolution method which effectively removes the dynamic contributions of the transducer measurement system.

This study also investigates the ideal characteristics for a transducer and filter measurement system. The optimum coefficients for the AE system described were not tested experimentally because 1) the means for manufacturing an optimum transducer are not available and 2) the results obtained with the deconvolution method appear to minimize the need to optimize the system for this study.

Experimental tests were conducted and the results from the different AE pulses examined. Mathematical models for the components of the measuring system are presented in the equation form and in a Bode frequency plot. Four experiments were conducted to:

1. evaluate the reproduceability of the pulse recordings

2. test the relative performance of different transducers

3. test the ability of one transducer to distinguish between different AE sources, and

4. test the performance of an AE transducer on a ball bearing test rig for bearings with and without defects.

The following chapters present the analysis, findings and conclusions of this study. Suggestions for further research and improvements in the deconvolution method of AE measurement are also presented.

CHAPTER II

ASSESSMENT OF PULSE ANALYSIS METHODS

Introduction

The principal methods for analysis and evaluation of acoustic emission stress waves are the following: 1) frequency spectrum, 2) total number of acoustic emission counts from a transducer ringdown, 3) count rate, 4) amplitude distribution and 5) rise time of initial burst.

The count rate and the total number of counts are the most widely used. They have been correlated with stress intensity factors, applied stress, number of fatigue cycles, and applied strain (12). The present state of the analysis of acoustic emission signals similar to the one shown in Figures 1 and 2 has been primarily in the area of simple signal statistics such as the number of pulses above a given pulse amplitude.

Several of the available methods for dealing with pulse analysis have been tested for their relative sensitivity in distinguishing between different types of pulses. The work reported in this chapter is a theoretical analysis of the pulse analysis methods with idealized geometrical pulses substituted for actual test pulses. The study described herein was conducted to find an analysis method selective
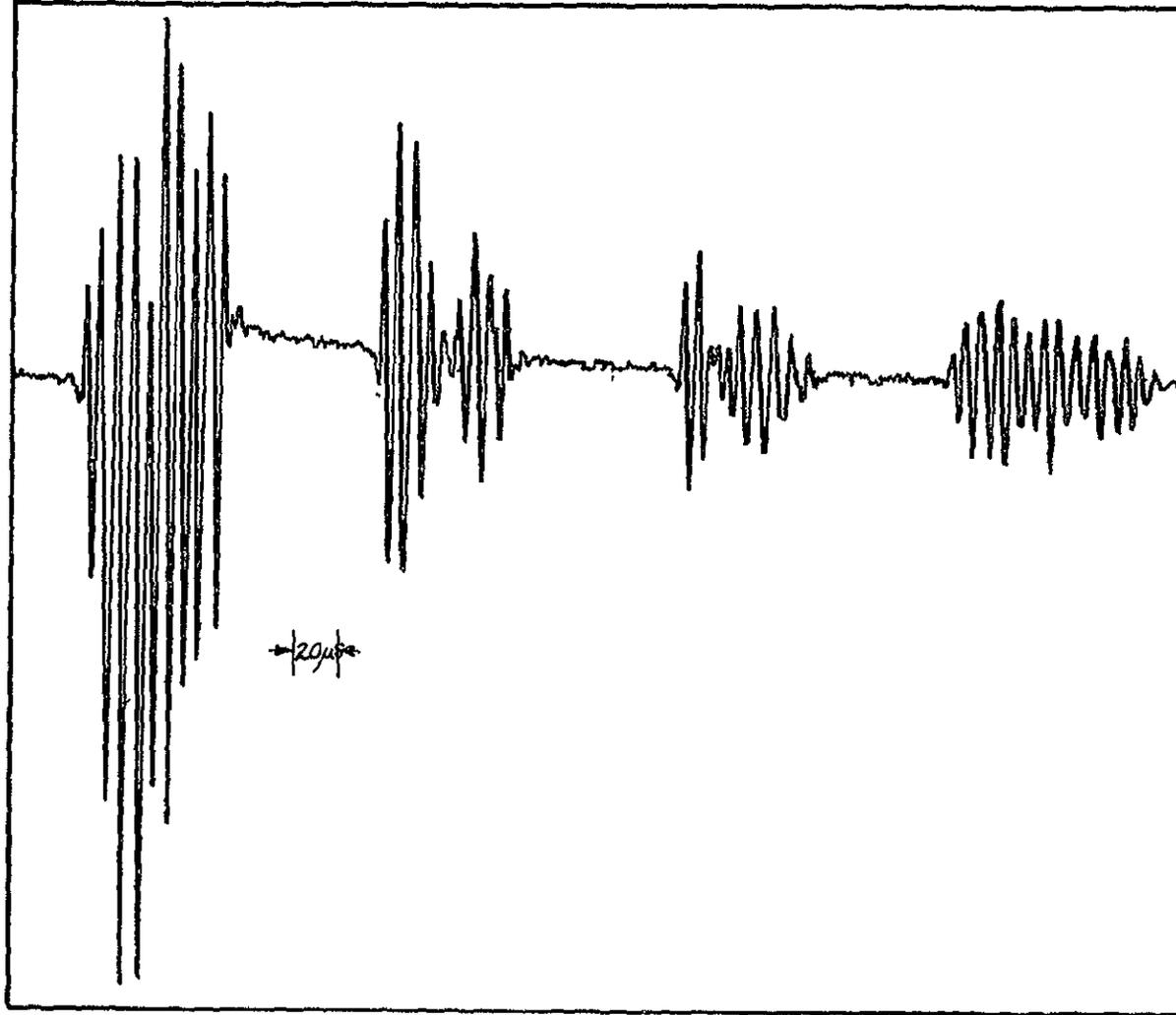
Fig. 1.   Acoustic emission pulse from ball bearing rig.
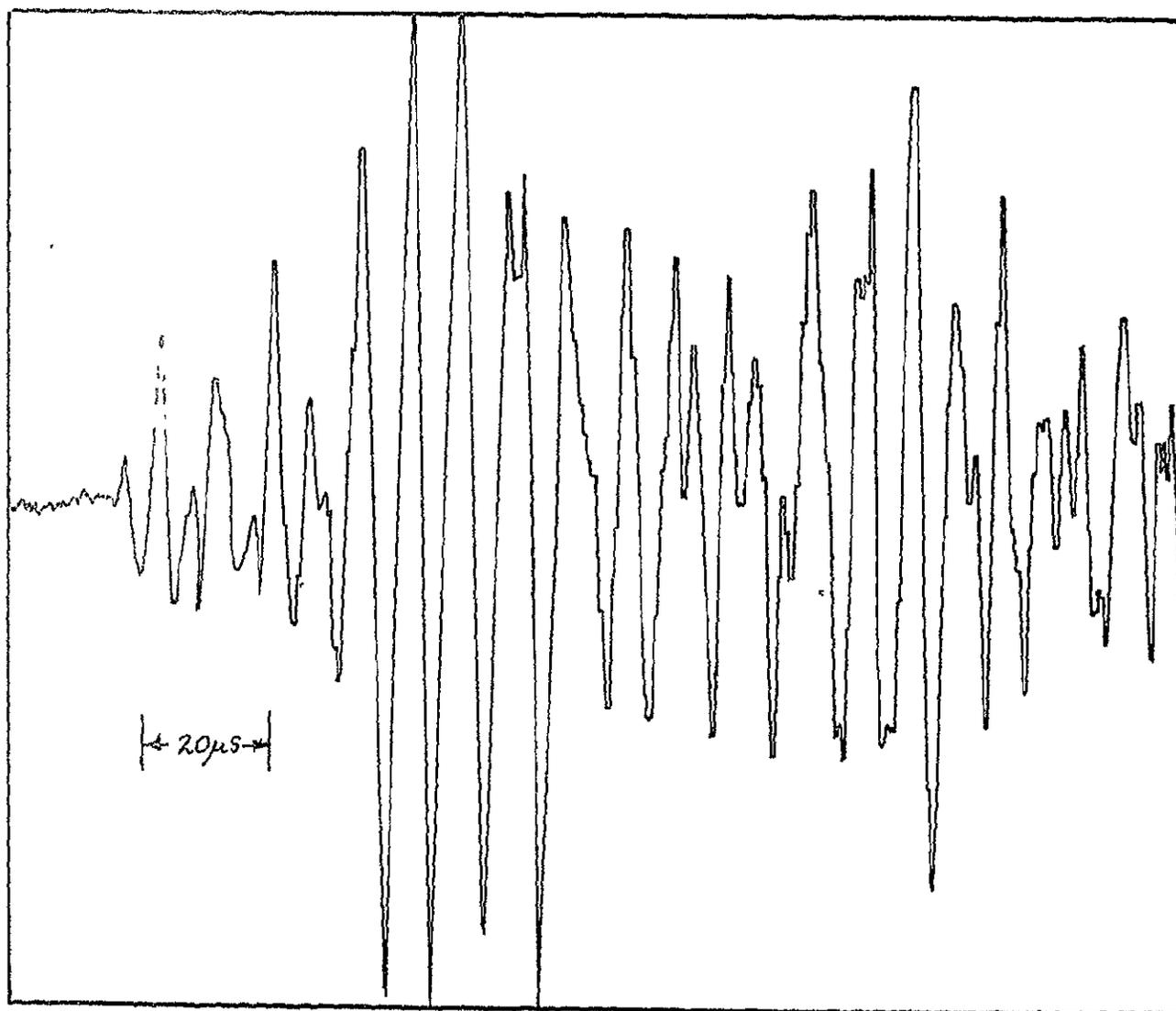
Fig. 2. Acoustic emission pulse from electrical spark.

enough to distinguish between separate acoustic emissions associated with 1) an actively growing crack and 2) extraneous signals of short duration.

A phase of this study was initiated to determine how effective the available pulse analysis methods are in segregating pulses of different types after they have passed through an acoustic emission transducer and filter measurement system. Since no adequate model was available to describe the dynamic behavior of an acoustic emission pickup, a simple single-degree-of-freedom model of an accelerometer was used for the computer model. Filters in the measuring system are modeled as a single-pole passive high-pass filter and low-pass filter. The system is shown in Figure 3.

The pulse shapes, which any pulse analysis methods must deal with, were considered to be 1) large changes in the shape as represented by a triangle, square, and displaced cosine pulse as well as 2) small perturbations on the profile of a large pulse. The criteria for judging the accuracy of each pulse analysis method is how well each method identified differences in pulse shapes.

The pulse analysis techniques tested on a triangular pulse with small perturbations are: 1) Fourier spectrum; 2) Fourier transfer function; 3) shock spectrum; 4) shock spectrum ratio.

The influence of the measuring system on the pulse analysis was tested with three different analytical pulses:
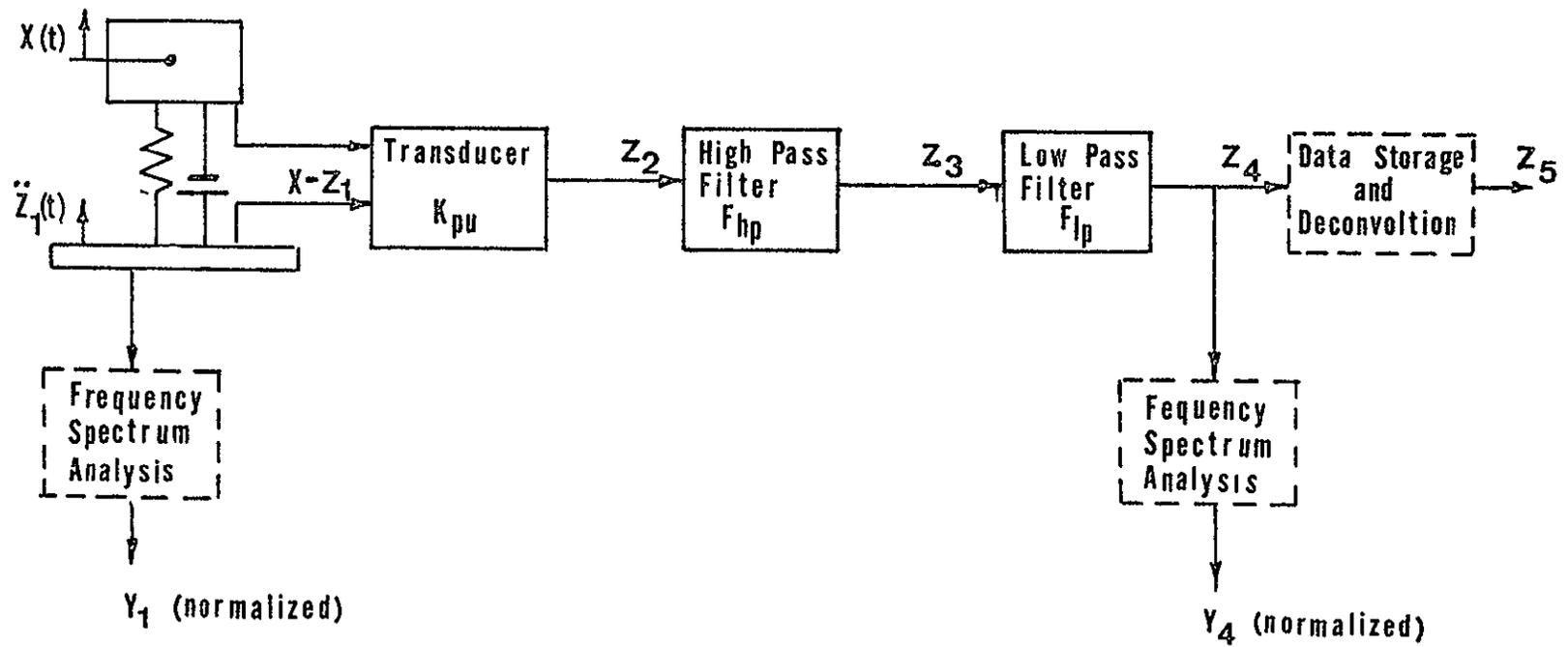
Fig. 3. Schematic diagram of transducer, filter, and recording system.

displaced cosine, square and triangle. Fourier spectrum was used to analyze the pulse at different locations in the measuring system. Several deconvolution methods were also used.

Spectrum Analysis Methods

Four techniques follow for signature analysis performed in the frequency domain. Signature analysis in the time domain are rise-time analysis and deconvolution. Rise-time analysis is simply a study of the shape of the leading edge of a pulse. Deconvolution is described later in this chapter.

Fourier spectrum

The Fourier transform of a pulse is the most common means for characterization of a signature in both destructive and nondestructive testing. The transform of a signal, f(t), into the frequency domain as F(jω) is:

$$F(j\omega) = \int_0^\infty f(t) \ \exp(-j\omega t) \ dt \qquad (4)$$

where ω equals frequency, rad/s and j equals the square root of minus one. The advantage of this frequency transform is that it can treat one unique pulse. A requirement in using this transform is that the detector of the pulse not exhibit transient decay during the period of the pulse measurement. When there is a transient decay problem in the measurement system, then the Laplace transform equation is used.

Samples of the Fourier spectra that are generated by a square pulse of duration T_p are shown in Figure 4(a). Figure 4(b) is a typical experimental frequency signature of an actual short duration shock measured with an accelerometer transducer.

To permit rapid visual comparison of pulses, the following normalization process was used.

1. When the pulse width is clearly defined, the frequency scale was normalized by multiplication of each frequency (F) by the pulse width in seconds (T_p).

2. The Fourier spectrum magnitudes (Y) were normalized with respect to the size of the pulse by division of the Fourier magnitude by the absolute value of the area between the pulse and the zero line.

3. The shock spectrum magnitudes were normalized by division by the maximum value of the pulse.

A variety of test computations were conducted on pulses of similar shape but with different heights and pulse widths. For a particular pulse, whether it be a symmetrical triangle, an unsymmetrical triangle or a rectangle, the signatures are always the same without regard to the pulse height or pulse width when the above normalization procedure is used.

Figure 5 presents the Fourier spectrum for a simple triangular pulse and for a triangular pulse with a 17% perturbation on the trailing side of the pulse. The sensitivity of the Fourier analysis technique to distinguish between the square pulse and the triangular pulse is relatively high, but the technique does not deal effectively with the presence of
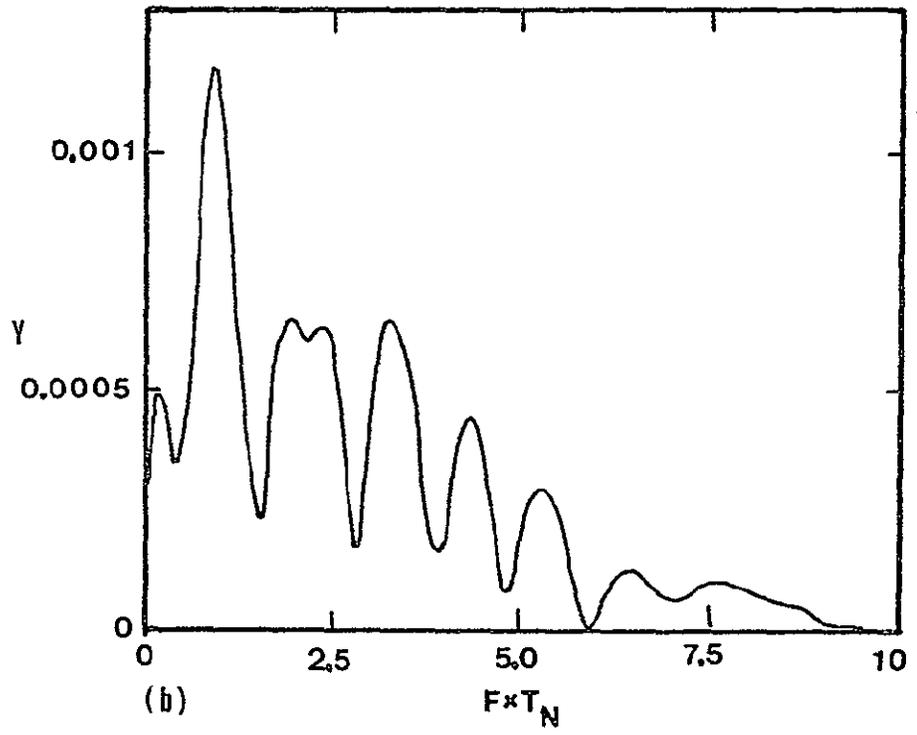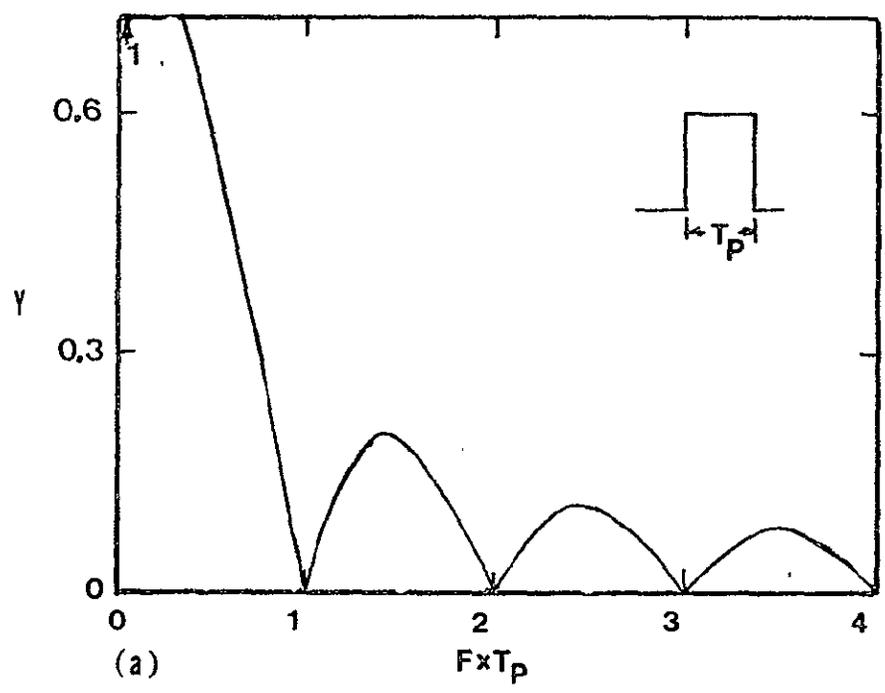
Fig. 4. Fourier spectrum of two pulses: a) square
pulse input and b) unknown AE pulse input.
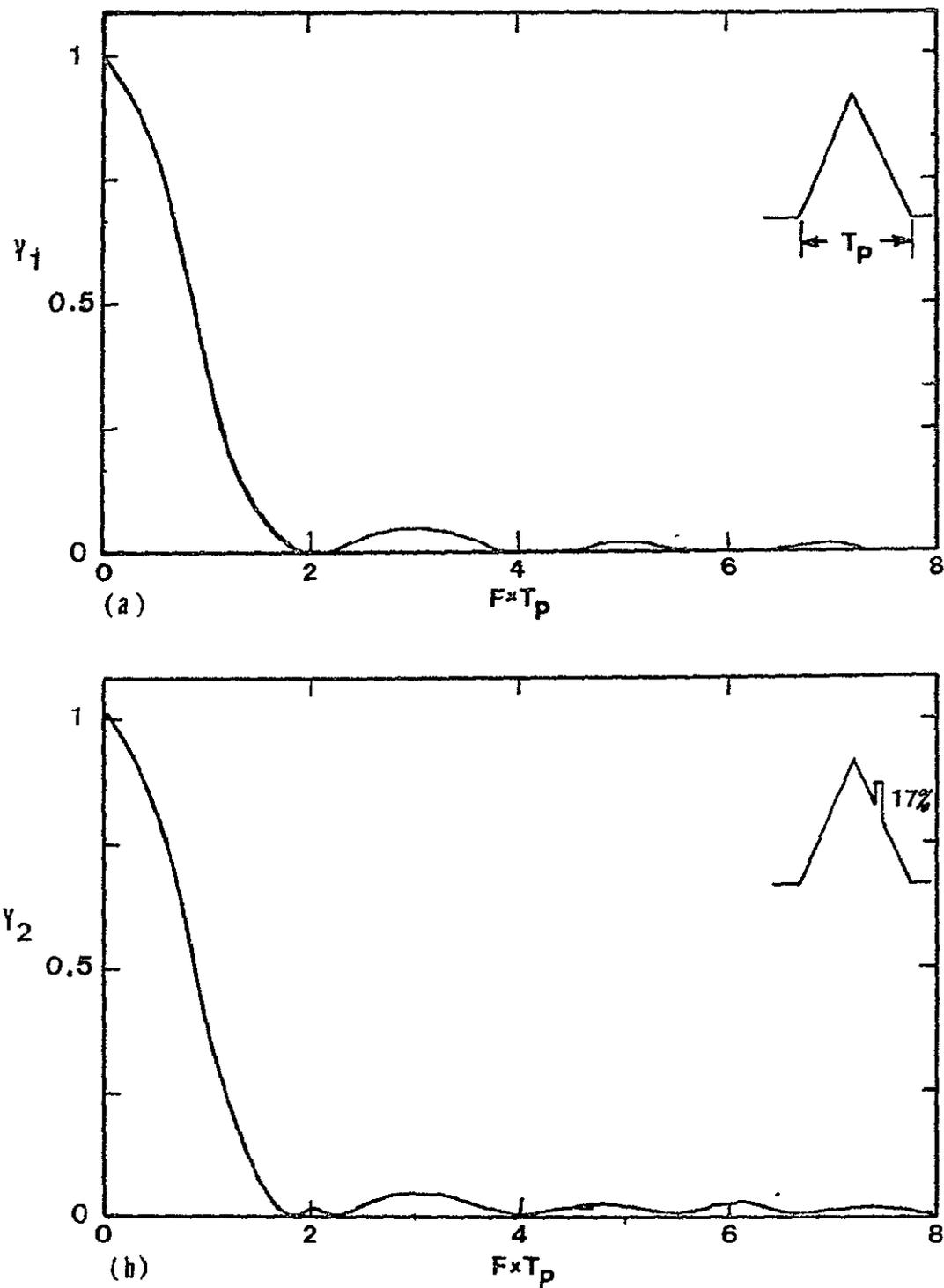
Fig. 5. a) Fourier spectrum for triangular pulse and
b) triangular pulse with a 17% perturbation on trailing edge
of pulse.

a small perturbation. The only significant shifts are at the null magnitude frequency $FxT_p = 2$, 4 and 6 where small amplitude signals are present in the perturbated frequency spectrum. It is probable that small amplitude signal differences such as this could be masked by system noise.

Fourier transfer function spectrum

A transfer function is defined as a mathematical relationship that relates the output signal to the input signal of a system and presumes a linear relationship $\theta = GI$. When an experimental output variable can be measured for a known input variable, it is then possible to derive an approximate transfer function that is representative of the system. This approach to pulse measurement situations was suggested by Clements and Schnelle (15), and has been used on a number of nondestructive testing projects (16, 17). The equation that is used for derivation of a Fourier transfer function is as follows:

$$G(j\omega) = \frac{\int_{o}^{\infty} f(t)_{out} \cdot \exp(-j\omega t)dt}{\int_{o}^{\infty} f(t)_{in} \exp(-j\omega t)dt} \qquad (5)$$

Samples of the magnitude of the Fourier transfer function as a function of frequency are shown in the plots of Figure 6. The output signal is a triangular pulse with a 2% perturbation of the peak height on the leading edge for the top plot, and a triangular pulse with two perturbations for

the lower plot. The input signal in both cases was a tri-angular pulse.

The signature analysis method demonstrates high sensitivity for detection of these small perturbations. If the input and output signal are identical, the transfer function is a straight horizontal line of magnitude 1. The straight horizontal portions of the plots in Figure 6 are in the frequency ranges where there was a significant magnitude shown on the Fourier spectrum plots of Figure 5. Thus the transfer function is shown to amplify differences in y_1 and y_2 at FxT_p of 2, 4 and 6 which is where y_1 and y_2 are quite small.

The two plots of Figure 6 show the influence of the location and number of perturbations on the main pulse by Fourier transfer function analysis. For the example given, the second minimum of the Fourier spectrum at $FxT_p = 4$ appears to be the most sensitive to small changes. No analysis has been made that would predict this behavior. The Fourier transfer function signature is altered significantly when the height of the perturbation is increased from 2 to 15%.

Shock spectrum

A shock spectrum is defined as follows (18).

The application of an acceleration shock pulse to the base of a single-degree-of-freedom vibration system results in a time response of the mass. The maximum value of the time response for a given pulse shape depends on the natural frequency and the damping of the vibrating system. The plot of the maximum response of the oscillator against the natural frequency of the oscillator is the shock spectrum of the pulse.
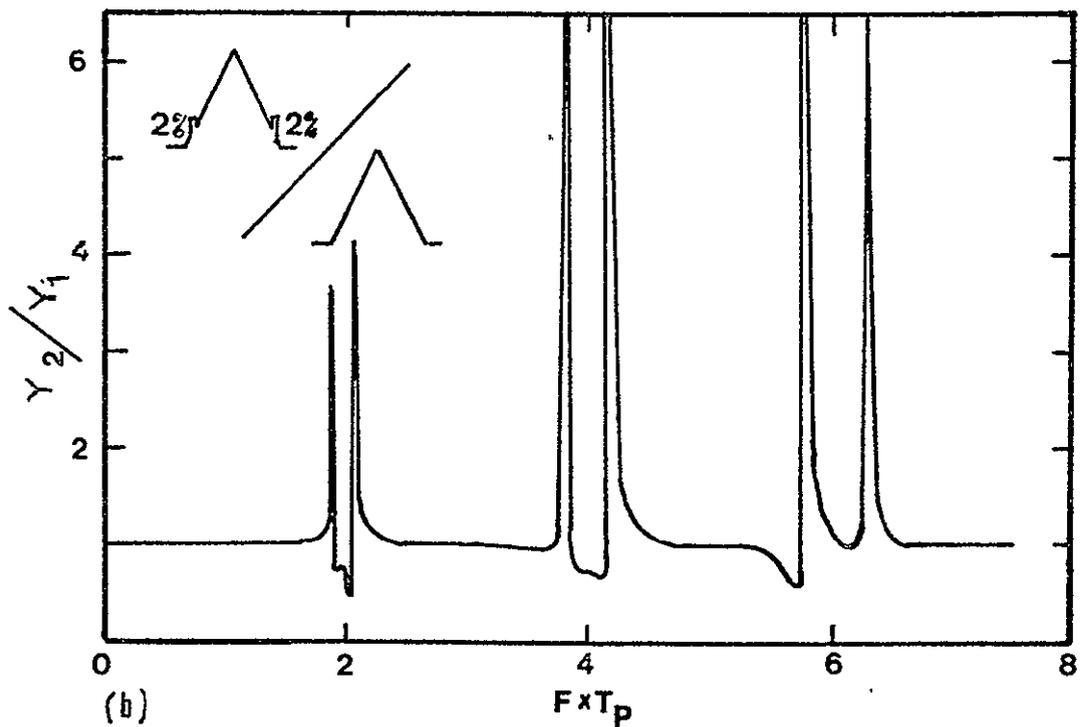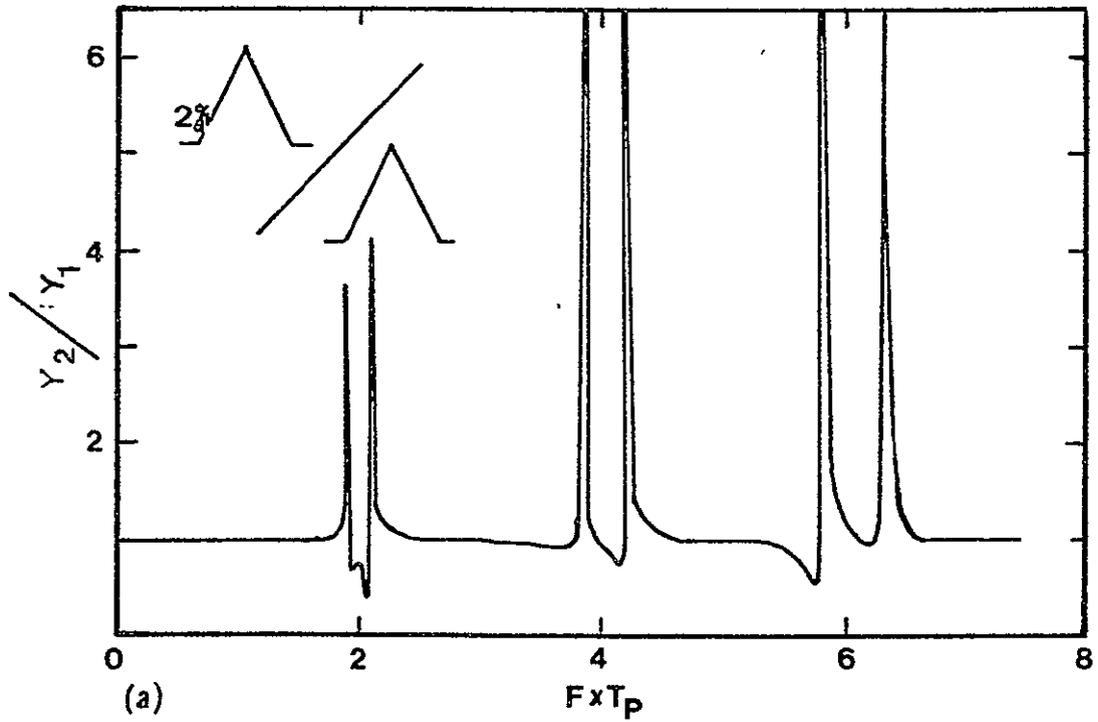
Fig. 6. Transfer function in frequency domain for two
pulses each with different perturbation relative to a simple
pulse: a) 2% perturbation on leading edge of pulse and b)
2% perturbation on both edges of pulse.

The equation of an undamped system initially at rest is:

$$(x-Z)_{max} = \left[-\frac{1}{\omega} \int_0^t \ddot{Z}(\xi) \sin \omega(t-\xi) \, d\xi \right]_{max} \qquad (6)$$

The relative displacement between oscillator mass and the base for a shock input is normally calculated by Duhamel's integral for linear systems (18). A pseudo-relative acceleration is then found by multiplying the displacement by (natural frequency)^2. An improvement on the Duhamel's integral approach has been developed recently (19) where the differential equation of motion is solved directly for the particular pulse input using the Runge-Kutta-Nystrom method (20). One of the advantages of the Runge-Kutta shock spectrum is that the relative acceleration peak values are found directly and different damping models may be used. The Runge-Kutta method is similar to setting up the differential equation on an analog computer and picking off the peak amplitude at each natural frequency selected in the frequency band for the spectrum.

The shock spectrum was derived for a damping ratio of 0.0001. The resultant shock spectrum for a triangular-shaped acceleration pulse and the spectrum for a triangular pulse with a 5% perturbation are shown in Figure 7. This method of representation of a pulse signature shows only a slight change in shape between the two pulses for frequencies above $FxT_p = 3$. Other perturbations resulted in only minimal differences in shock spectrum, and it was concluded that the
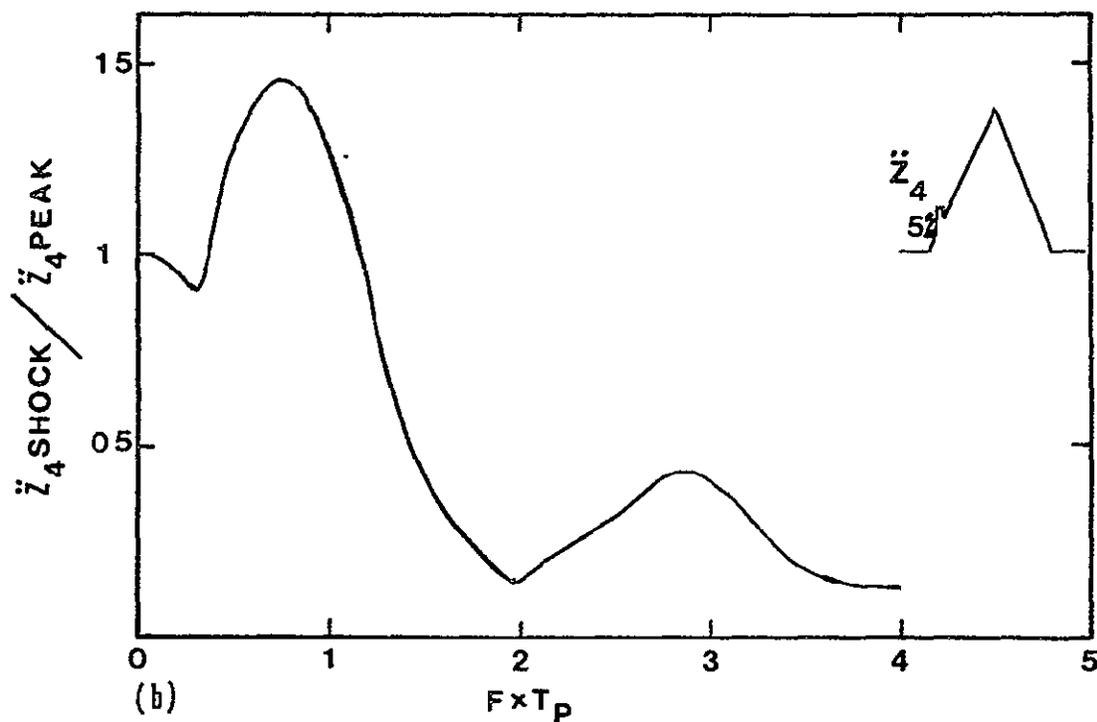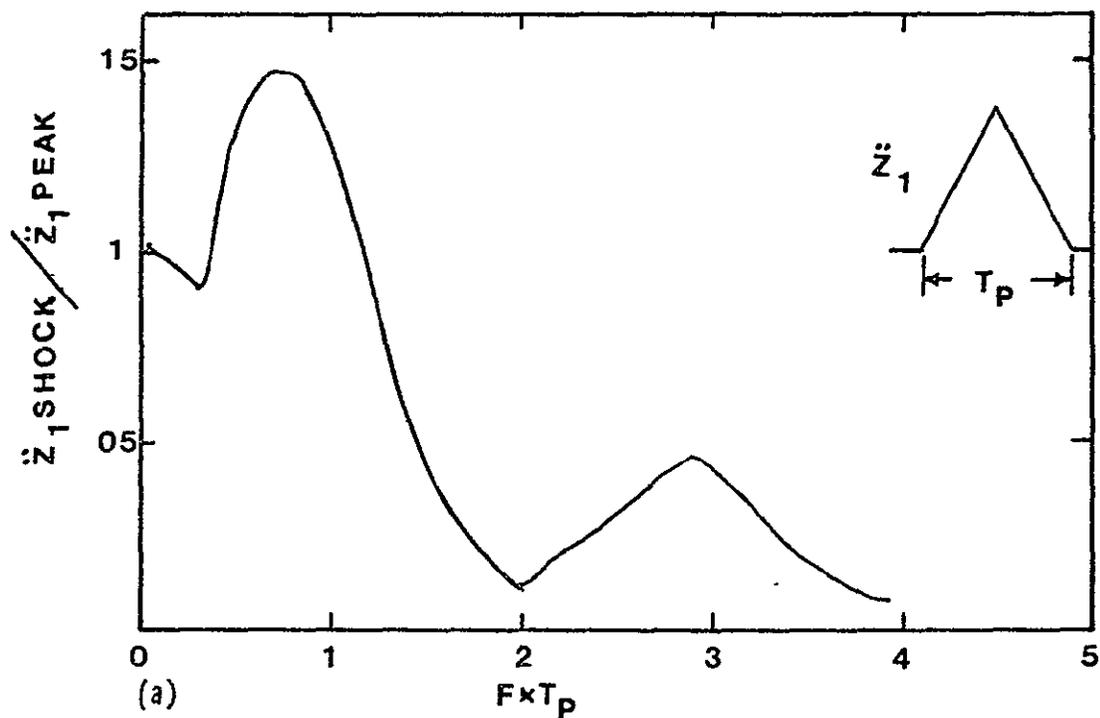
Fig. 7. Shock spectrum of relative motion for triangular pulse and triangular pulse with a 5% perturbation (damping ratio = 0.0001).

shock spectrum signature does not produce an improvement on the Fourier spectrum signature.

Shock spectrum ratio

Following the approach suggested by the Fourier transfer function method, a pseudo-transfer function was derived by dividing the shock spectrum of the output function by the shock spectrum of the input function as shown in Figure 8. A sketch of the shape of the acceleration pulses used and their relative positions in the ratio is shown in the upper left corner of each plot. It is apparent from the plots that the shock spectrum ratio is sensitive to a small perturbation and when more than one perturbation is present the plot is significantly different. An advantage of this method for signature derivation is seen in the broad peak and low magnitude of the deviation, i.e., from 1.0 to 1.6, as contrasted with the sharp peaks over a narrow frequency band for the Fourier transfer function seen in Figure 6. Also, note for $FxT_p = 2$ and 4 where the shock spectrum is low (Figure 7), that the shock spectrum ratio plots (Figure 8) is a well-behaved function.

One application of the Fourier transfer function and the shock spectrum ratio signatures is the definition by size and location of the perturbation on a larger pulse. A series of five test computations for different perturbation heights at the same location on a triangular pulse are shown
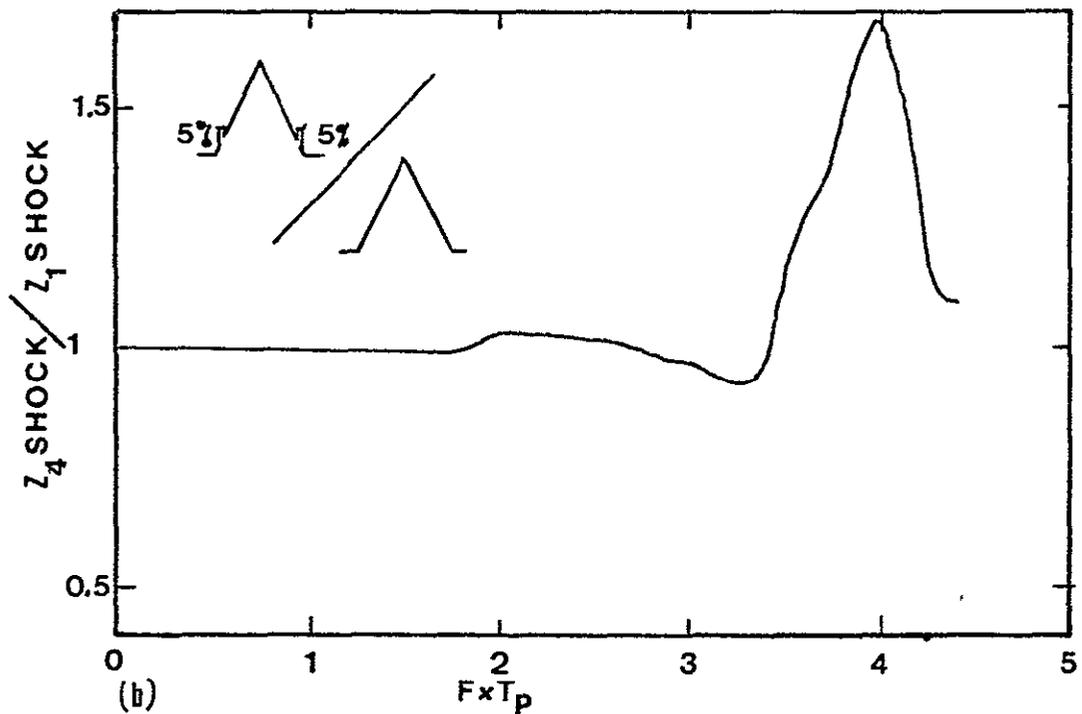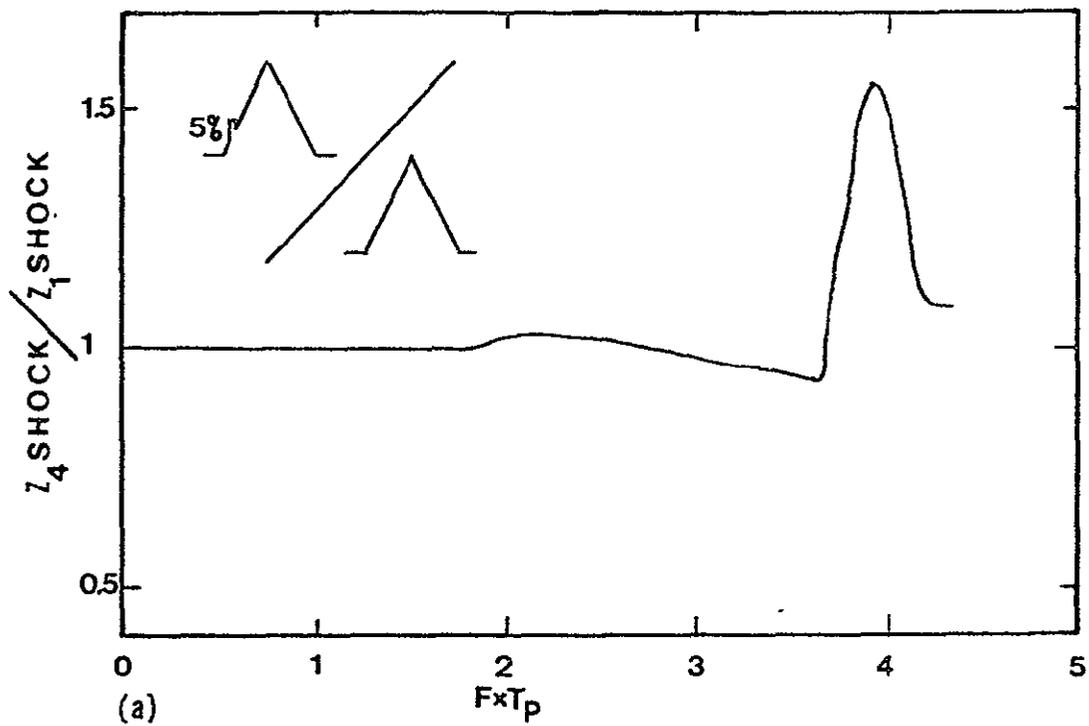
Fig. 8. Ratio of shock spectrums for two pulses relative to a simple pulse: a) 5% perturbation in leading edge of pulse and b) 5% perturbation on both edges of pulse.

in Figures 9 and 10. The highest peak with the Fourier transfer function, Figure 9, occurred at $FxT_p = 4.5$, and the peak decreased as the perturbation height increased. The changes in the peak height with perturbation height was not linear. The peak seen at $FxT_p = 2.0$ did increase linearly with perturbation height. The shock spectrum ratio results, Figure 10, showed a peak at $FxT_p = 2$ and 4. These peaks increased linearly with the perturbation height. The shock spectrum ratio results are considered to be more useful for the analysis of perturbations. Five additional computations were made with the 15% perturbation moved across the width of the pulse from 7.5 to 17.5% of T_p. The results are shown in Figure 11 and it appears that the features of the signature above $FxT_p = 2.3$ are influenced significantly by the location of the pulse.

Influence of the Transducer on Pulse Shape Analysis

Graham and Alers (9) have determined the frequency spectrum of AE pulses. Their results suggested that it was possible to detect variations in the pulse shape for pulses from different acoustic emission sources, but the frequency spectrum approach is hampered by an inability to classify how much the original acoustic signature was modified by filtering and attenuation in the measurement system. Typical charactistics of commerically available AE transducers are as follows.
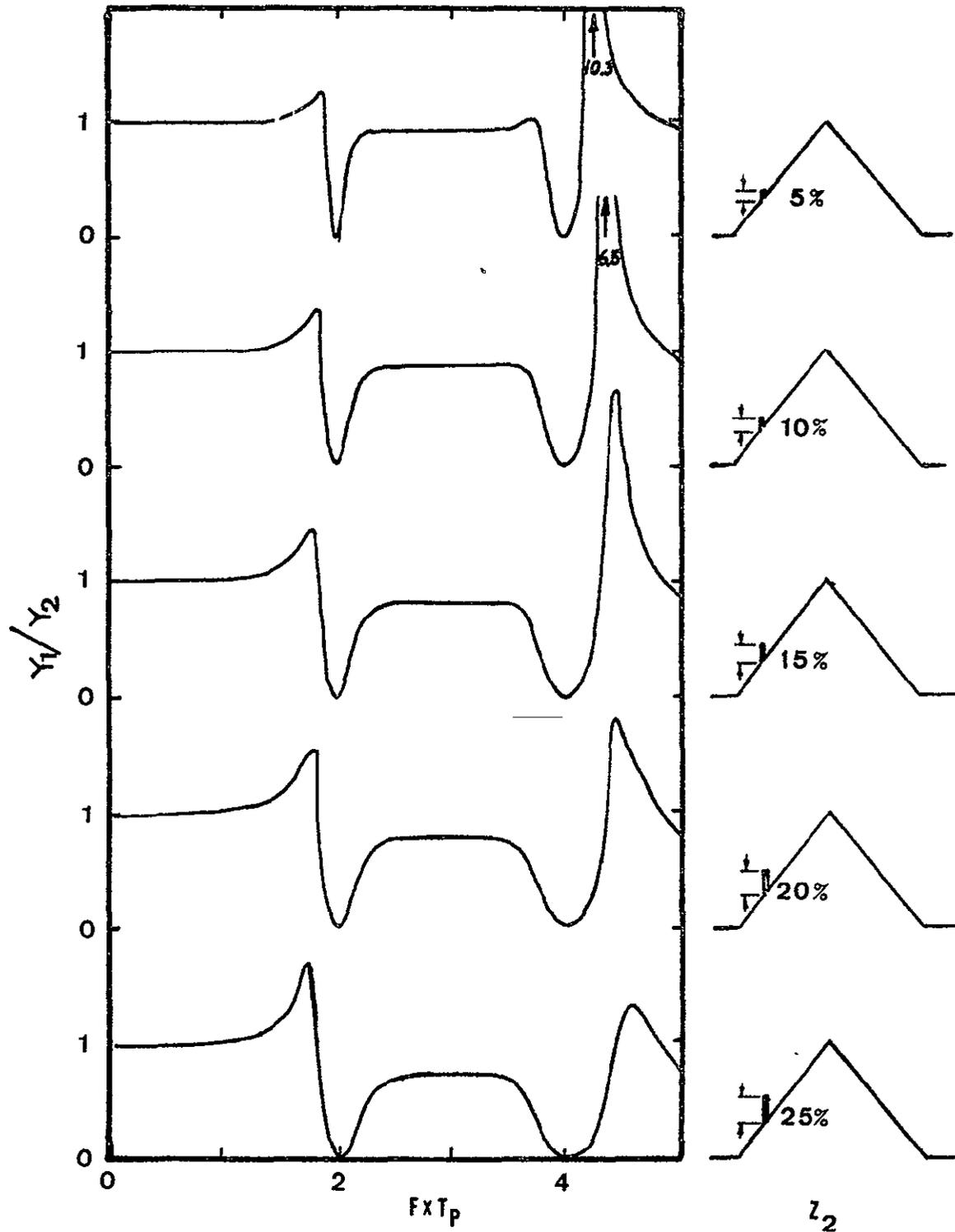
Fig. 9. Fourier transfer function plots for perturbation of different height located at 0.125 Tp from the leading edge of a triangular pulse.
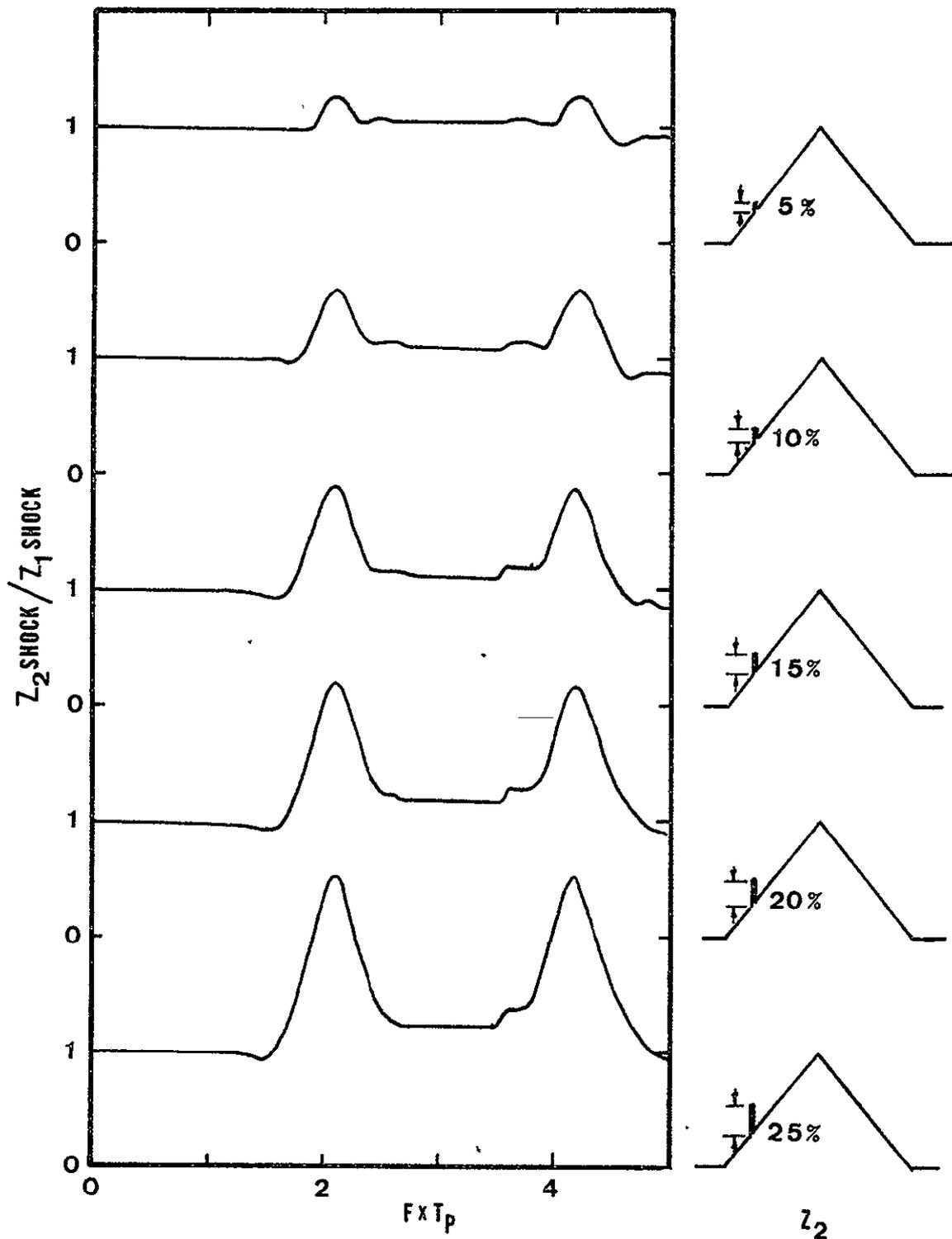
Fig. 10. Shock spectrum ratio plots for perturbation of different height located at 0.125 Tp.
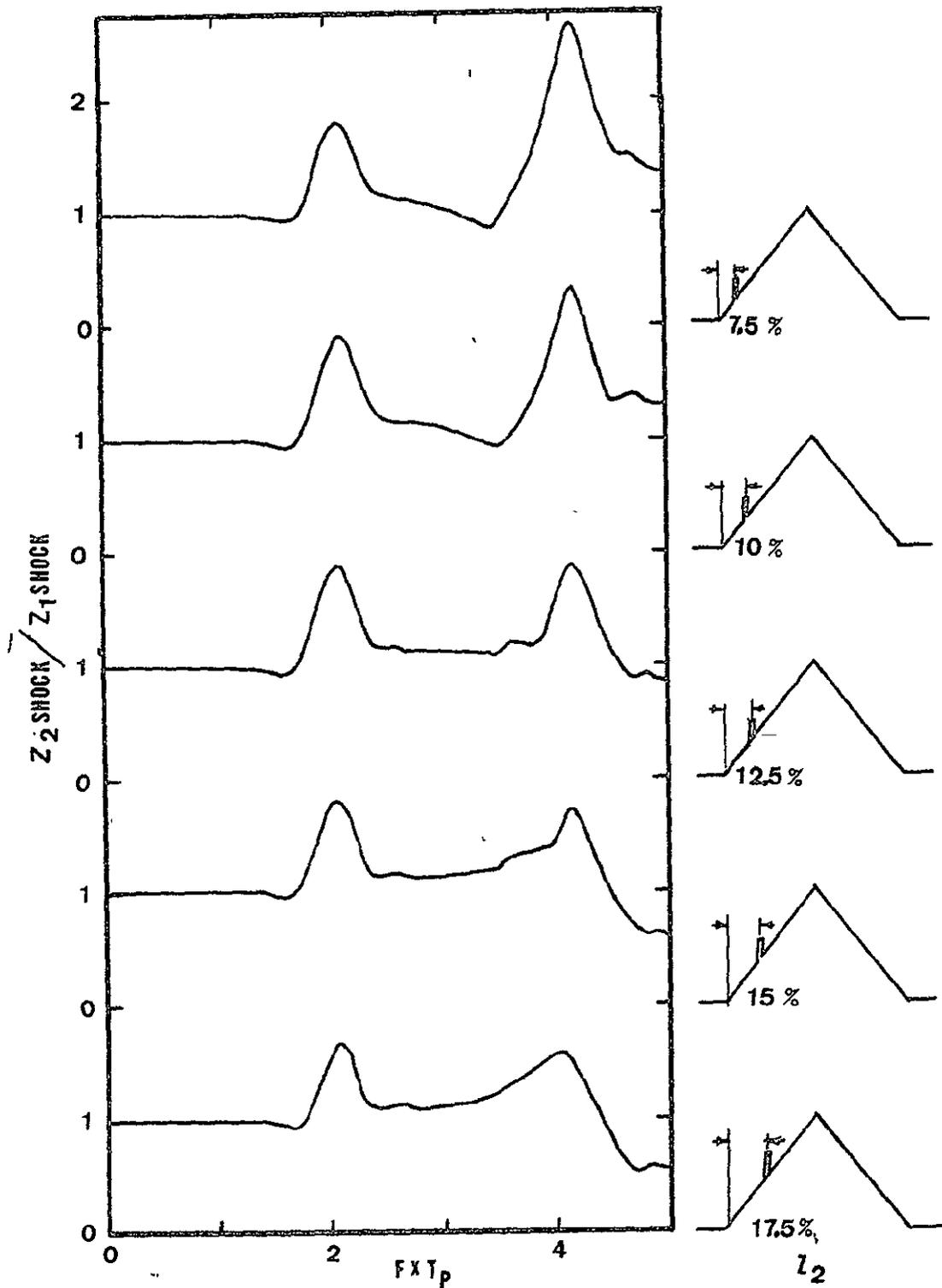
Fig. 11. Shock spectrum ratio plots for perturbation 0.15* peak height at different locations along the pulse.

1. Natural frequency: between 100 and 500 kHz, primarily because of the good transmission through the material of pulse information in this frequency range.

2. Transducer damping: low for extended periods of ringing ($\zeta = 0.01$).

3. Filtering: high-pass for frequencies above approximately 50 kHz to mask out unwanted background noise.

An analysis of the modifying influence caused by the measurement system was made by modeling the transducer as a simple single-degree-of-freedom accelerometer and a filter as a single-pole passive filter. This simple model is not fully representative of an AE transducer, since laboratory measurements indicate that AE transducers have many modes of resonance as would be expected from a distributed parameter system.

Mathematical Definition of the System

The system is shown schematically in Figure 3. To avoid obscuring the overall issue and following conventional usage (21), the transducer will be modeled by a simple single-degree-of-freedom lumped parameter piezoelectric accelerometer. For this study the filters are simple single-pole and -zero passive networks. Higher order representations of filters and transducers will be used in later studies.

Model development

Figure 3 shows schematically the mass of the transducer plus the mass effect of the piezoelectric material (M), supported by an effective spring stiffness (K) of the piezoelectric material, and internal plus external damping within the transducer, modeled by an equivalent viscous damper (C). The transducer is designed to respond to an input acceleration (force) at the base, $\ddot{z}_1(t)$[†]. The force transmitted through the 'spring' corresponds to a shear or compressive stress in the piezoelectric material. A voltage z_2 is generated proportional to the strain between the mass and the foundation (or base), i.e.,

$$z_2 = K_{pu}(x - z_1), \text{ volts} \qquad (7)$$

where K_{pu} is a constant.

The signals of interest are z_2, the transducer output; z_4, the system output; and z_5 the reconstructed (deconvoluted) input. Generation of $z_5(t)$ is considered later. In operation form z_2 and z_4 are given respectively by

$$\frac{z_2(t)}{\ddot{z}_1(t)} = \frac{-K_{pu}}{D^2 + 2\zeta\omega_n D + \omega_n^2} \qquad (8)$$

and

[†]In general the argument (t) expressing the time dependence of the signals will be suppressed for convenience; retention will be for clarity or for emphasis, as in $z_5(t)$ below.

$$\frac{Z_4(t)}{\ddot{Z}_1(t)} = \frac{-K_{pu}\omega_{lp}D}{(D^2 + 2\zeta\omega_1 D + \omega_n^2)(D + \omega_{hp})(D + \omega_{lp})} \tag{9}$$

where:

D = operator for d/dt

ζ = C/2 $\sqrt{KM}$

ω_n = $\sqrt{K/M}$, transducer natural frequency $(2\pi f_n)$

ω_{hp} = corner frequency of first-order high-pass filter $(2\pi f_n)$

ω_{lp} = corner frequency of first-order low-pass filter $(2\pi f_{lp})$

K_{pu} is redefined to include M, $K_{pu} \rightarrow K_{pu}/M$.

The solution of equation (9) is relatively straight-forward when the input signal $Z_1(t)$ is simply described mathematically. When the pulses are irregular in shape and occurrence, solutions may be impossible (or at least impractical) to obtain analytically. Accordingly, it is useful to also employ numerical integration in such cases, and eventually in general. After some algebraic manipulation of equation (9), the system differential equation is:

$$\frac{d^4 Z_4}{dt^4} = -(2\zeta\omega_n + \omega_{hp} + \omega_{lp})\frac{d^3 Z_4}{dt^3} - \omega_n^2 + 2\zeta\omega_n(\omega_{hp} + \omega_{lp}) + \omega_{hp}\omega_{lp}\frac{d^2 Z_4}{dt^2}$$

$$-\omega_n^2(\omega_{hp} + \omega_{lp}) + 2\zeta\omega_n\omega_{hp}\omega_{lp})\frac{dZ_4}{dt}$$

$$-\omega_{hp}\omega_{lp}\omega_n^2 Z_4 - K_{pu}\omega_{lp}\frac{d\ddot{Z}_1}{dt} \tag{10}$$

One advantage of this form is that 'initial conditions' (residual values from previous pulses) can be handled without difficulty, thereby facilitating treatment of arbitrarily shaped and spaced signals.

Preliminary system design studies using equation (10) to generate Z_4 for given inputs $\ddot{Z}_1$ showed the low-pass filter to be redundant, since the transducer already acts as a low-pass filter. Therefore a modified transfer function excluding the low-pass filter was used in the studies presented here. The modified system operator form and differential equation are, respectively

$$\frac{Z_4}{\ddot{Z}_1} = \frac{-K_{pu}D}{(D^2 + 2\zeta\omega_n D + \omega_n{}^2)(D + \omega_{hp})} \tag{11}$$

and

$$\frac{d^3Z_4}{dt^3} = -(2\zeta\omega_n + \omega_{hp})\frac{d^2Z_4}{dt^2} - (\omega_n{}^2 + 2\zeta\omega_n\omega_{hp})\frac{dZ_4}{dt}$$

$$-\omega_n{}^2\omega_{hp}Z_4 - K_{pu}\frac{d\ddot{Z}_1}{dt} \tag{12}$$

Equations (11) and (12) (or (9) and (10)) are used to determine the fidelity of the data signal Z_4 to the test inputs $\ddot{Z}_1$ by comparing the frequency spectra. To solve equations (10) or (12), a fourth-order predictor-corrector Runge-Kutta integration scheme is used (20).

Several pulse shape configurations were used to demonstrate the influence of the measurement system on the pulse shape. Three pulses of different shapes with equal pulse widths were selected for testing. The square, cosine and triangular pulse are shown in Figure 12. The damping ratio for the transducer was 0.01 and the high-pass filter corner $F_{hp}/F_n \doteq 0.1$ are reasonably representative of present pulse counting designs.

The pulse shapes that come out of the transducer-filter system are shown in Figure 13 in the same relative positions as their input pulses. The Fourier spectrum of each output signal Z_4 were computed and are shown in Figure 14. The Fourier spectrums for the input signals would be similar to those shown in Figures 4(a) and 5(a) for the square and triangle. The distinguishing characteristics of the Fourier spectrum for these simple pulse shapes are modified significantly by passage of the pulse through the measurement system. The output signal pulse shapes for a triangle and a cosine can have nearly the same Fourier spectrum. Hence, it can be concluded that the transducer and filtrating systems presently used for AE pulse signature analysis are a major deterrent in the search for a unique signature from AE signals coming from defects.
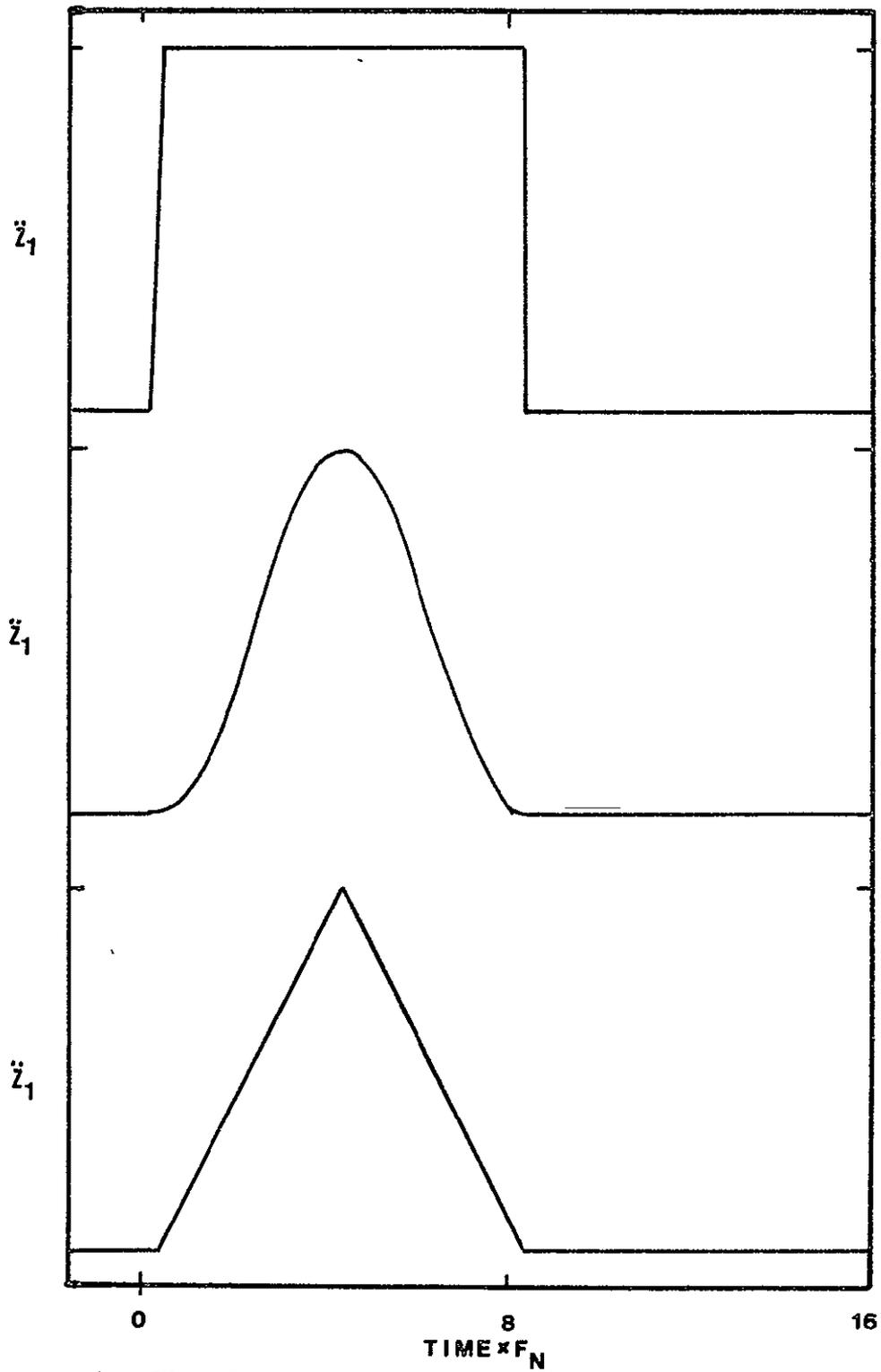
Fig. 12. Three sample acceleration pulses input at the transducer base, $\ddot{Z}_1$ vs Time x F_n.

Z_4

Z_4

Z_4

0   8   16
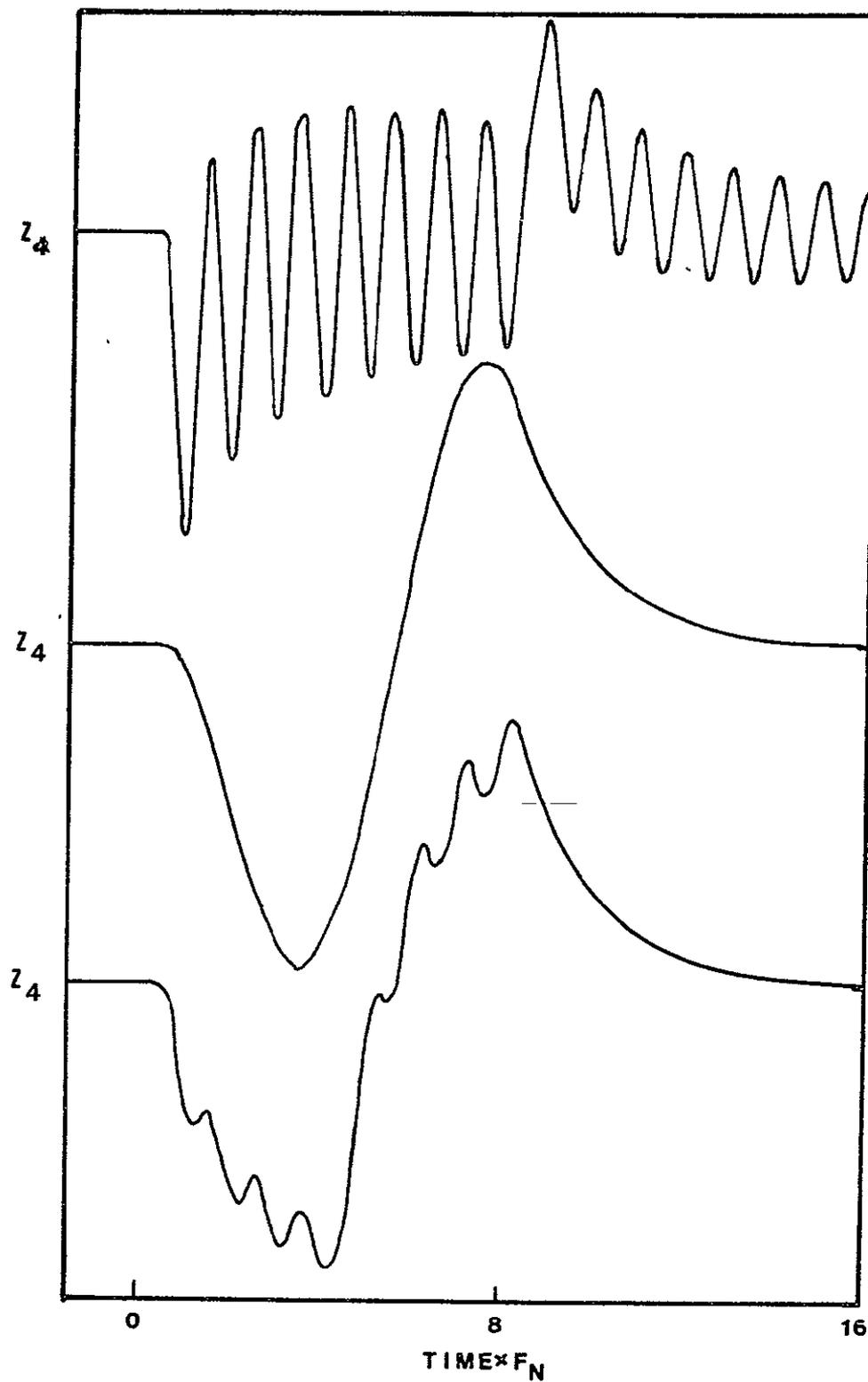
TIME×F_N

Fig. 13. Recorded output of three sample pulses, sequence as in Fig. 12, Z_4 vs Time x F_n.
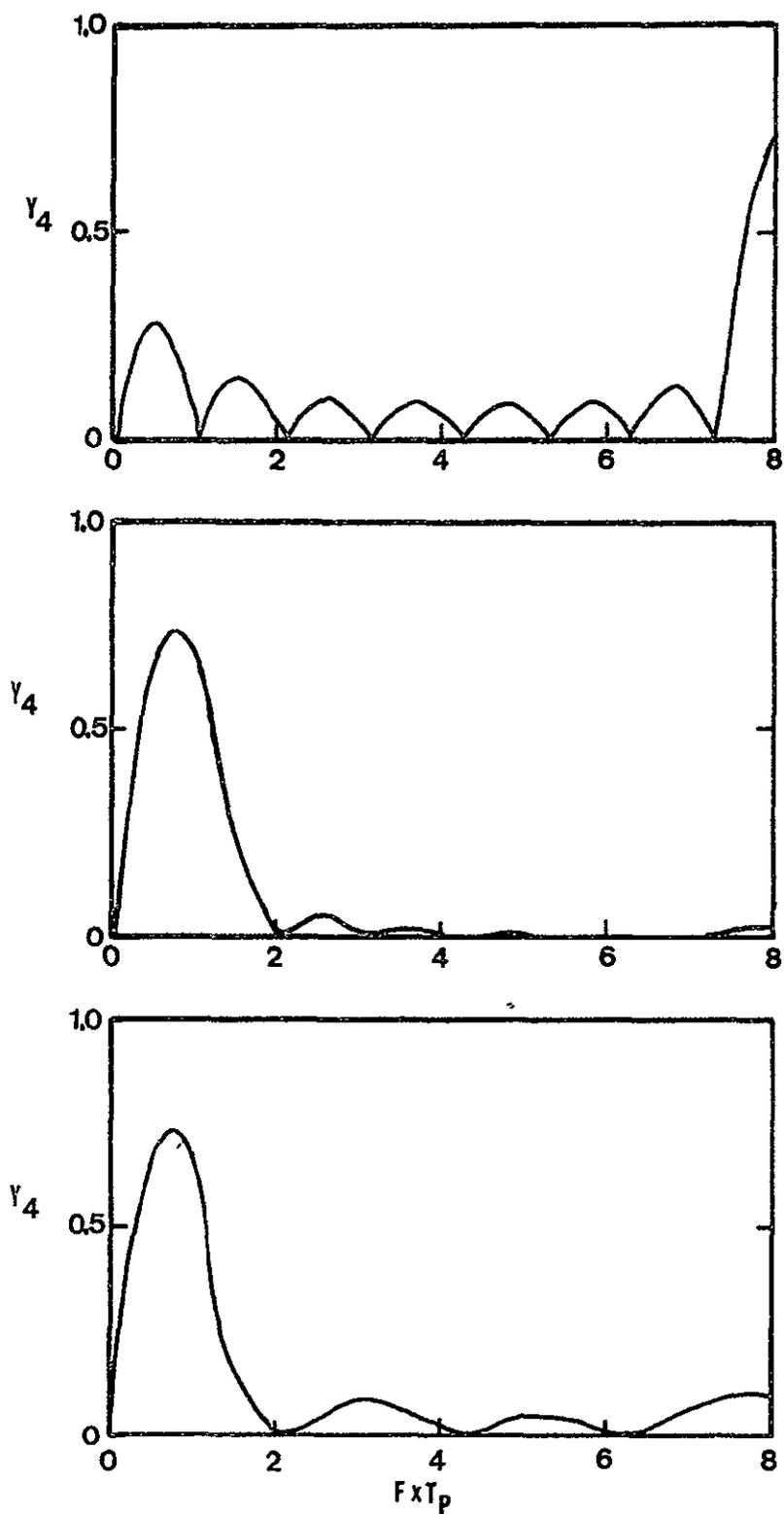
Fig. 14. Fourier spectrum of three sample output pulses, sequence as in Fig. 13.

Deconvolution method

An alternative to pulse counting and frequency spectra analysis is time domain reconstruction of the pulse or pulse train. It would be a step forward if the transducer and its modifying effects on the signal could be eliminated by computing the shape of the signal before it entered the transducer. That is, utilizing recently-developed laboratory-compatible digital storage units; if one had the correct computer routine, the digitized transducer output could be manipulated (deconvoluted)[††] to determine the approximate original shape of the pulse at the base of the transducer. Although intriguing, this approach does not appear to have been reported. To implement the deconvolution idea, a computer routine is required to manipulate the data signal Z_4 in terms of the assumed or known dominant instrumentation system parameters. The result, Z_5 in Figure 3, is then a reshaped time-domain ¦pulse' based on the recorded output shape. To implement this approach equation (12) is expressed in suitable finite difference form:

$$Z_5(i) = Z_5(i-1) - \frac{\Delta t}{K_{pu}} \{ \omega_n^2 \omega_{hp} Z_4(i) + (\omega_n^2 + 2\zeta\omega_n\omega_{hp})(Z_4(i+1)$$

$$-Z_4(i-1))/2\Delta t + (2\zeta\omega_n + \omega_{hp})(Z_4(i+1) - 2Z_4(i) + Z_4(i-1))\Delta t^2$$

[††] Deconvolution is defined as identifying an input in the time domain, given the output and the system transfer function.

$$+(Z_4(i+2)-2Z_4(i+1)+2Z_4(i-1)-Z_4(i-2)/2\Delta t^3) \qquad (13)$$

where i, $i+1$, ..., $i-1$, etc. represent values at present, future and past discrete times. Δt is the sampling period. Thus $Z_5(i)$ is the estimate of the corresponding $\ddot{Z}_1(t)$, based on $Z_4(i)$, which is the signal actually recorded and the only true knowledge available when real signals are treated.

A typical output from the deconvolution program is shown in Figure 15. This figure illustrates the deconvoluted signals that were generated from the original filtered signals shown in Figure 13. They can be compared favorably to the original signals that went into the transducer filter system, Figure 12. Thus, it appears that the deconvolution process can produce recognizable signals that are identical to those that input to the transducer-filter-recorder, and can effectively eliminate the signature identification difficulties caused by the measurement system.

Summary of Evaluation of Signature Analysis Methods

Four frequency domain signature analysis methods have been examined and evaluated for their ability to distinguish features associated with acoustic emission pulses. The Fourier transform method and the shock spectrum method are shown to be relatively insensitive as to their ability to distinguish between square, triangular and cosine pulses, and even less sensitive when asked to distinguish between simple pulses and the same pulse with a small perturbation.
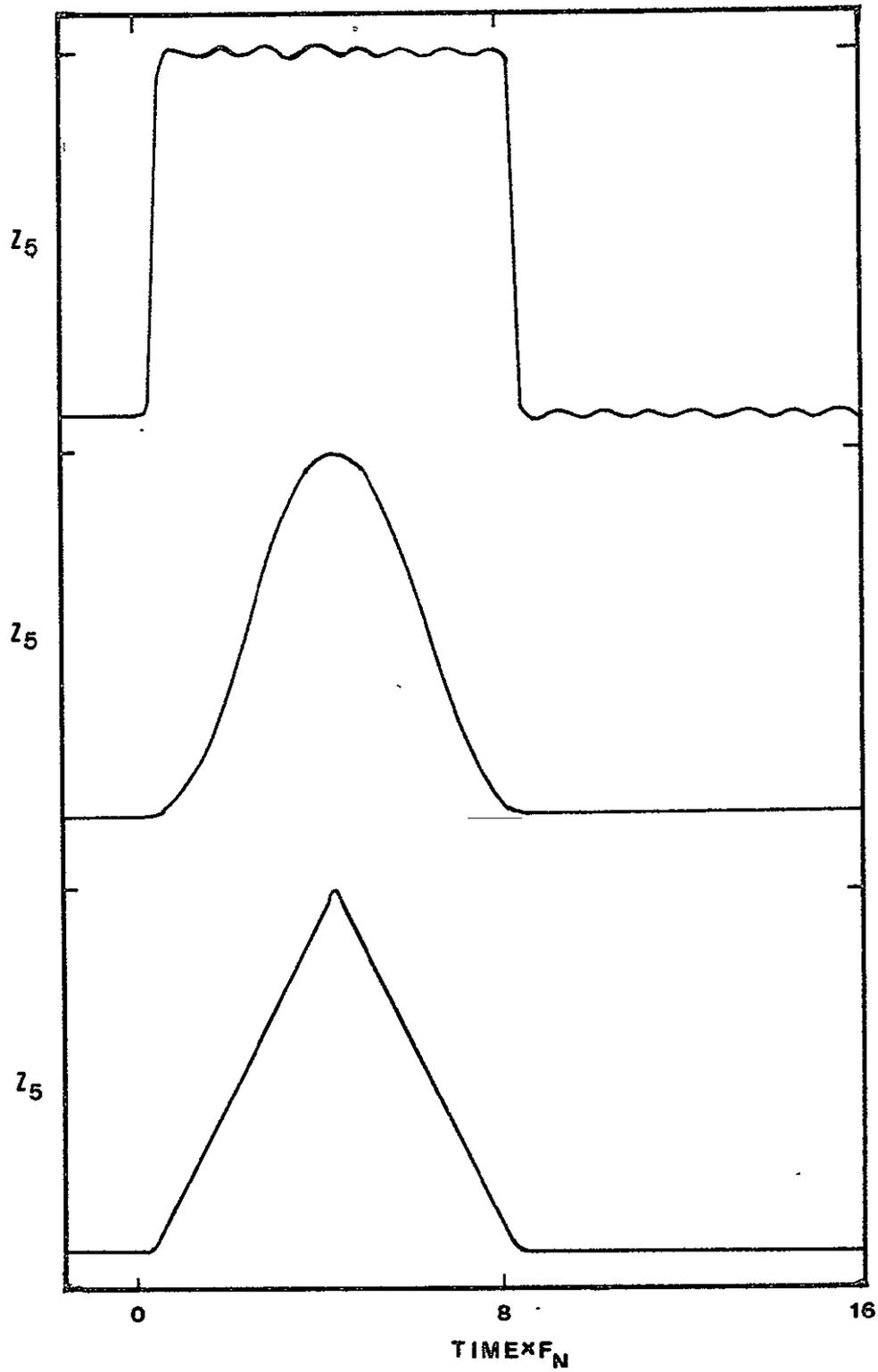
Fig. 15. Deconvolution of three sample pulses, Z_5 sequence as in Figure 12.

Fourier transfer function and the shock spectrum ratio tech-
niques have also been evaluated, in which the output trans-
form is divided by the input transform at each value of fre-
quency. It is shown that the Fourier transfer function does
amplify the difference between the simple input signal and
small perturbations on the simple signal, but does so only at
the particular frequencies associated with the near-zero
values of amplitude in the Fourier spectrum. The shock
spectrum ratio does distinguish between different types of
pulses, between perturbed pulses and between different types
of perturbations of the original pulse. A significant fea-
ture of the shock spectrum is that it does not go to zero at
any frequency. Thus the shock spectrum ratio does not shift
dramatically as seen with the Fourier transfer function. Of
all the signature analysis techniques examined, the shock
spectrum transfer function is the most adequate for analyz-
ing the experimental pulses.

The transducer-filter system was shown to have a sig-
nificant influence on the Fourier spectrum, such that the
input pulse shape could not be discernable nor could the
primary output Fourier transform be used to characterize
acoustic emission bursts, even from simple inputs. A decon-
volution system was demonstrated as a means to generate a
new signal that closely represents the input signal shape.

CHAPTER III

OPTIMAL DESIGN OF THE TRANSDUCER AND

FILTER MEASUREMENT SYSTEM

Introduction

An important consideration in pulse data recording is

the selection of filters (corner frequencies) and transducers

(natural frequencies and damping). This maximizes the infor-

mation output relevant to the input signal and minimizes the

extraneous information in the signal. When commercial AE

transducers are used for sophisticated frequency analysis

experiments, the transducers are built primarily to meet the

specifications listed in Chapter II. Accordingly, this

chapter proposes to consider the following questions.

1. Can modern optimal design techniques be used to
   determine the best AE transducer natural fre-
   quency, system damping, and filter frequencies
   (high-pass and low-pass) for the frequency
   analysis of an acoustic emission pulse?

2. What design criteria should be used? Are there
   other methods which could be employed for fre-
   quency domain or time domain examination of the
   pulses?

3. How much information is lost if a nonoptimal sys-
   tem such as the pulse counting system is used for
   the collection of pulse data?

Four methods for spectrum analysis of input and output

pulses described in Chapter II can be considered for signa-

ture analysis. The first is the Fast Fourier Transform

45

approach, which is primarily used in this chapter. The second is a Fourier transfer function of the output pulse relative to the input pulse. The third is to calculate the shock spectrum at zero damping of input and output pulses. The ratio of the output and input shock spectra is a fourth method. Time domain reconstruction of the pulse may be even more enlightening than the spectral analyses. This method is to deconvolute the output pulse information to the approximate shape of the original input pulse at the base of the transducer by differentiation using finite difference techniques.

The method used for quantification of the differences between the spectra of the input and output pulses is the statistical standard error of estimate, which is the root-mean-square differences of a set of data and a reference set. (Explicit forms are given below in equations (14) and (15).) Thus, the objective function for the optimal design of the transducer-filter-measurement system is to minimize the difference between two pulse spectra by selection of the system design variables; these may be functions of pulse shape, magnitude, and duration. To study the question (1) above, analytical pulses (e.g., square, triangular, etc.) are used. Among other things, it is shown that pulse duration does affect the optimum.

In the following, the criterion is mathematically expressed. Results are obtained using an optimal design technique, described later.

Design Strategy and Criteria

The variables influencing the system response and which are, to some extent, under the influence of a designer have already been suggested in the model development and were related to the system variables following equation (10). They are:

f_n transducer natural frequency ($\omega_n/2\pi = 1/T_n$)

ζ transducer damping ratio

f_{hp} high pass filter corner frequency ($\omega_{hp}/2\pi = 1/T_{hp}$)

f_{lp} low pass filter corner frequency ($\omega_{lp}/2\pi = 1/T_{lp}$)

where T is the equivalent time constant.

The independent variables are input pulse width and shape. Height and rates of occurrence are not considerations, since at this time perfect resolution, etc. are assumed. One of the variables can be eliminated and the solutions made more general by normalizing the filter corner frequencies and pulse width (time) with respect to the transducer natural frequency f_n.

A suitable function for evaluating the performance of a transducer-filter system is the statistical standard error of estimate, since analytical signals of the general type expected are used for the input Z_1. This measure is also suitable as a criterion for determining the feasibility and value of optimal system design. With reference to Figure 3, the statistical standard error of estimate may be expressed in the frequency and time domains as:

$$\text{FDEV} = \left[\frac{1}{\Omega} \int_0^{\Omega} (Y_4 - Y_1)^2 \, d\omega \right]^{\frac{1}{2}} \tag{14}$$

for the frequency domain where

$Y_4 = Y_4(j\omega)$, the Fourier transform of the output $Z_4(t)$

$Y_1 = Y_1(j\omega)$, the Fourier transform of the input $\ddot{Z}_1(t)$

Typically Ω is 50/pulse width. The time domain (defining $e = Z_5(t) - Z_1(t)$) is expressed as

$$\text{TDEV} = \left[\frac{1}{T} \int_0^{\infty} e^2 dt \right]^{\frac{1}{2}} \tag{15}$$

In digital form, with

$$e_i = Z_5(i) - Z_1(i),$$

$$\text{TDEV} = \left[\frac{1}{n-1} \sum_{i=1}^{I(t)} e_i^2 \right]^{\frac{1}{2}} \tag{16}$$

T and n relate to pulse duration. $I(t)$ corresponds to the time $t \to \infty$ until any substantial contribution to the value of TDEV dissappears (typically 50T). The values of these criteria are directly comparable: the lower the value, the better the performance. A flow chart showing the frequency and time domain evaluations is shown in Figure 16 (including the entry points for the optimal design phase). The sequence for a frequency spectrum solution is:

1. input an acceleration pulse, $\ddot{Z}_1(t)$

2. solve for the system response, $Z_4(t)$

3. normalize the pulses to a maximum height of 1.0

Optimal Design
Phase

Entry Point (with
modified values of
System Parameters)

Davidon-
Fletcher
Powell
Algorithm
+
Penalty
Functions

Return Point

Additional
cases, if
more data

Frequency
Spectrum
Analysis

Time Domain
Deconvolution

Companion
Subroutine

```
┌─────────────────────────────┐
│ Initialize Variables        │
│ INPUT:-Sampling Parameters  │
│   ΔT, N                      │
│   Pulse Data $\ddot{Z}_1(t)$ │
└─────────────────────────────┘
```

```
┌─────────────────────────────┐
│ INPUT:-System Parameters    │
│   $K_{pu}$, $\zeta$, $f_{hp}/f_n$, $f_{\ell p}/f_n$ │
└─────────────────────────────┘
```

```
┌─────────────────────────────┐
│ Solve Transducer System:    │
│ Sub. PICKUP                 │
│   $\dot{Z}_1 \rightarrow Z_4$ │
│                             │
│   Att'n RATIO= $\dfrac{Z_4(t)}{Z_1(t)}$ min │
└─────────────────────────────┘
```

```
┌──────────────────────┐
│ Normalize $\ddot{Z}_1$ │
│ $Z_4$ to maxima       │
│ Calculate             │
│ Freq. Spectra:        │
│ Sub. FREQSP           │
│ $Z_1 \rightarrow$     │
│ $Y_1 \leftarrow$      │
│ $Z_4 \rightarrow$     │
│ $Y_4 \leftarrow$      │
│ Evaluate              │
│ FDEV, eq.(14)         │
└──────────────────────┘
```

```
┌──────────────────────┐
│ Deconvolution        │
│ Sub RESHAPE          │
│ $Z_4 \rightarrow$    │
│ $Z_5 \leftarrow$     │
│                      │
│ Evaluate             │
│ TDEV, ez.(15)        │
└──────────────────────┘
```

```
┌─────────────────────────────┐
│ OUTPUT Results: $\zeta$, $f_{hp}/f_n$, │
│ $f_{\ell p}/f_n$, RADIO, FDEV or TDEV │
│ Plot Graphs                 │
└─────────────────────────────┘
```

stop

```
┌─────────────────────────────┐
│ PICKUP                      │
│ Runge-Kutta Solution        │
│ of System Differential      │
│ Equation                    │
│   $\rightarrow \ddot{Z}_1$  │
│   $\leftarrow Z_4$          │
└─────────────────────────────┘
```

```
┌─────────────────────────────┐
│ FREQSP                      │
│ Fourier Transform           │
│ Solution                    │
│                             │
│ $Y(j\omega)= Z(t)\exp(-j\omega t)dt$ │
└─────────────────────────────┘
```

```
┌─────────────────────────────┐
│ RESHAPE                     │
│ Deconvolution of            │
│ output signal,              │
│ eqn (7).                    │
│   $\rightarrow Z_4$         │
│   $\leftarrow Z_5$          │
└─────────────────────────────┘
```

Fig. 16. Flow chart for frequency domain and time
domain objective function solution.

4. fast Fourier transform $\ddot{Z}_1$ and Z_4

5. evaluate FDEV, equation (14).

The sequence for the time domain solution (second stage) is:

1. input an acceleration pulse, $\ddot{Z}_1(t)$

2. solve for the system response, $Z_4(t)$

3. solve for the deconvoluted pulse, $Z_5(t)$

4. evaluate TDEV, equation (15).

Results

The initial thrust of this study was to investigate frequency spectrum characteristics as a criterion for evaluating acoustic emission data as suggested by the cited investigators. As will be shown, frequency spectrum comparisons and straightforward integration of the data signal Z_4 were in many instances inconclusive, even when treated in an optimal design mode. At this point the deconvolution idea emerged and was implemented.

To compare the various approaches, initially a comprehensive study was made of a 'typical' system design with representative input pulse shapes and pulse durations. These were then followed by an optimal design study based upon the frequency domain criterion, FDEV. These results are presented to clearly identify the attributes of frequency domain criteria (characterized here by the Fourier spectrum) vis-a-vis time domain (deconvolution) criteria and the effects of signal shape and duration. In so doing, frequency spectrum and deconvolution results appear simultaneously, although it

is to be emphasized that the deconvolution approach was initiated after viewing the frequency domain results. These results provided a basis for an optimal system design approach and results evaluation, which are described in the appropriate section.

General system study results

Results from the frequency domain and time domain programs are shown in Figures 17 through 22. The design variables for these figures, $\zeta=0.01$; $f_{hp}/f_n=0.1$, are reasonably representative of present pulse-counting designs. As it turns out, these tests show a 'bad' design point for frequency spectrum analysis, due to a significant underdamped vibration of the transducer. Figures 17-19 are for short pulses, and Figures 20-22 are for long pulses, relative to the transducer time constant $1/f_n$. The pulse shapes here and throughout are rectangular, triangular and cosine $(1-\cos\omega t)$, respectively. The figures N(a) show the input acceleration pulse $\ddot{Z}_1$ with the transducer-filter system response Z_4 and the deconvoluted signal Z_5 superimposed. The figures N(b) show the frequency spectrum Y_1 of the input signal $\ddot{Z}_1$ and the frequency spectrum Y_4 of the output signal Z_4. The values of the objective functions in both domains are shown in the figures.

For short pulses $(Txf_n=0.3)$, Figures 17-19, there is very little difference in the systems' outputs $Z_4(t)$ and
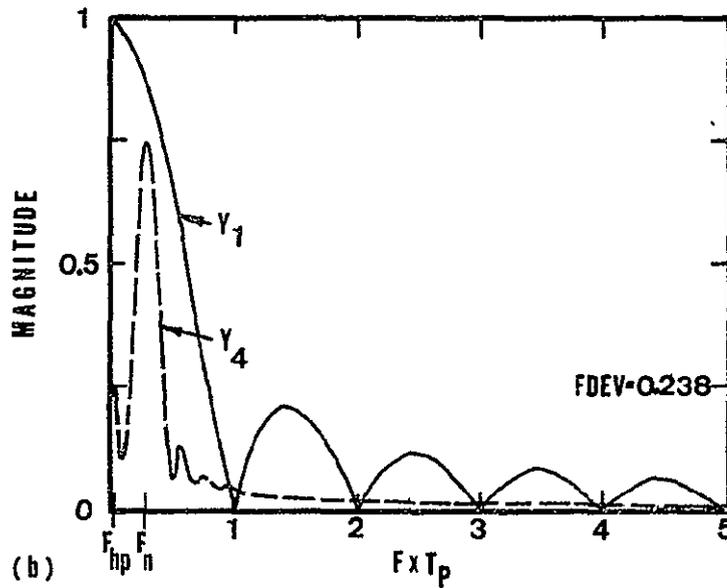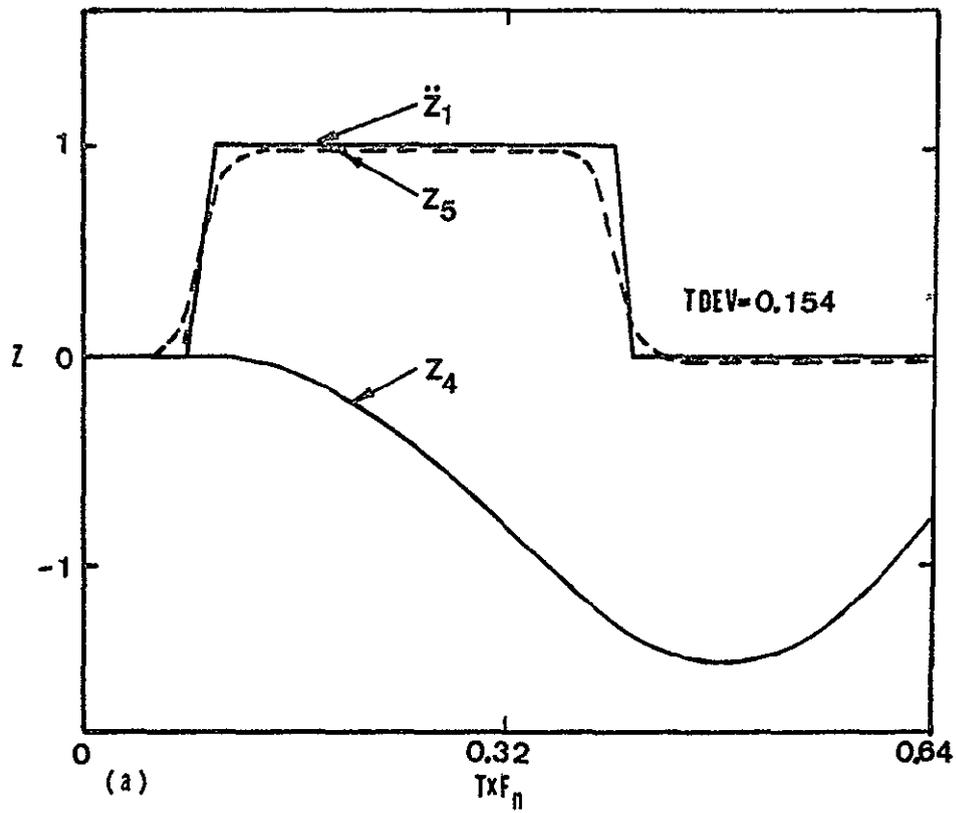
Fig. 17. Square pulse: $\zeta = 0.01$; $F_{hp}/F_n = 0.1$; $T_pF_n = 0.3$. a) time domain; b) frequency spectrum.
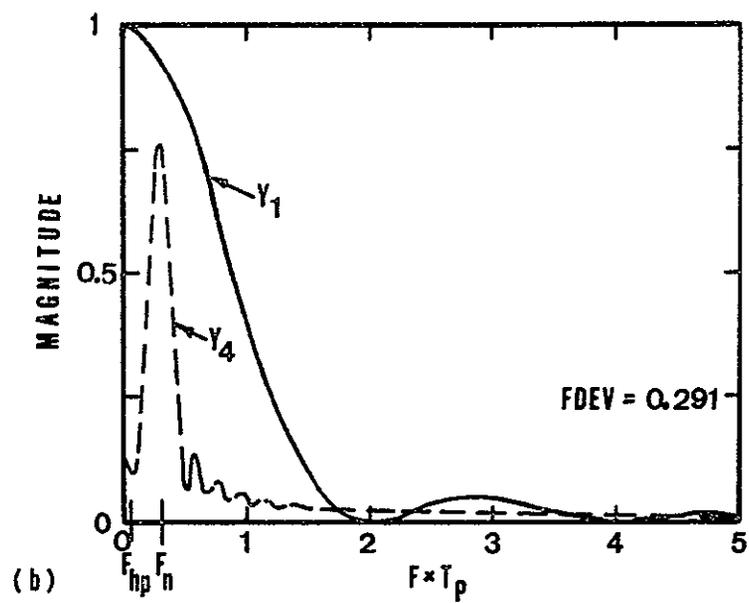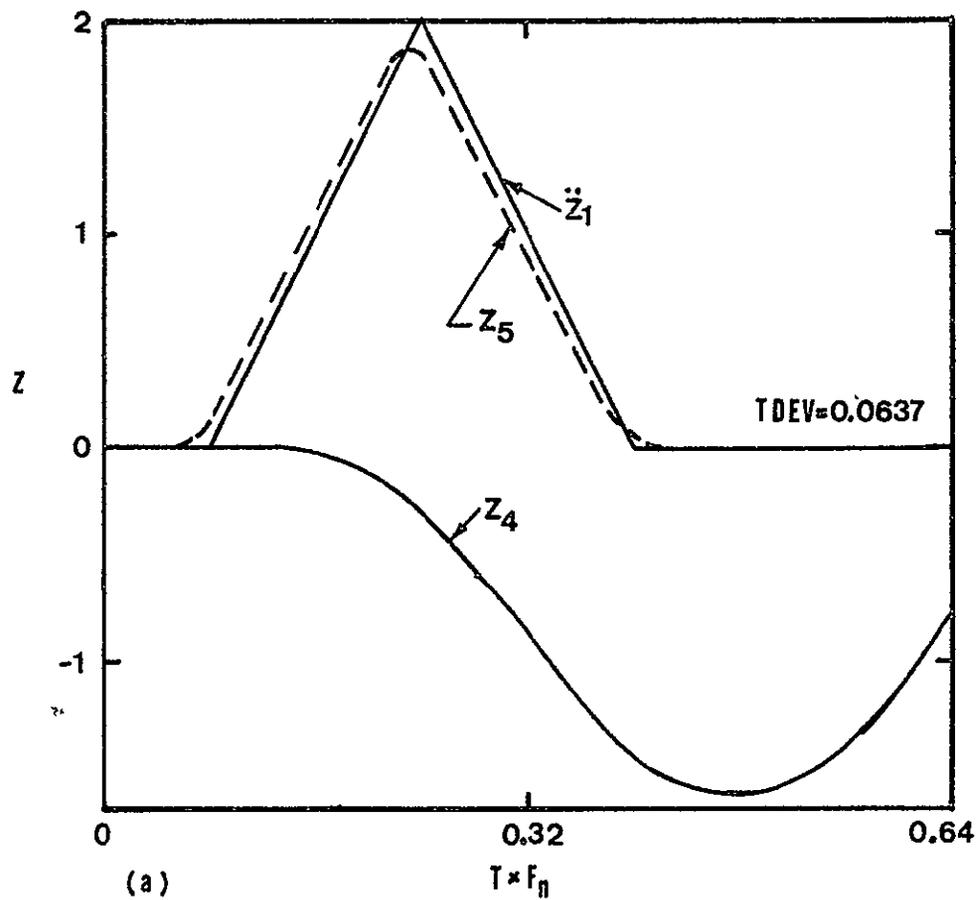
Fig. 18. Triangular pulse: $\zeta = 0.01$; $F_{hp}/F_n = 0.1$; $T_p F_n = 0.3$. a) time domain; b) frequency spectrum.
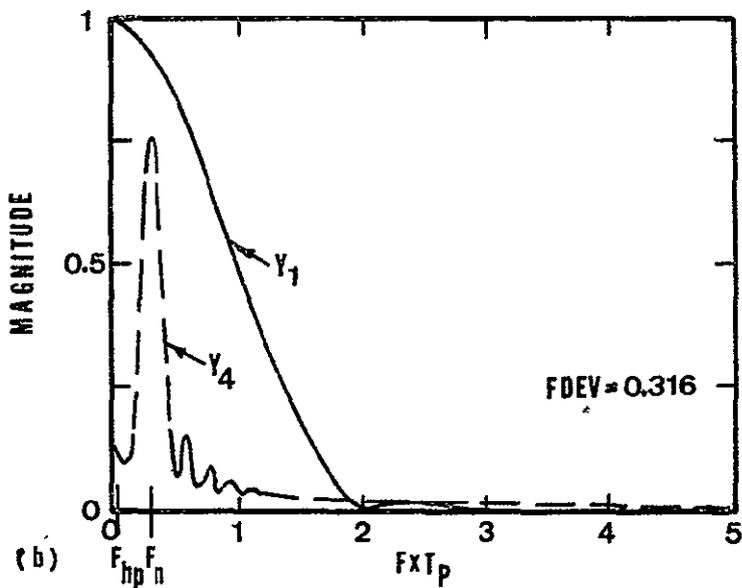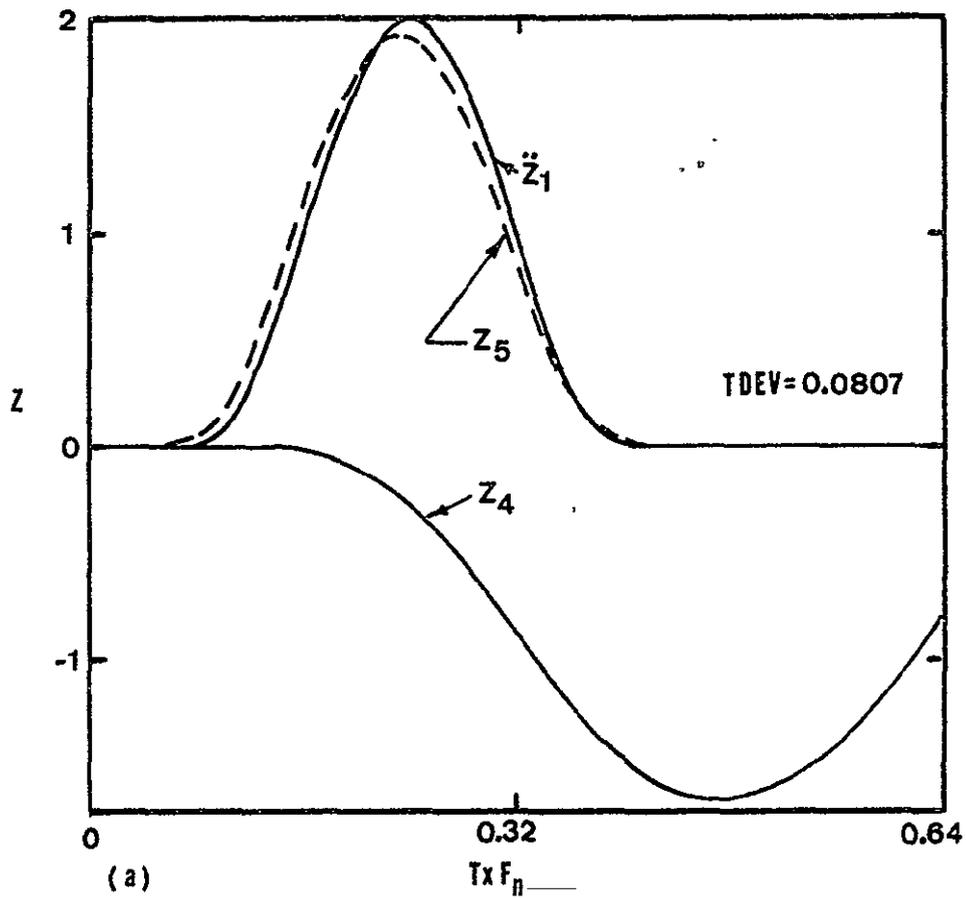
Fig. 19. Cosine pulse: $\zeta = 0.01$; $F_{hp}/F_n = 0.1$; $T_pF_n = 0.3$. a) time domain; b) frequency domain.
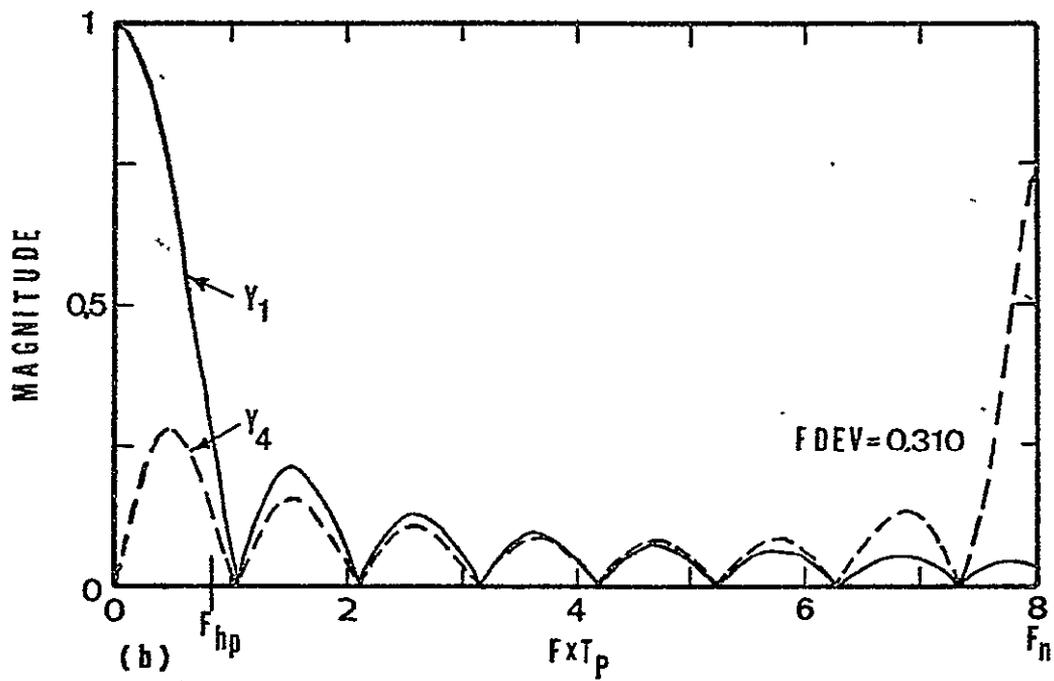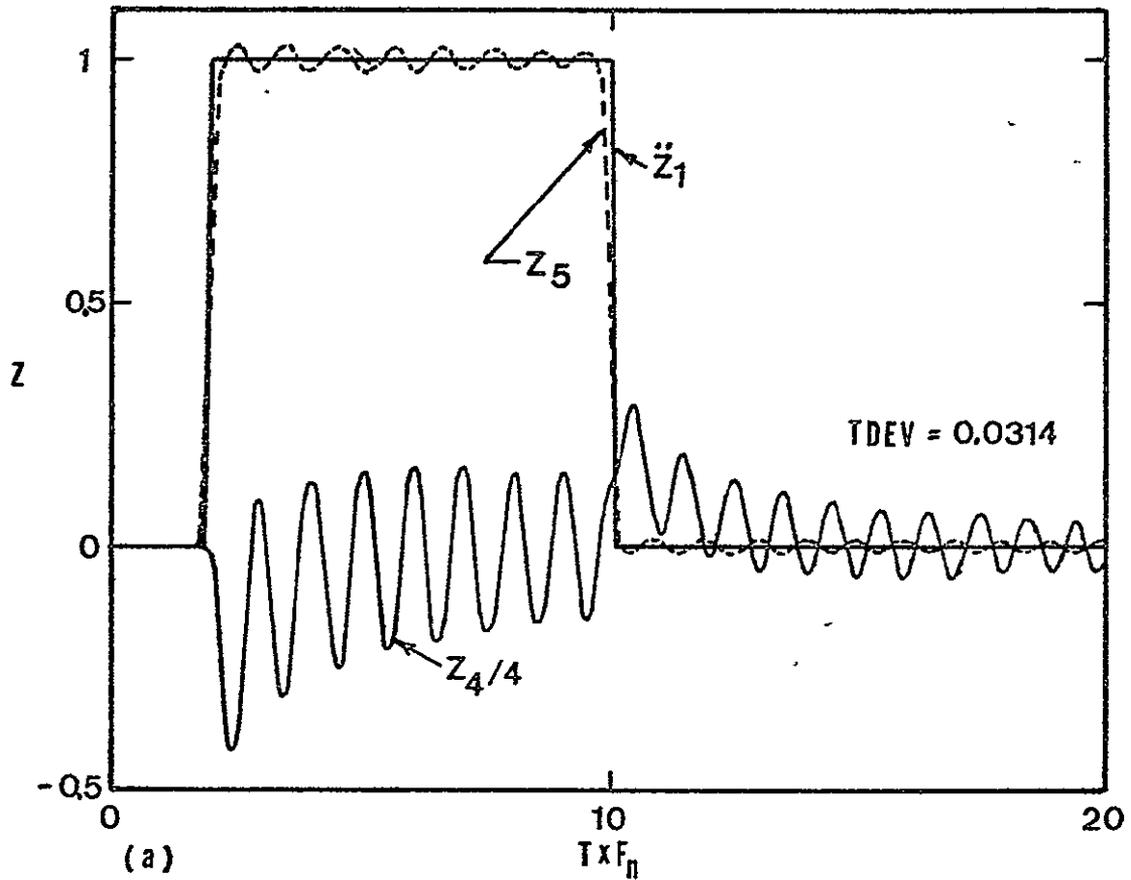
Fig. 20. Square pulse: $\zeta = 0.01$; $F_{hp}/F_n = 0.1$; $T_p F_n = 8.0$. a) time domain; b) frequency spectrum.
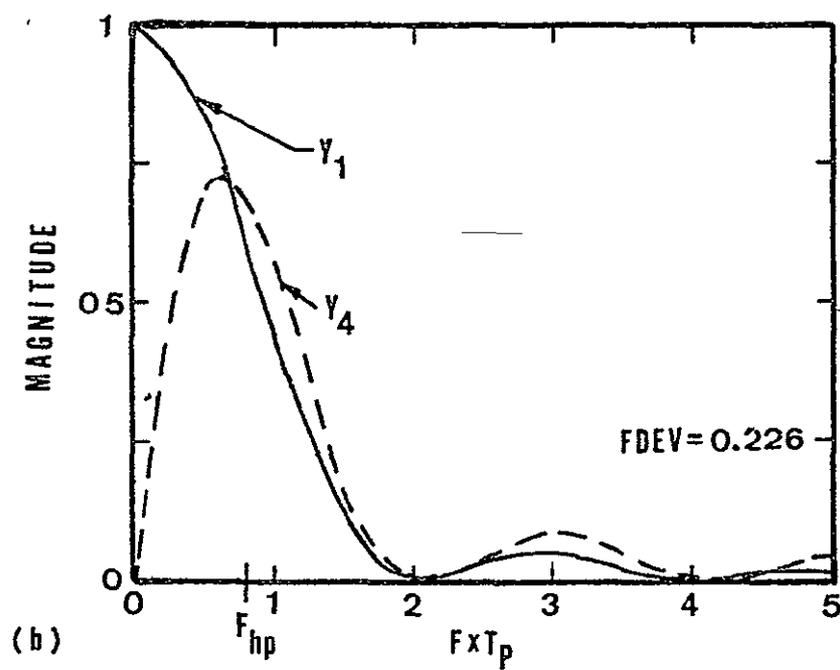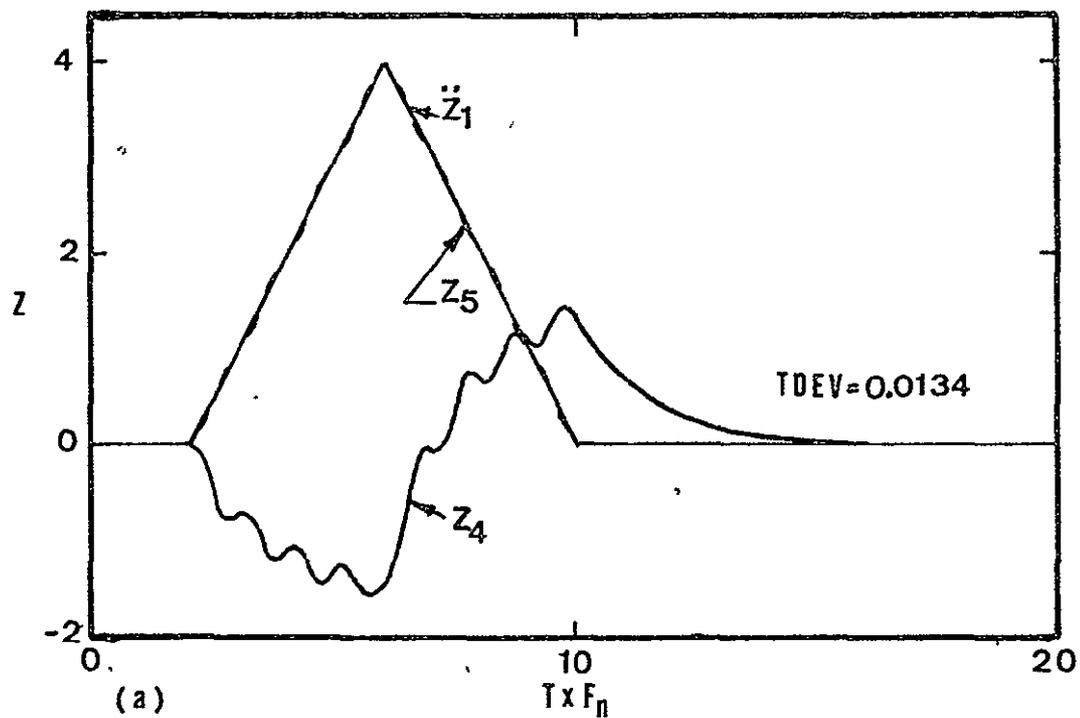
Fig. 21. Triangular pulse: $\zeta = 0.01$; $F_{hp}/F_n = 0.1$; $T_p F_n = 8.0$. a) time domain; b) frequency domain.
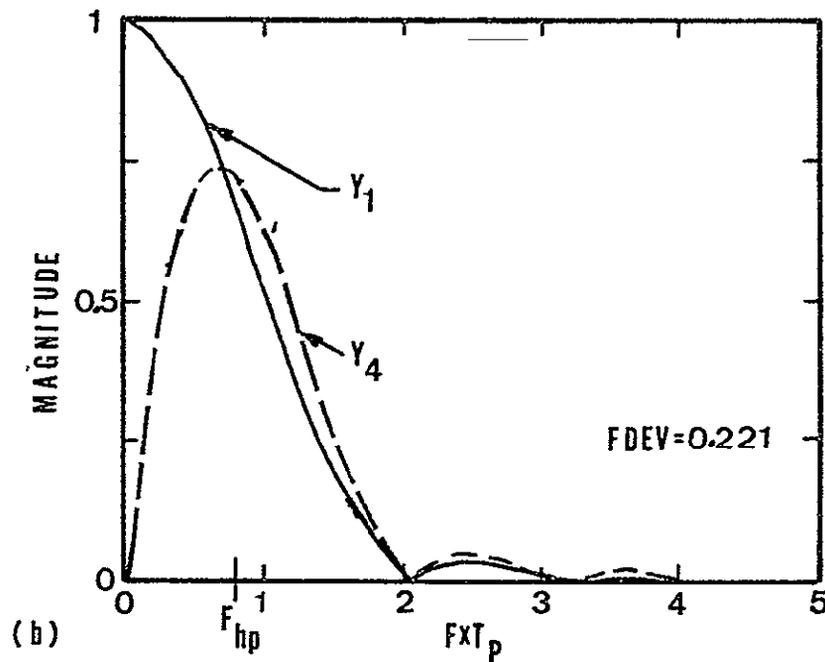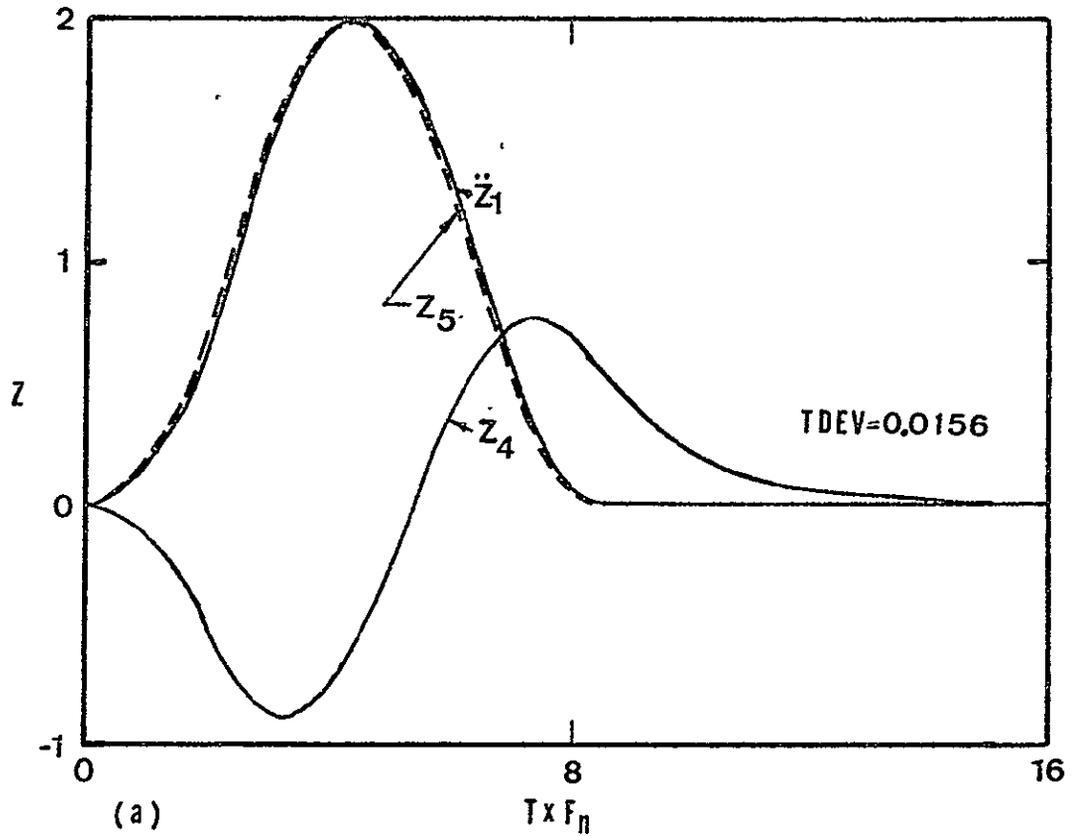
Fig. 22. Cosine pulse: $\zeta = 0.01$; $F_{hp}/F_n = 0.1$; $T_pF_n = 8.0$. a) time domain; b) frequency domain.

frequency spectra Y_4 for the three different inputs. The deconvoluted signal (Z_5 in the (a) figures) fairly well reproduces each input, although for unknown signals, this reconstruction may still be inadequate. This is investigated in the optimal design section.

Figures 20-22 show similar results for long (Txf$_n$=8) rectangular, triangular and cosine pulses respectively. The system outputs Z_4 and Y_4 are noticeably distorted, but they do not show any resemblance to each other as with the short pulses. Here the deconvolution gives very good reproduction of the triangular and cosine pulses. The effect of ringing of the transducer is clearly seen in Figures 20 and 21. The deconvoluted signal is much less sensitive to this than the transmitted signal and Fourier spectrum.

In all cases the values of the deconvolution criteria TDEV are substantially less than the frequency spectrum criterion FDEV. As these measures are directly comparable, it is clear that deconvolution approach can provide a more significant representation of the excitation. Incidentally, in all these studies, the rectangular pulses were the hardest to treat mathematically, due to the greater high frequency content.

Optimal design of transducer-filter system. Because of the predisposition to investigate the frequency domain characteristics and the rather disappointing results as

indicated by Figures 17-22, the determination of optimal system design parameters to minimize the frequency domain criterion FDEV of equation (14) was undertaken.

Accordingly, FDEV is now a design objective function to be minimized by selection of some combination of the system design variables, for a given input signal $\ddot{Z}_1$ characterized by shape and duration (ratioed to f_n). The necessary relationship (model) is determined by the appropriate dynamical equation, one of equation (10) through (13). From before, the design variables are:

f_n transducer natural frequency (dominant)

ζ transducer damping ratio (dominant)

f_{hp} high-pass filter corner frequency

f_{lp}' low-pass filter corner frequency.

The optimization procedure used here is the Davidon-Fletcher-Powell (DFP) variable-metric algorithm for minimization of an unconstrained function (22). Thus, any constraints must be treated in an indirect manner, e.g., by penalty functions. The DFP method was selected because of a good reputation for rapid convergence to a minimum value of the objective function in a large number of cases. Since the objective function calculation for the transducer-filter system is rather lengthy, rapid convergence to a good answer is important from an economic point of view.

From practical considerations, there may be constraints upon the design variables, e.g., non-negativity, reasonable

limits, etc. A practical concern in transducer-filter sys-
tems is the attenuation of the signal. Accordingly, a mini-
mum tolerable output/input signal ratio in the range con-
cerned is specified. After observing several design solu-
tions during the program development stage, it was arbitrar-
ily decided that any solution with a signal ratio below 10%
would be unacceptable.

The design limits and associated penalty functions, g_n,
were expressed as follows:

$$\left.\begin{array}{l} g_1 = \begin{cases} 0.0 \text{ for } 0.0 < \zeta < 2.0 \\ \zeta^4, \text{ otherwise} \end{cases} \\[3ex] g_2 = \begin{cases} 0.0 \text{ for } 0.05 < f_{hp}/f_n < 2.0 \\ (f_{hp}/f_n)^4 \text{ otherwise} \end{cases} \\[3ex] g_3 = \begin{cases} 0.0 \text{ for } 0.5 < f_{lp}/f_n \\ (f_{lp}/f_n)^4 \text{ otherwise} \end{cases} \end{array}\right\} \quad (17)$$

In the studies, the input pulse shape and time duration
were fixed for each optimization run. A range of pulse
shapes and durations were run. The flow chart of Figure 16
shows the general approach.

Results for frequency domain criterion. Minimizations
of FDEV of equation (14) with the appended penalty functions
of equations (17) using the DFP algorithm with short and long
square pulses $-T = .3/f_n$ and $8.0/f_n$ respectively, were under-
taken. However, the objective function field was essentially

flat with no clear minima. Furthermore, FDEV was large indicating a poor fit. This can be inferred from the (b) plots in Figures 17-22, and is seen even more clearly in Figure 23, which shows the objective function variation for three lines drawn through the field of FDEV for a short duration square pulse, $Txf_n = 0.3$. The field is quite flat with a slight gradient towards higher values of the design variables. To a slight extent this is a function of the test pulse shape. The results for longer pulses and different shapes showed similar patterns. Figure 23 also shows the ineffectiveness of the low-pass filter which was still in the system.

Consequently, these approaches were not considered to give better solutions to the problem. Trials with the other frequency domain analysis approaches mentioned previously did not appear to be substantially more definitive than the Fourier spectrum analysis and were not pursued. Some general study results akin to Figures 17-22 for other frequency domain measures were presented in Chapter II with the same overall conclusion.

It may be premature to dismiss all such procedures for AE pulse analysis, but there seemed no reason to pursue them here as design criteria. As is well known, selection of meaningful design criteria is vital to achieving valid optimal design and performance.
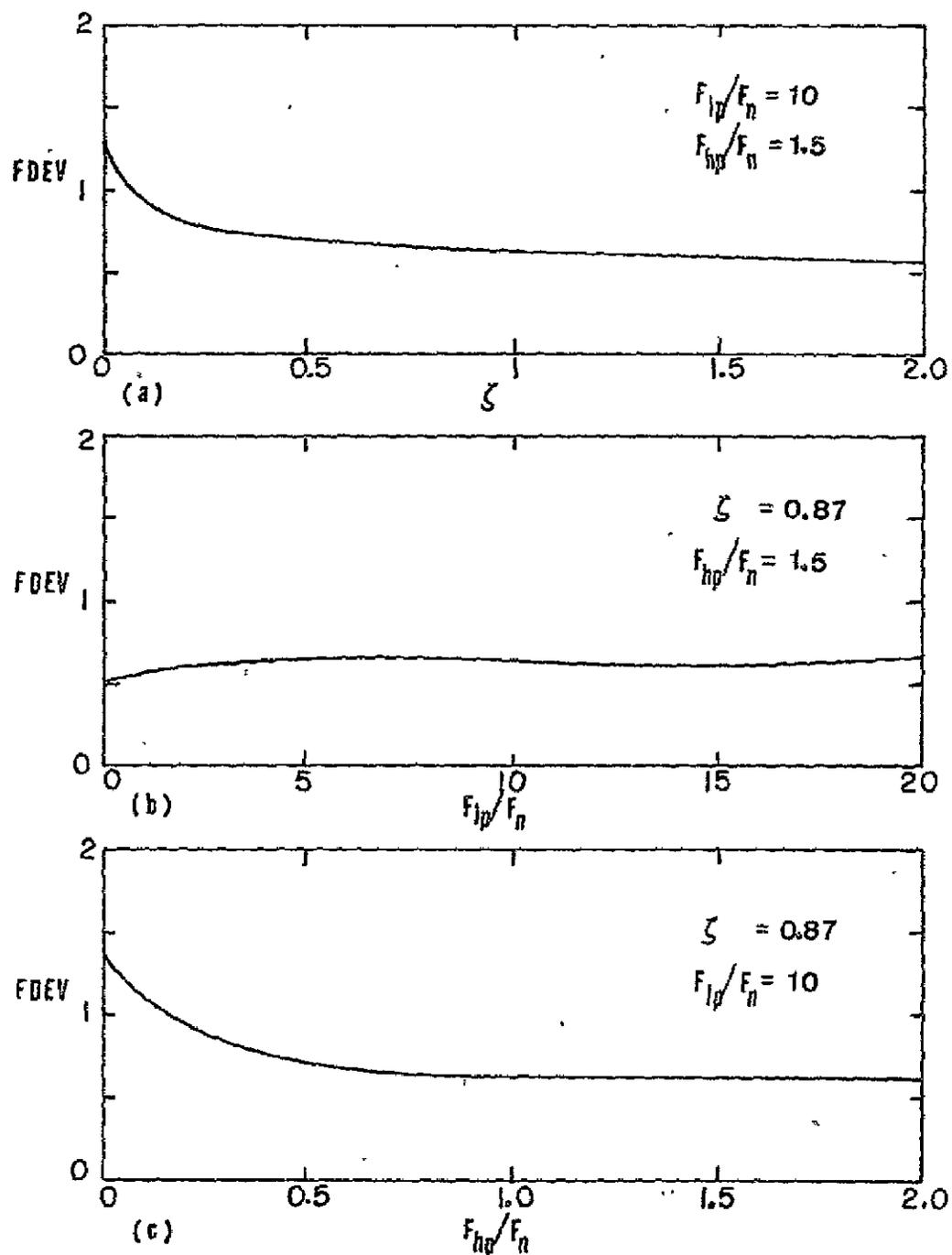
Fig. 23. Frequency domain objective function field for a square pulse: $T_p F_n = 0.3$.

<u>Optimal design for deconvolution criterion</u>. Chrono-
logically, it was at this point that the deconvolution ap-
proach emerged and that the composite results of Figures 17-
22 were completed for that set of transducer variables.

Optimal system design for deconvolution used TDEV of
equation. (15) as the objective function (to be minimized) and
the penalty functions of equations (17) to reflect the con-
straints. Comprehensive results are given in Table 2 (with
annotations) and Figures 24-25 for a range of pulse shapes
and durations. The more exhaustive studies of Figure 24 were
made with triangular and cosine input pulses, lengths from
$0.3/f_n$ to $20/f_n$. Because of generally similar results and
the relatively greater computational effort required with
rectangular pulses, fewer studies were made with long rec-
tangular pulses.

The design strategy was to initiate the search using
known typical designs and signals, for which the results of
Figures 17-22 provided the basis. Because of the lengthy
computations, subsequent searches were initiated at these
'better' points using finer criteria for locating the opti-
mum. The general trend of coarse vs precise optima can be
seen in Table 2. Note that in Table 2 and in Figures 17-22,
25, that the magnitude of the objective TDEV are low for non-
optimized designs, the possible exception being the short
square pulse and very lightly damped system in Figure 17.

TABLE 2

OPTIMAL DESIGN FOR DECONVOLUTION SUMMARY

Pulse Shape	$T*f_n$	Initial values			Final values			No. of Iterations	(Notes), Comments
		ζ	f_{hp}/f_n	TDEV	$\zeta*$	f_{hp}/f_n	TDEV*		
Cosine	0.3	.01	.1	.0807					(1)Fig. 19
	0.3	2.0	0.9	0.00756	1.63	1.80	0.00756	1	Flat field
	1.0	1.8	0.01	0.00753	-0.013	1.73	0.00722	3	Strange: T pulse = $1/f_n$
	3.0	1.8	0.01	0.00745	2.01	1.94	0.00740	6	
	7.0	1.8	0.01	0.00135	1.98	1.43	0.00110	1	No improvement
	8.0	.01	.1	.0156					(1) Fig. 22
	8.0	2.0	0.9	0.00119	1.81	1.15	0.00113	8	
	10.0	1.8	0.01	0.00195	1.44	0.88	0.000968	7	
	10.0	1.5	0.7	0.000982	1.44	0.88	0.000968	7	Confirmation Test
	13.0	1.8	1.8	0.000960	1.96	1.90	0.000255	6	
	17.0	1.8	0.01	0.00131	1.71	1.06	0.000268	4	
	17.0	1.5	0.9	0.000447	1.71	1.06	0.000268	5	Confirmation Test
	20.0	1.5	0.9	0.000462	1.45	0.87	0.000252	4	
Triangular	0.3	.01	.1	0.0637	1.91	1.98	0.0068		(1)Fig. 18
	1.0	1.8	0.01	0.00682	-0.03	1.89	0.00661	7	Strange: T pulse = $1/f_n$
	3.0	1.8	0.01	0.00671	1.85	2.00	0.00666	6	
	7.0	1.8	0.01	0.00393	1.97	1.49	0.00183	8	
	8.0	.01	.1		1.55	1.58	0.0018		(1) Fig. 21
	10.0	1.8	0.01		1.206	1.206	0.00160	2	Incomplete: Time limit
	17.0	1.8	0.01	0.00114	1.46	1.46	9.000614	7	
	20.0	1.8	0.01	0.00128	1.40	0.94	0.000635	6	
Square	0.3	.01	.1	0.155					(1) Fig. 17
	0.3	2.0	0.9	0.0573	2.0	0.9	0.0537	7	Flat field
	8.0	.01	.1	.0314					(1) Fig. 20
	8.0	.01	.1	.0314	1.66	1.43	.0262		Fig. 26
	8.0	0.01	0.01	0.0499	1.93	0.859	0.0443	4	Supplemental Run
	8.0	1.6	1.6	0.0436	1.47	1.53	0.0436	7	Incomplete: Time limit

Note (1) Current practice design, see respective Figures 17-22.
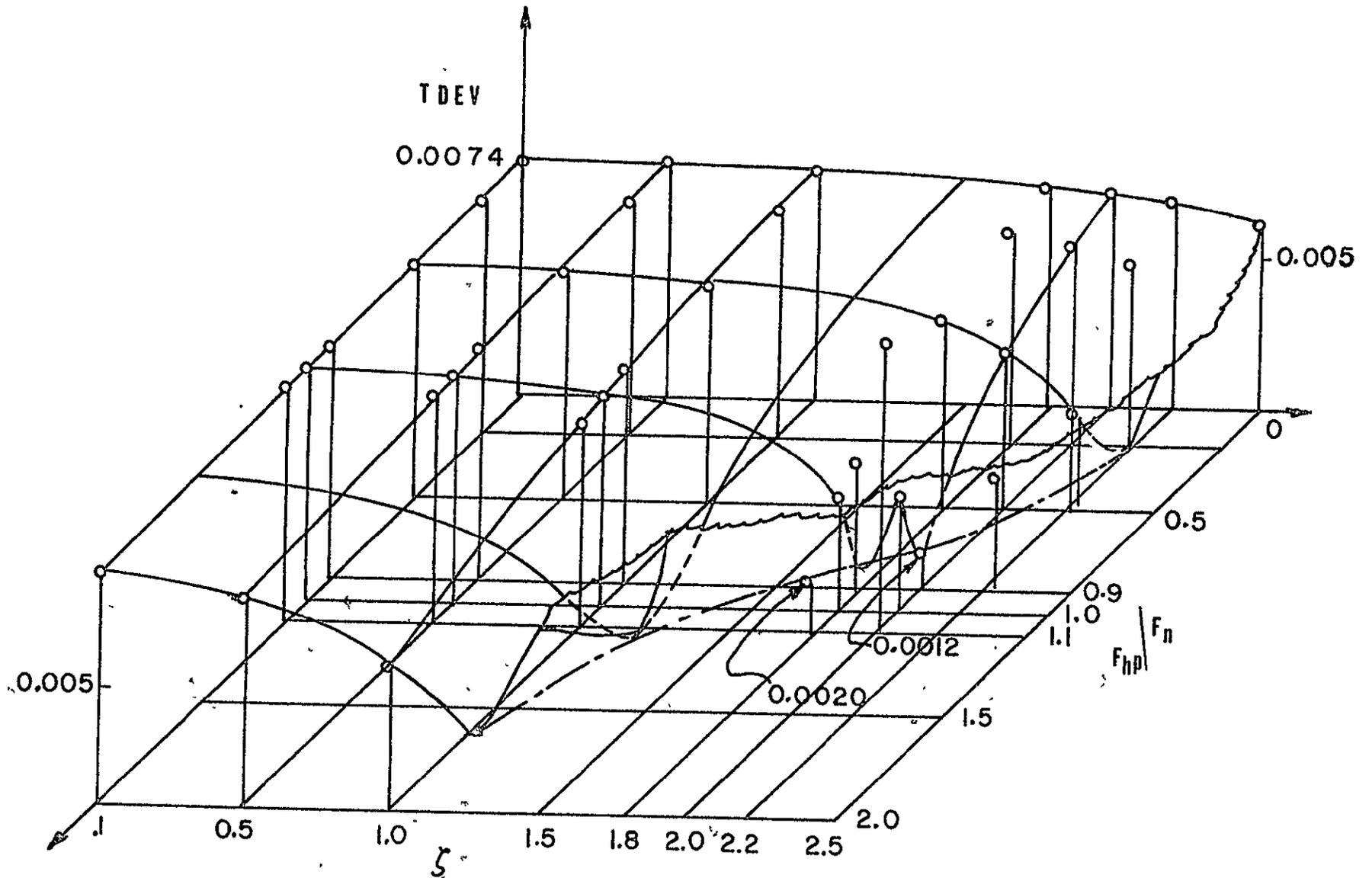
Fig. 24. Time domain objective function field for a
long cosine pulse: $T_p F_n = 8.0$.
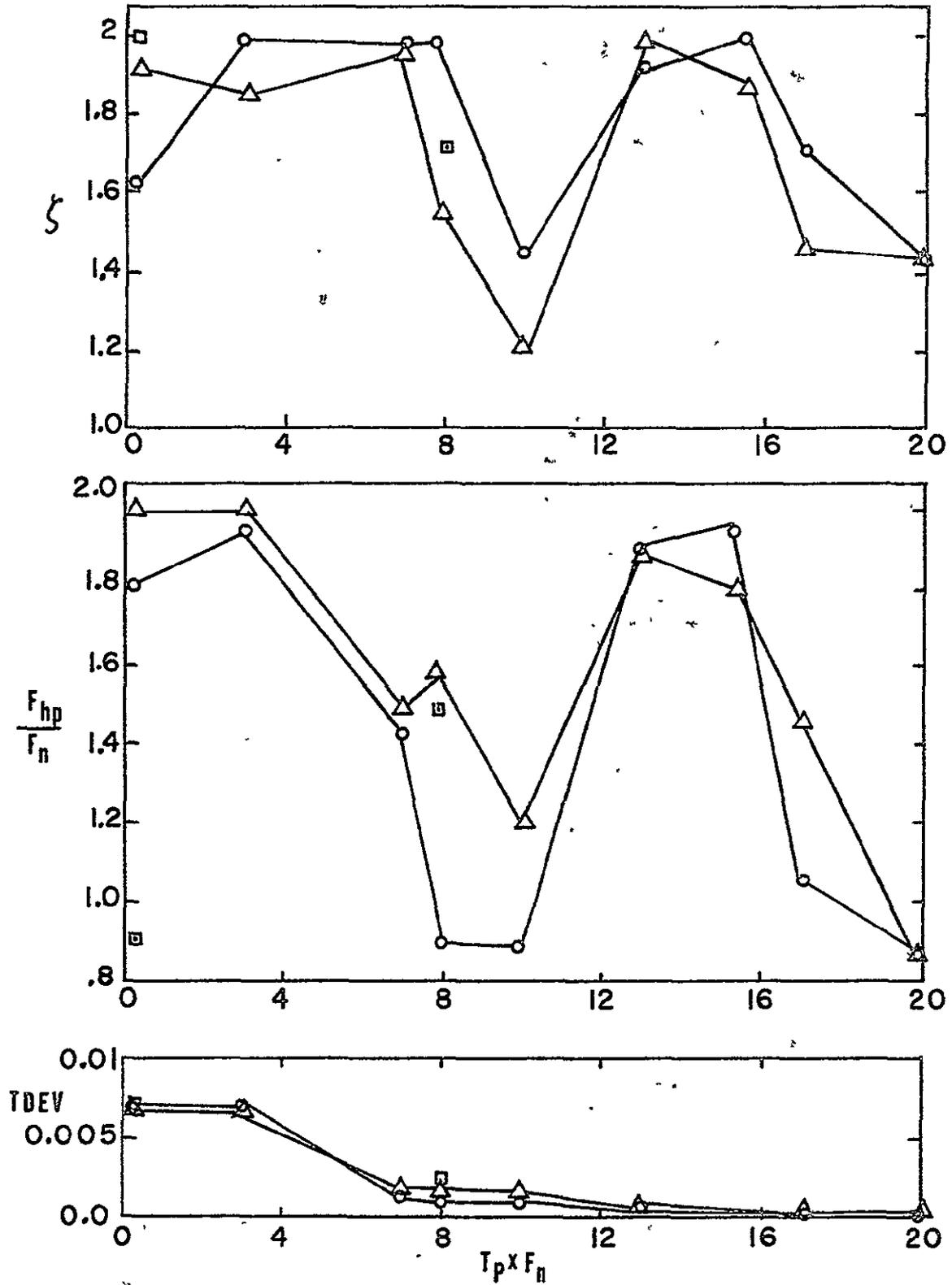
Fig. 25. Summary of optimal designs for triangular (Δ), square (□) and cosine (o) pulses of various lengths.

Nevertheless, in some instances the relative change is quite substantial. As it turns out and as might be anticipated, numerical implementation of the deconvolution algorithm also can affect the magnitudes of the results, but not the relative values.

The extremely low values of TDEV for the optimal designs are desirable. It is seen in Figures 24 and 25 that the optima depend to some extent upon the nature of the signal and can therefore be chosen to maximize information relevant to the signal type expected or sought. It is notable that the optimal transducers are generally quite overdamped and the high-pass filter frequency corner is above the transducer natural frequency (or low-pass cutoff) for all cases, i.e., $f_{hp} > f_n$. Accordingly, significant attenuation results, but it is a known quantity and never exceeds the attenuation constraint. This also minimizes the 'ringing' and possible false counts of other methods. In Table 2, it is seen that poor results are obtained if the pulse length is about equal to the transducer time constant; this is the only case in which a lightly-damped transducer ($\zeta = .01$) shows to advantage. It would appear that this is a situation to be avoided.

A comparison of the objective function fields for the frequency domain and time domain objectives in Figure 23 and Figures 24 and 25 respectively gives some indication of the degree of success one can expect using the optimal design

approach (within our ability to graphically display the results). That is, although deconvolution for systems with a wide range of transducer damping ratio and time constant and high frequency filter corner gives very good results for the simple known test signals of this study, optima do exist and may be essential in dealing with unknown signals where the only known data is transducer system output Z_4 (in Figure 3). The objective function field shape for the time domain solutions is shown in Figure 24 for the long cosine pulse $Txf_n = 8.0$. Calculated points are indicated by circles, and contours indicated are as suggested by a number of trial points. The existence of a long narrow trough with a relatively flat valley floor is interesting. Such valleys have been observed to cause design problems in most texts on optimal design.

Figure 26 shows a specific example which is representative of the general situation: an optimal transducer-filter system for deconvoluting a long rectangular pulse $Txf_n = 8.0$. (This is also a 'difficult' case.) The optimal design has $\zeta^* = 1.66$; $f_{hp}/f_n^* = 1.43$, with $TDEV^* = 0.0262$. The search was initiated with the design of Figure 20. The design is within the region described by the penalty functions. This is significant, since it can be assumed that at least one minimum is not limited by the constraints, i.e., the practical constraints do not exclude all relative minima. Comparing Figures 20(a) and 26(a) one can see a significant

Fig. 26.   Square pulse: $\zeta = 1.66$; $F_{hp}/F_n = 1.43$; $T_pF_n = 8.0$.

improvement in the 'optimally' deconvoluted pulse even though the value of objective function only changes from 0.0314 to 0.0262; that is, the human eye perceives a better match of the deconvoluted pulse and the original pulse. Figures 20(b) and 26(b) show the Fourier spectra for these two systems. In Figure 26(b), the output Y_4 clearly shows a reduced tendency for 'ringing' of the transducer and false counts as pointed out above. The transducer damping predictably influences the $f_n x T_p = 8$ region. Also, note that FDEV (the frequency spectrum criteria of equation (14) has increased for the optimal deconvolution solution.

As further tests of (a) frequency vs deconvolution criteria and (b) the optimal design approach, Figures 27-30 are presented. Figures 27 and 28 compare deconvoluted results for a sequence of different long pulses (relative to transducer time constant), with the system output Z_4 superimposed. Figures 29 and 30 show the same comparison for a sequence of short pulses. Figures 27 and 29 are for the 'conventional' system described above; Figures 28 and 30 are for the 'optimal' system.

Figures 26-30 clearly show the significance of the deconvolution approach to transient pulse signal analysis, regardless of optimization. These clearly corroborate the previous figures for cases where there may be residual effects of different pulses and unknown times of occurrence. The transducer output Z_4 is obviously useless as a means for
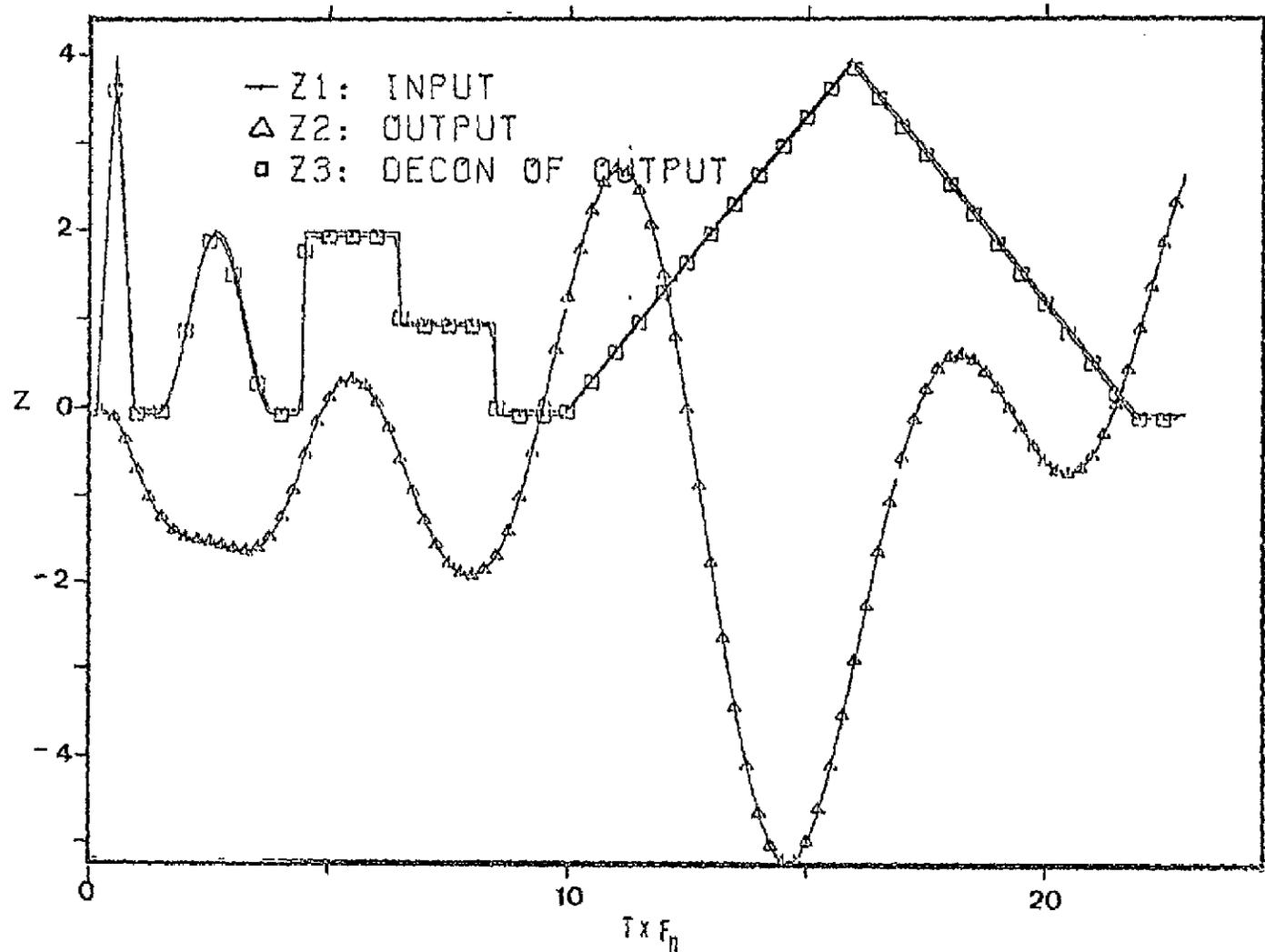
Fig. 27. Deconvolution of a family of short pulses;
$\zeta = 0.01$; $F_{hp}/F_n = 0.1$.
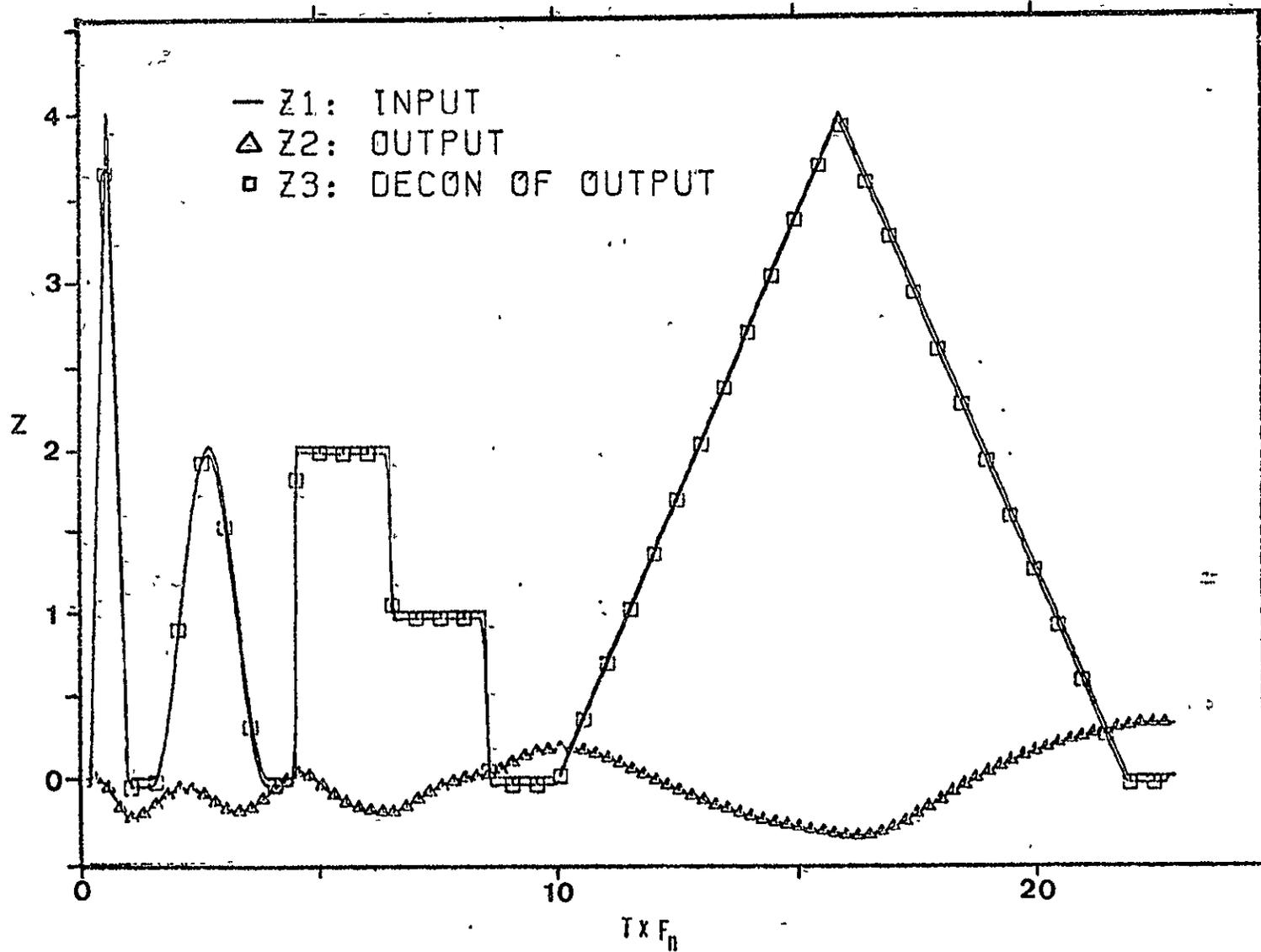
Fig. 28. Deconvolution of a family of short pulses;
$\zeta = 1.66$; $F_{hp}/F_n = 1.44$.
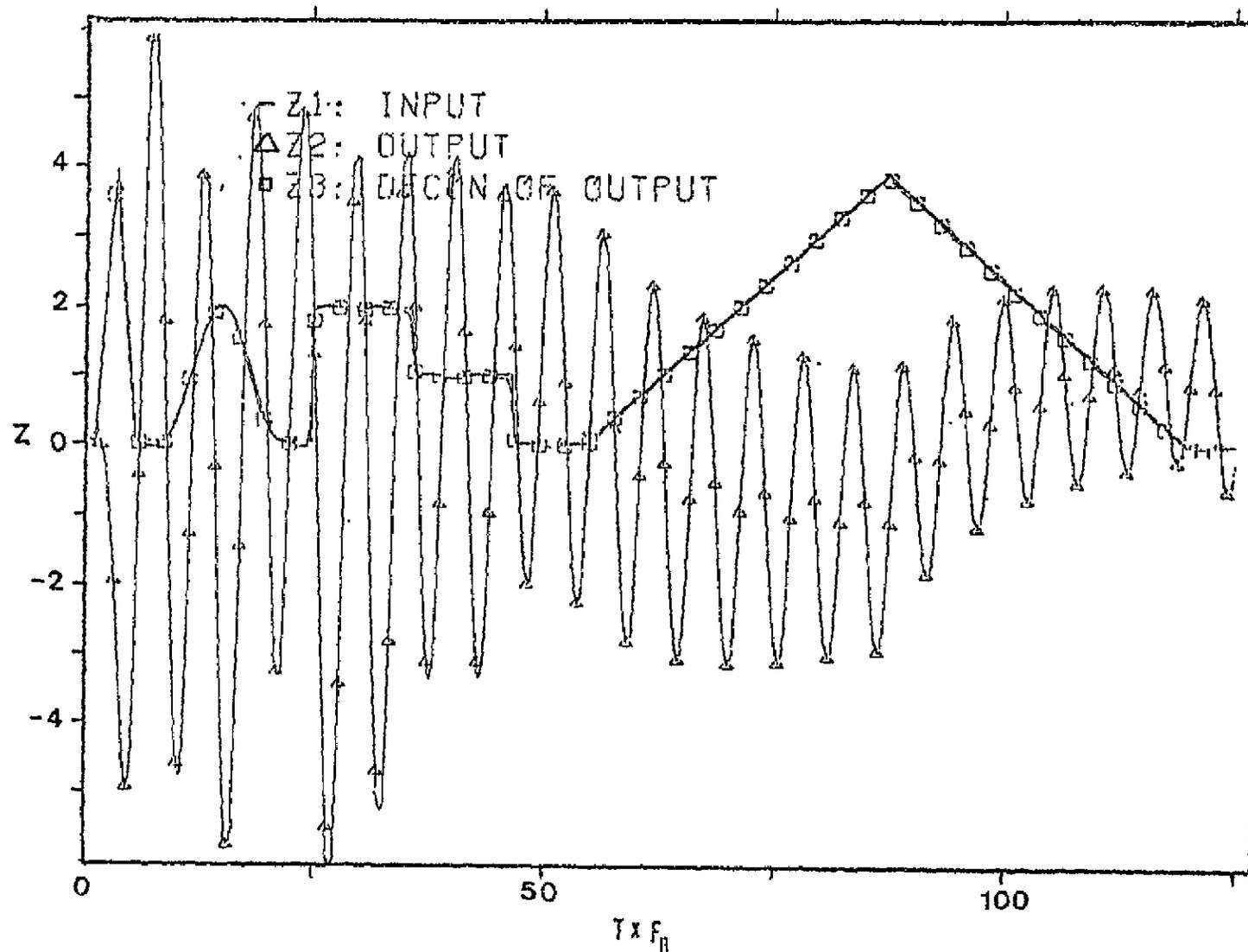
Fig. 29.   Deconvolution of a family of long pulses;
$\zeta = 0.01$; $F_{hp}/F_n = 0.1$.
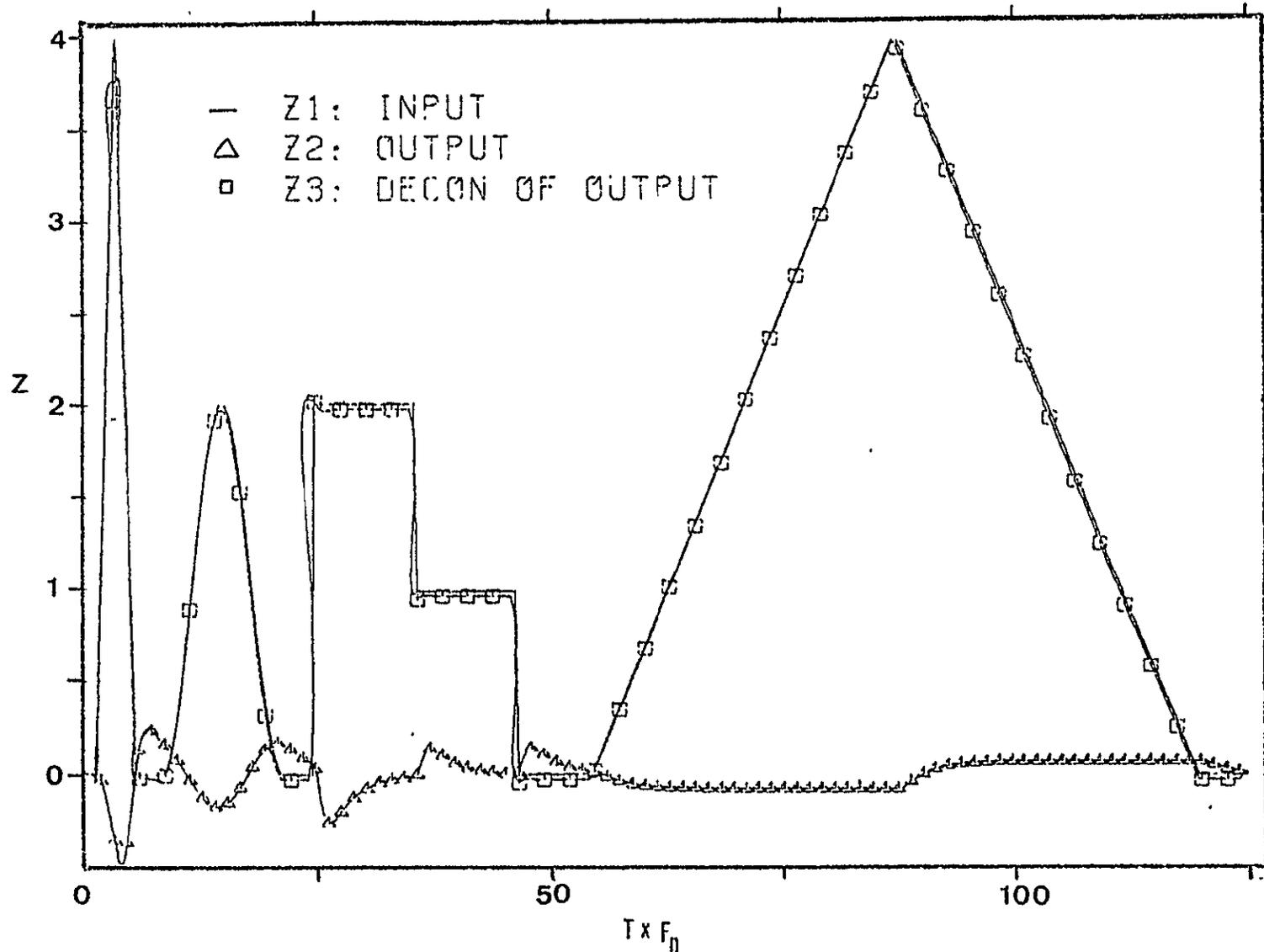
Fig. 30. Deconvolution of a family of long pulses;
$\zeta = 1.66$; $F_{hp}/F_n = 1.44$.

distinguishing the height and shape of pulses. Deconvolution of the transducer signal closely reproduces the shapes in the pulse train.

Within the accuracy of the figures, the differences between the conventional and the optimal deconvolutions are almost imperceptible. In general, most current acoustic emission transducers are for pulse counting and are described as having 'high Q' resonance (i.e., low damping ratio), and their associated filters are set to pass only the fundamental resonant frequencies. Thus, pulse-counting pickups can be used for pulse deconvolution in the time domain with a slight degradation of the information. However, the optimal design studies show that for best pulse shape deconvolution, the damping of the transducer should be greater than critical damping, and the high-pass filter corner should be above the resonant frequency. The differences may be significant when dealing with real signals, as previously suggested.

Comparison of Figures 1 and 2, the sample AE recordings, with Figure 29, suggests that a pulse counting acoustic emission system would count significantly more than the actual number of defect acoustic events. Note that if the natural frequency of the transducer is greater than or less than the f_n used for the derivation of Figure 29, then the AE counting system would indicate a correspondingly higher or lower count respectively. Hence, the intuitive lack of correlation of AE counts and the number of defect events is

theoretically verified and is shown to be due primarily to the resonant response of the system rather than a response to the actual defect.

Summary of Optimal Design for
Measurement System

Deconvolution of a pulse has been demonstrated to be a superior approach for transient pulse analysis. Reshaping of a transducer output back to the original input pulse is possible and gives an accurate representation of the generating pulse in the time domain. If the transducer response curve has a low frequency cut-off or if high-pass filters are used in the measurement system, then the DC components of a pulse will be absent from the output signal. This characteristic of AE measurement systems frequently makes the pulse shape virtually unrecognizable in the time domain. Frequency analysis methods have been tested and shown to be similarly ambiguous for segregation of different pulse shapes. Using deconvolution, in principle any definable transducer and filter system can be used to reconstruct pulse characteristics, i.e., to generate time domain signatures.

The following major points about the selection of design variables have been demonstrated.

1. Any definable transducer and filter system can be used for measurement of pulses by means of the deconvolution method. The time domain signature thus generated becomes the basis for analysis.

2. The use of a low-pass filter for frequencies above the transducer natural frequency is unnecessary.

3. The output pulse shape (Z_2 in Figure 1) for a pulse duration shorter than half the transducer natural period is relatively insensitive to the shape of the input pulse.

4. The frequency spectrum of the signal output from a measurement system with filtration of low frequency components relative to the frequency spectrum of the original pulse is significantly different such that most criteria for comparison of these spectra may not be meaningful.

5. The deconvolution method can 'bring back' information about the original pulse even after filtering. This method was operational for the pulses of short duration for which the frequency spectra of all pulse shapes were similar. Optimization can improve these results, but may not be necessary.

6. There is a wide and relatively level plateau for the relative standard error between an input pulse and the deconvoluted output pulse, per Figure 24. Within this area designers will be nominally successful for many choices of the design variables. In general the shapes of the input pulses do not have a significant influence on the determination of the optimum design location.

7. Item 5 and 6 above notwithstanding, there are families of optimal selections for transducer and filter system parameters which give superior deconvoluted output signals. These may be significant when working with actual hardware and unknown characteristics.

The optimal design results (ζ^*, f_{hp}/f_n^*) are certainly new and different from the expectations of engineers accustomed to working in the field of signal conditioning. In obtaining these results modern rational design techniques on a rather complex design problem have been demonstrated. Acoustic emission transducer manufacturers describe their pickups as having a high Q resonance, or low-damping ratio, and their filters are set to pass only the fundamental resonant frequencies. The optimal design study has shown that

acoustic emission pickups can be used for pulse deconvolution in the time domain with a slight degradation of the information, but that for best pulse shape deconvolution the damping of the transducer should be larger than critical damping and the high-pass filter corner should be above the resonant frequency.

CHAPTER IV

DECONVOLUTION OF EXPERIMENTAL PULSES

Introduction

Deconvolution of experimental data requires that an acceptable mathematical model for each of the components in the measurement system be created. When commercial equipment is available, a frequency response curve is frequently provided or, at a minimum, a specification is given for the bandwidth (± 3 db magnitude limit). Response information such as this or experimental frequency response curves can be used to create component models of arbitrary complexity. After reasonable models have been developed for the transducers, filters, tape recorder and digital event recorder, deconvolution calculations can address the following questions.

1. Can a simple source be found that will produce acoustic emissions with a repeatable shape?

2. Assuming a source with repeatable shape is available, will the output of a given transducer have signals of repeatable or similar shape? If yes, then the deconvolution of the signals should show a repeatable shape representative of the source.

3. When different transducers are used to record AE signals from the same source, will the deconvolution signatures be recognizeable as having come from the same source?

79

4. When more than one AE source is recorded with the same measuring system can the deconvolution signatures be distinguished from each other?

5. Can a major defect, e.g., on a thrust ball bearing race, be detected using the present level of deconvolution signature analysis?

In the following sections, a description of the model equations that were used for the components of the measuring systems are presented. Four sets of experiments are performed in order to evaluate: 1) the reproduceability of the pulse recordings; 2) the relative performance of the transducers; 3) the ability to distinguish between AE sources; 4) the performance of an AE transducer on a ball bearing test rig. The ball bearing tests were conducted using bearings with small slots (defects) cut in the race by electro-discharge machinery, and compared to an undamaged bearing.

Techniques for Testing Transducer Reproduceability for Pulse Recording

The search for an experiment for the evaluation of AE transducers leads to the area of transducer calibrations at high frequencies. Calibration of AE transducers is an unfinished area in the AE industry today. The Acoustic Emission Working Group, a subsection within the American Society of Testing and Materials is actively concerned that the calibration methods should be worked out and eventually published as a proposed standard. Experiments in the literature use different approaches to evaluate an AE transducer or an AE experiment. These are summarized as follows.

Grinding of glass powder

Graham and Allers (8) described an experiment they used to simulate an AE source similar to growing cracks. An electric drill was used to grind and break small glass fragments held in a socket. This was a repeatable source and the frequency response curves were similar to that of an AE from a gowing defect in metals.

Capacitive transducer as a standard

Graham (8) and Breckenridge (23) have described experiments in which a highly sensitive capacitor plate directly above the specimen surface has been used to detect single-shot AE signals. The capacitive transducer output can be compared to a piezoelectric transducer's output, and a calibration curve for different frequencies can be derived. The disadvantages of this experiment are: the pulses must be large to get a significant signal from the capacitive transducer, and the AE measurements are usually of through transmissions, i.e., longitudinal waves, whereas <u>the significant AE signals picked up by AE transducers are thought to be predominantly surface waves or Rayleigh waves</u>.

Electric spark discharge

Bell (24) discharged a high-voltage electric spark from an electrode to the metal test specimen. This experiment was considered a similar excitation as in·AE crack growth situations and produces the required Rayleigh waves. The major

advantage is that the AE event was individual and unique. Feng (25) improved on the spark discharge experiment by adding a second electrode. Thus the pulse from the discharge is only acoustically coupled to the specimen and from there onto the transducer. Dr. Feng's experiment is used by Dunegan/Endevco for the frequency response curve provided with each AE transducer. The spark discharge can be a short Dirac-type pulse when it leaves the electrode area, but the mechanical medium of the plate used for transmitting the wave to the transducer can have several resonant frequencies and some mode conversions. The wave that passes under the transducer cannot be expected to be a short-duration pulse, but it can be shown to be repeatable.

Ultrasonic transducer driven as a steady state energy source

Prior to spark discharge, Dunegan/Endevco used the ultrasonic driver directly coupled back-to-back with an AE transducer for their calibration experiment. This experiment excites an entirely different set of resonant frequencies, and the frequency response curves are significantly different than the response curves from an electric spark discharge. The longitudinal coupling was thought to be responsible for some of the major differences. This observation may also hold true for the capacitive transducer calibration.

One of the significant problems in AE transducer cali-
brations is that the measurement system is intended to look
through a very high frequency window, typically 50-350 kHz
The frequency range is well above the first and second reson-
ant frequencies of the mounting block and transducer case.
The frequencies are also well beyond the upper limit, approx-
imately 20 kHz, of laboratory verifiable sine-wave steady
state acceleration.

Of the various evaluation experiments described above,
the spark discharge method of Feng seems to be the best for
the purposes of this study. It is portable; it has a demon-
strated repeatability and it can be used for on-the-site
calibration of the transducer.

Electrical Spark Discharge for Acoustic Wave Calibration

Two spark calibration probes were built and tested for
this project. The first had 12-inch leads from the capacitor
to the electrodes and the electrodes were mounted 180° from
one another. This design produced considerable electromag-
netic interference in the area of the experiment and appeared
to have multiple discharges during each event. A discussion
with engineers working on spark-discharge experiments in the
Vanderbilt Chemical Engineering Department revealed that
there can be a problem with fields interacting with the dis-
charge when the electrodes are mounted at 90° and at 180°.
Thus, to avoid reverberations during the discharge, the

electrodes should be mounted at an angle between 89° and 85°.
The second spark-probe design was constructed with much
shorter leads from the capacitors to the electrodes, and the
angle between the tungsten electrodes was approximately 88°.
The capacitance was 0.025 μF, and the power supply was
current-limiting to provide 10 μA at 3500 volts. A photo-
graph of the spark probe over a specimen and of the experi-
mental setup with the power supply is shown in Figure 31.

Setup of spark probe and data
collection procedure

The procedure for collection of spark discharge data
was as follows.

1. Set the spark gap at 0.5 mm, the power supply volt-
   age at 3,500 volts and place the probe over the
   fatigue crack tip on the compact tensile specimen.

2. Record the transducer output signals as they come
   in at a frequency of approximately ten per minute.
   The recorder tape speed was 60 ips for a 100 to
   300,000 Hz recording band.

3. Play the recorded signals back and identify the AE
   burst on the oscilloscope, noting the footage
   counter value at each pulse.

4. Replay the pulse with the tape speed at 1 7/8 ips
   and capture the leading edge of the burst with the
   digital event recorder at 100,000 samples per
   second.

5. Play back the captured pulse on the X-Y-T plotter
   to determine if the stored pulse is satisfactory
   and complete. For the best results the digital
   event recorder should be used over the full ampli-
   tude range of ± 5 volts on ± 128 steps.

6. Assign the pulse an identification and record it
   by punching it on paper tape. The identification
   code is N.TOOP where N is the number of pulses
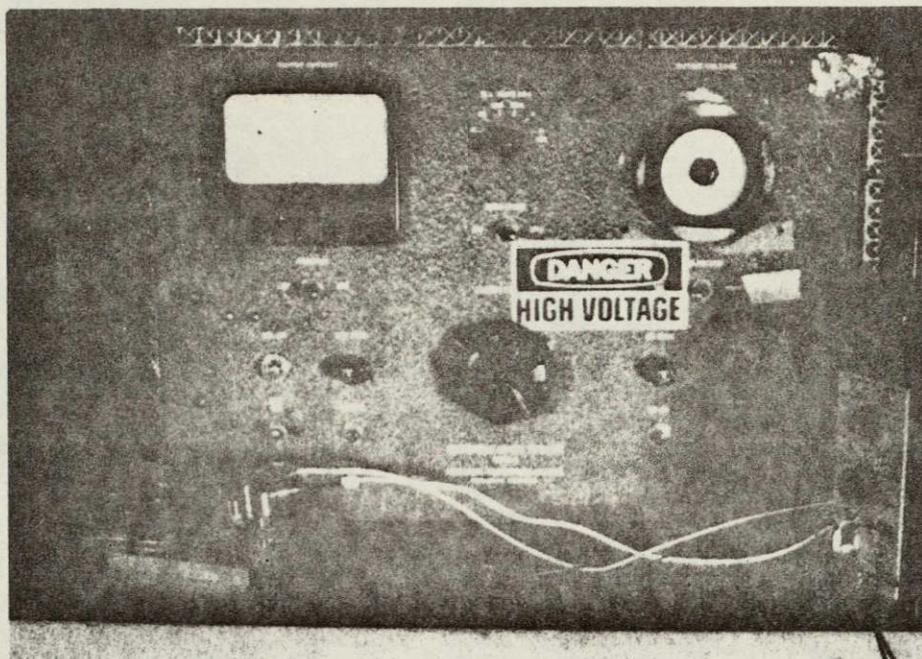
Fig. 31. Photograph of the spark discharge setup.

recorded in this mode, T is the type of test iden-
tification and P is the transducer identification.

7. Convert the binary words on the paper tape to ASCI
code with a special computer program worked out on
a PDP 8 minicomputer, and teletype punch a new
tape.

8. Feed the ASCI coded tape for the particular pulse
via a teletype terminal into the DISC storage of
the larger computer in preparation for the decon-
volution computation and Fourier frequency analy-
sis.

Mathematical Models for Digital Event Recorder, Tape Recorder, Amplifier and Transducer Components

The deconvolution equations used in the computational

routines were built up from a differential equation of the

component, or from a Bode Diagram curve fitting procedure.

The Bode Diagram approach makes it possible to recreate a

differential equation of the model from the experimental

frequency response curve of the component.

The deconvolution model was originally conceived of as

a single inverse transfer function that would take the signal

in one mathematical step back to the original, or starting,

shape. In the process of the evolution of this experiment,

the differential equation model went well beyond an eighth-

order differential equation, which meant that the finite dif-

ference derivatives were taking data from time intervals

greater than five data points on each side. See Appendix I,

Table A1. The approach now is to deconvolute stage-by-stage

through each component in turn. This modular approach makes

it possible to change the model for each component as the component is switched for another, or as better frequency response information becomes available and the user thinks that there is justification for changing the mathematical model.

A photograph of the laboratory is shown in Figure 32. The flow of signal information starts on the near end of the bench on the left side and progresses down to the tape recorder and digital event recorder at the far end of the bench. A flow chart of an acoustic emission from the spark discharge probe through all of the system components that were considered to have a dynamic effect on the pulse information is shown in Figure 33. Selected closeups of some of the components are shown in Figure 34.

The equations used to represent the forward-looking transfer function, i.e., the conventional input/output representation, and a brief discussion of the model are presented below. A series of frequency response figures of each component are presented and they include the following information:

1. the manufacturer's response plot for the component, if available

2. experimental check points when they have been made in the Material Science Department's NDT Laboratory

3. the plot for the mathematical model

4. the coefficients used for the mathematical model.
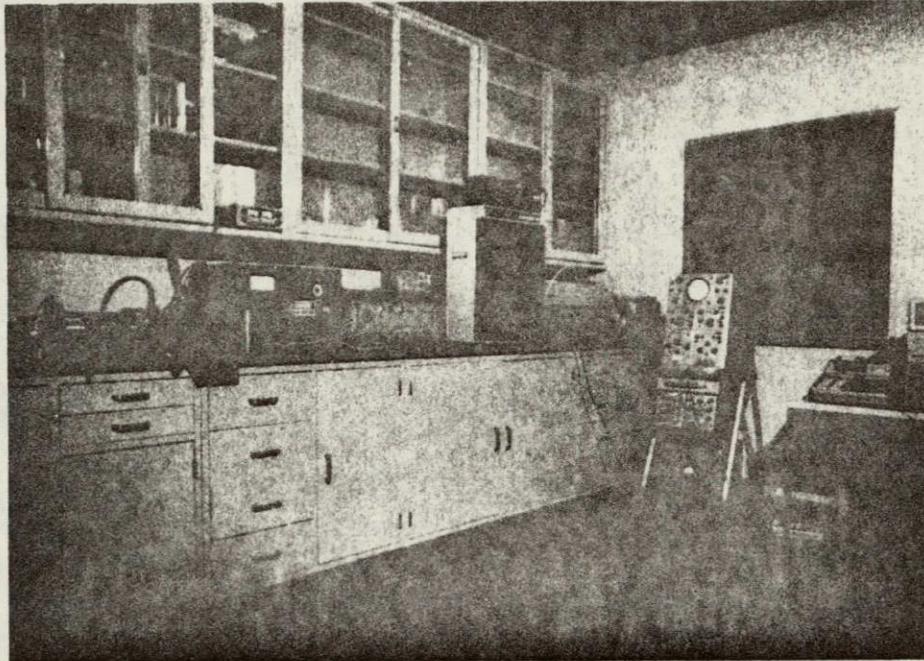
Fig. 32. Photograph of the laboratory setup for acoustic emission research.

```
┌─────────────────┐          ┌─────────────────┐
│  HIGH  VOLTAGE  │          │ SPARK  DISCHARGE│
│  POWER SUPPLY   ├──────────┤     PROBE       │
└─────────────────┘          └─────────────────┘
                                   Z₁
```

Z_1

```
┌───────────────────────────────────────────────────────────┐
│                 SOLID    STRUCTURE                          │
└───────────────────────────────────────────────────────────┘
```

Z_{2a} Z_{2b} Z_{2c} Z_{2d}

| ACCELEROMETER B&K 4339 | ACCELEROMETER B&K 4344 | AE PICKUP D/E D9202 | AE PICKUP PCB 392A |

Z_3

| AMPLIFIER, FILTER B&K 7625 | AMPLIFIER, FILTER D/E 2649 | POWER SUPPLY |

Z_4

TAPE   RECORDER

Ampex   PR 2200

Z_5

| X-Y-T PLOTTER HP 7044A | DIGITAL EVENT RECORDER B&K Type 7502 | OSCILLOSCOPE Tektronix 555 |

Z_6

PAPER TAPE PUNCH
B&K Type 6301

Binary   8 bit   tape

COMPUTER
DEC PDP8

ASCII coded paper tape

Fig. 33.   Flow diagram of the components used for the
spark discharge measurements with four different transducers.
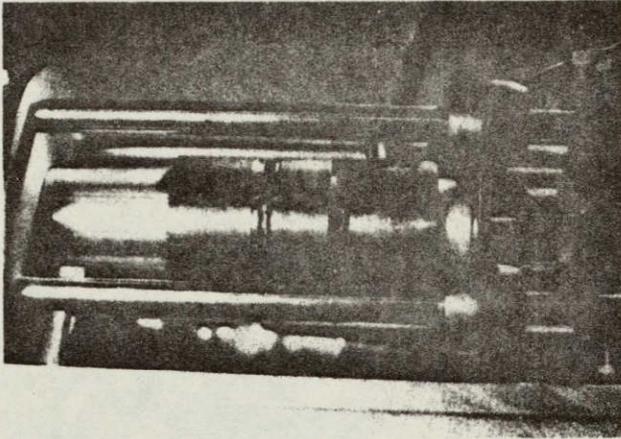
a) Closeup of ball-bearing rig
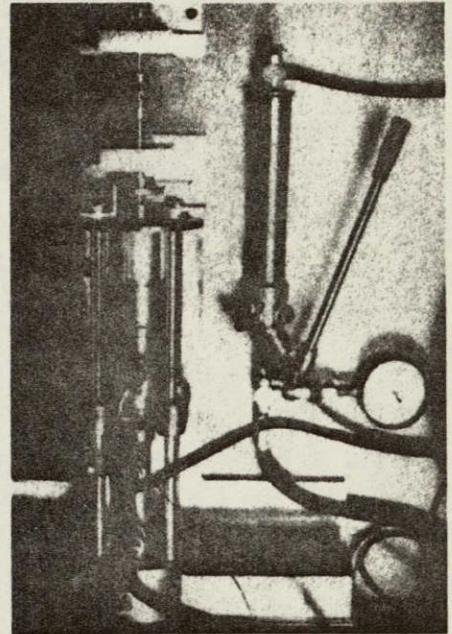
b) Ball-bearing rig

c) Tape recorder
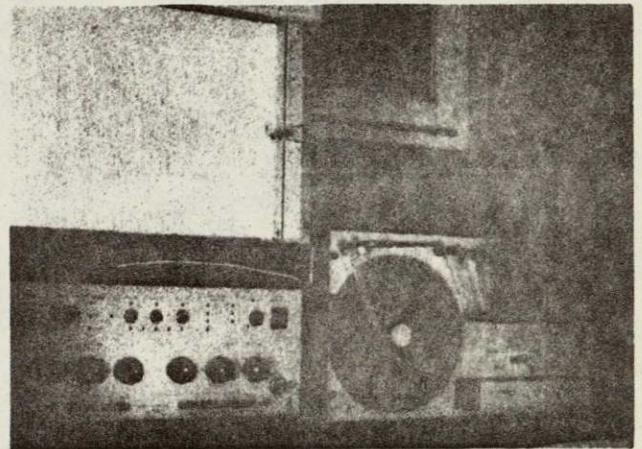
d) Digital event recorder, x-y plotter and paper tape punch

Fig. 34. Photographs of selected components used in the acoustic emission experiments.

The transducer models received the most attention and, in each case, a different model was selected than that suggested by the manufacturer's literature. The reason for this discrepancy may be the way in which the manufacturer derives his natural frequency data for publication or it may be due to the way in which the transducer is mounted on the structure. As will be explained later in this chapter, the natural frequencies used for the model were selected by examination of the Fourier spectrum of the pulses recorded during the spark calibration experiment. A summary of the transducer parameters are shown in Table 3 with the manufacturer's valu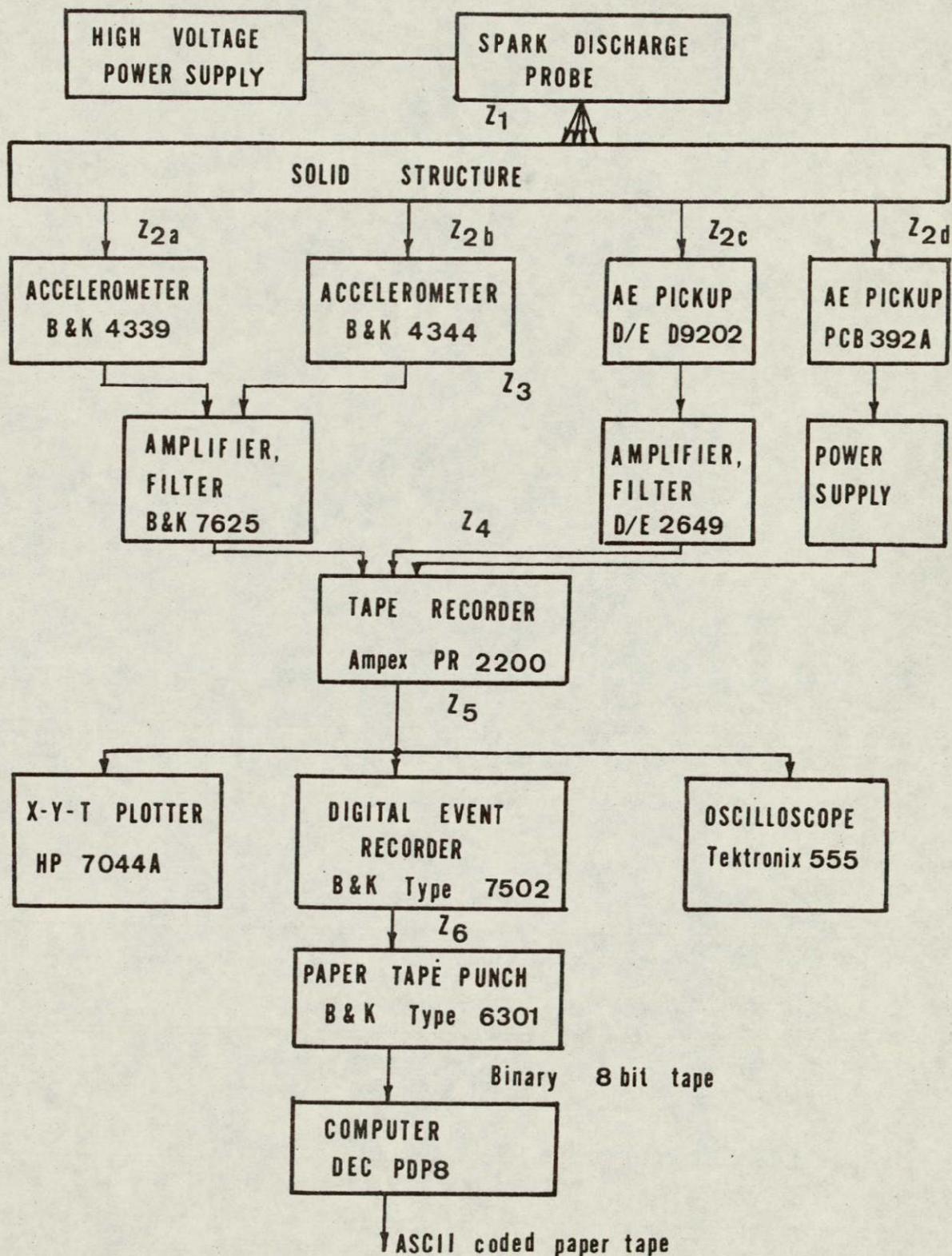es in the first column and the final model values in the second column. Each of the models for the transducers used had two resonant frequencies and one of these usually fell near the natural frequency given by the manufacturers except for the Dunegan/Endevco AE transducer which is specified by the manufacturer in a different manner.

Digital Event Recorder

This component was responsible for a cluster of high frequency signals around the digitization frequency (3.2 mHz) in a region at half the digitization frequency (1.6 mHz), and at one-fifth digitization frequency 0.64 mHz. The model shown below was used for deconvolution purposes to eliminate the one-fifth digitization frequency. The two higher frequencies were present but did not interfere in the results

TABLE 3

TRANSDUCERS USED FOR EVALUATION OF ACOUSTIC EMISSION PULSES

Manufacturer	Model No. Serial No.	Resonant Frequencies Specified (kHz)	Experimental (kHz)	Damping Ratio	Low-Pass Frequency (kHz)
Dunegan/Endevco San Juan Capistrano, CA	D9202 AB11	350-800	98 & 180	0.05	45
Bruel & Kjaer Cleveland, OH	4344 552940	128	70 & 128	0.01	0.005
Bruel & Kjaer	4339 349554	32	28.5 & 68	0.01	NA
PCB	392A 118	NA	NA		NA

NA = information not available.

significantly. The equation for the digital event recorder is

$$\frac{Z_6}{Z_5} = \frac{\omega_{D1}\omega_{D3}^2 (D+\omega_{D2})^3}{\omega_{D2}^3 (D+\omega_{D1}) (D^2+2\zeta_D\omega_{D3}D+\omega_{D3}^2)} \qquad (18)$$

The signal location Z_5 and Z_4 are indicated in Figure 33 and a plot of the frequency response is shown in Figure 35.

Tape Recorder

$$\frac{Z_5}{Z_4} = \frac{F_{RECORD}\omega_{T2}^2 D}{(D+\omega_{T1}) (D^2+2\zeta_T\omega_{T2}D+\omega_{T2}^2)} \qquad (19)$$

A plot of the frequency response and identification of the coefficients used for the particular solution of (19) is shown in Figure 36. A simple check of the frequency response was made in the laboratory and these results are also shown on the plot.

Amplifier and Filter

$$\frac{Z_4}{Z_3} = \frac{F_{FILTER}D}{(D + \omega_{F1})} \qquad (20)$$

The coefficients and the frequency response plot for the two filters used are shown in Figures 37 and 38.
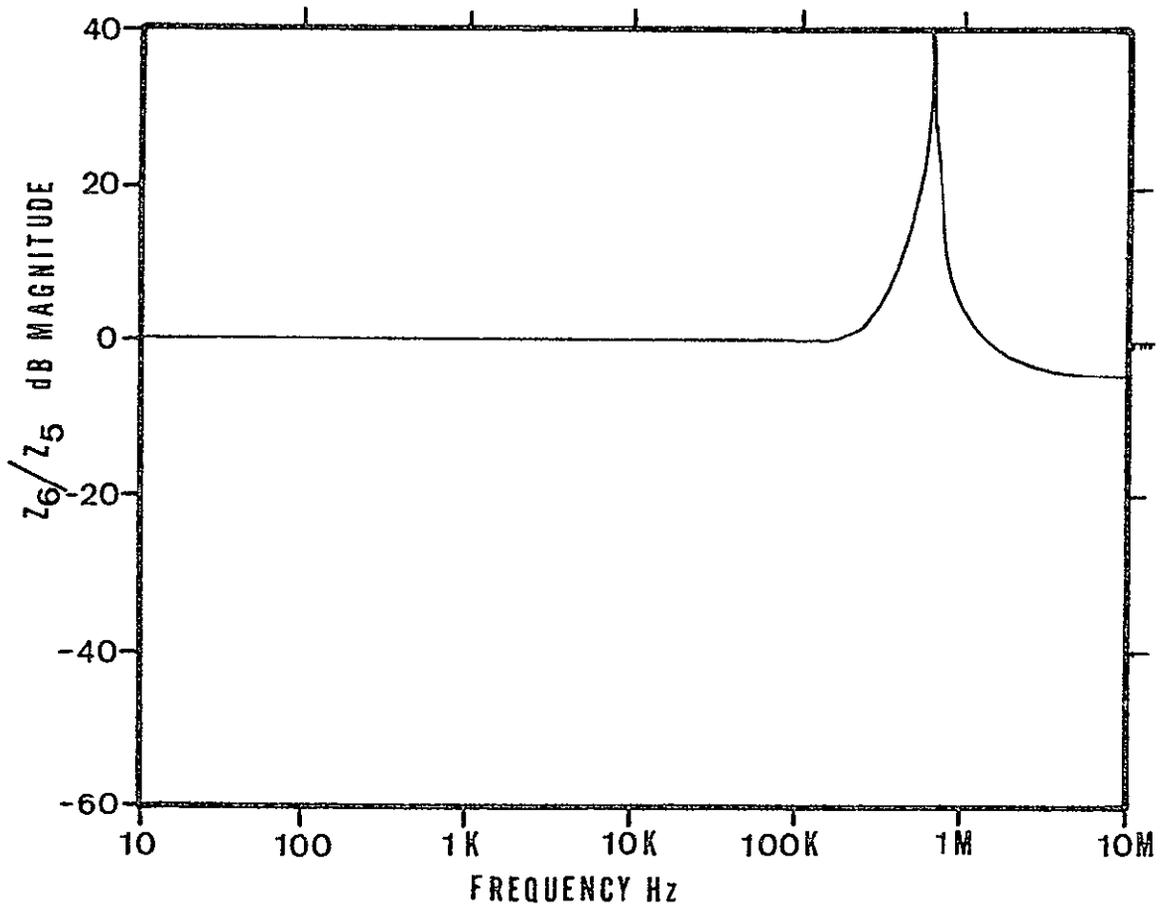
COMPONENT· Digital Even Recorder

TYPF: Bruel and Kjaer Model 6301

MODEL EQUATION:

$$\frac{z_6}{z_5} = \frac{(\omega_{D1}\,\omega_{D3}{}^2/\omega_{D2}{}^3)(D + \omega_{D2}{}^3)}{(D + \omega_{D1})(D^2 + 2\,\zeta_D\,\omega_{D3}\,D + \omega_{D3}{}^2)}$$

where $\omega_{D1} = \omega_{D3}\,0.6$

$\omega_{D2} = \omega_{D3}$

$\omega_{D3} = (0.2/dt)\,2\,\pi$

dt = time increment on digitized record

Figure 35 Digital event recorder characteristics and model.
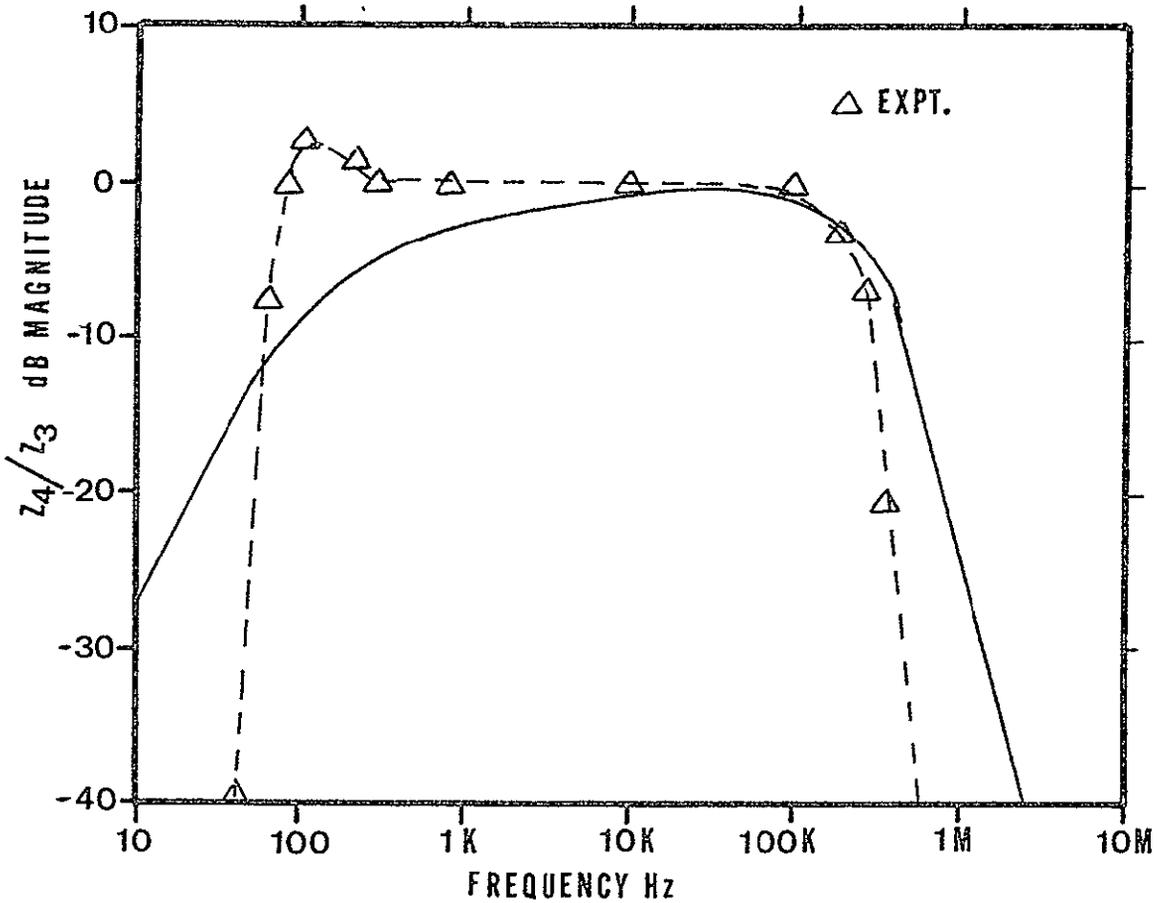
COMPONENT: Tape Recorder

TYPE: Ampex Corp. PR 2200
        Tape Speed.   60 in/s
        Amplifiers: Direct recording 300-300,000 Hz pass band

MODEL EQUATION:

$$\frac{Z_4}{Z_3} = \frac{F_{record} \ \omega_{T2}^2 \ D}{(D + \omega_{T1})(D^2 + 2 \zeta_T \omega_{T2} D + \omega_{T2}^2)}$$

where
$$F_{record} = 1.0$$
$$\omega_{T1} = 100.0 \times 2 \pi$$
$$\omega_{T2} = 300,00 \times 2 \pi$$
$$\zeta_T = 1.0$$

Figure 36   Tape recorder characteristics and model.
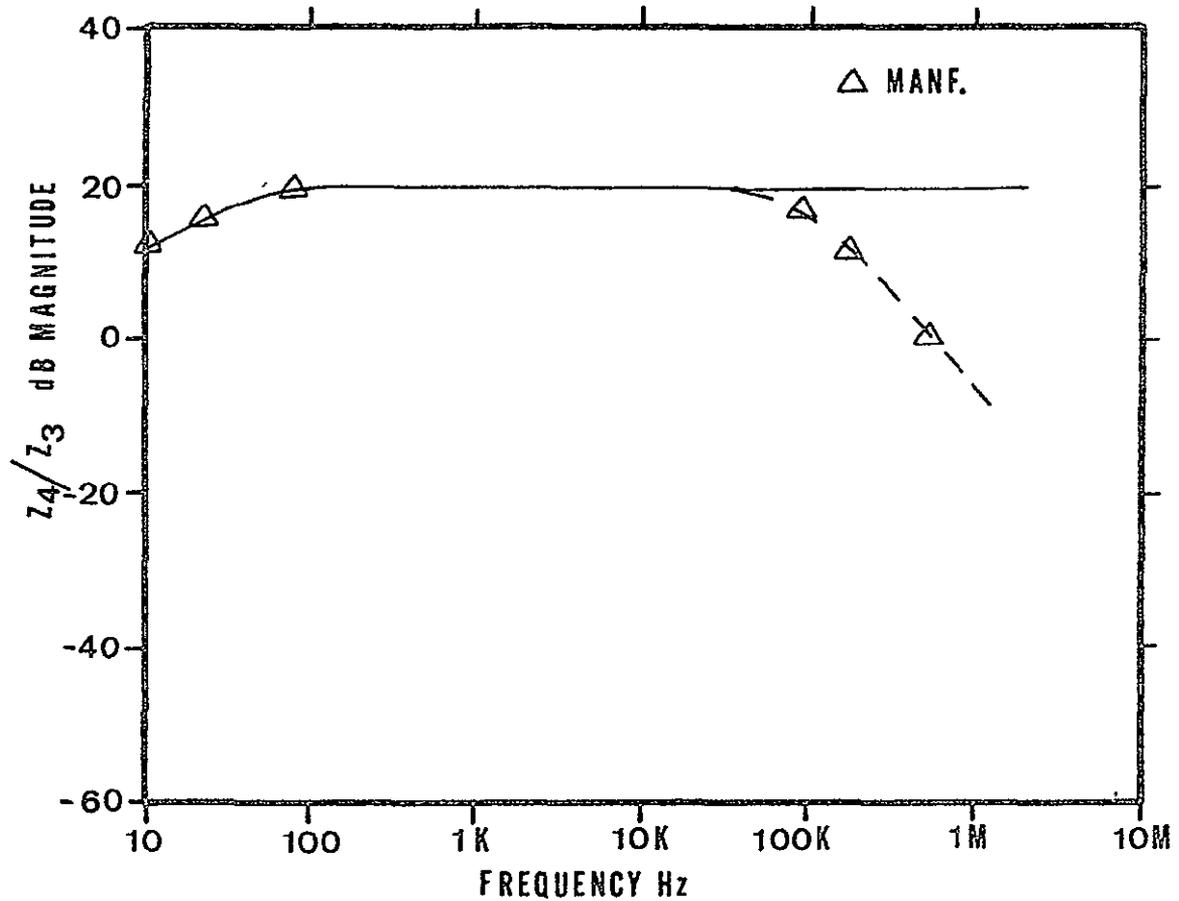
COMPONENT: Amplifier and Filter

TYPE: Bruel and Kjaer Type 2625

MODEL EQUATION:

$$\frac{Z_4}{Z_3} = \frac{F_{filter} \, D}{D + \frac{\omega}{F1}}$$

where $\quad F_{filter} = 10.0$

$$\frac{\omega}{F1} = 5. \times 2 \pi$$

Figure 37 Amplifier and filter characteristics and model for Bruel and Kaerj Type 2625 system.
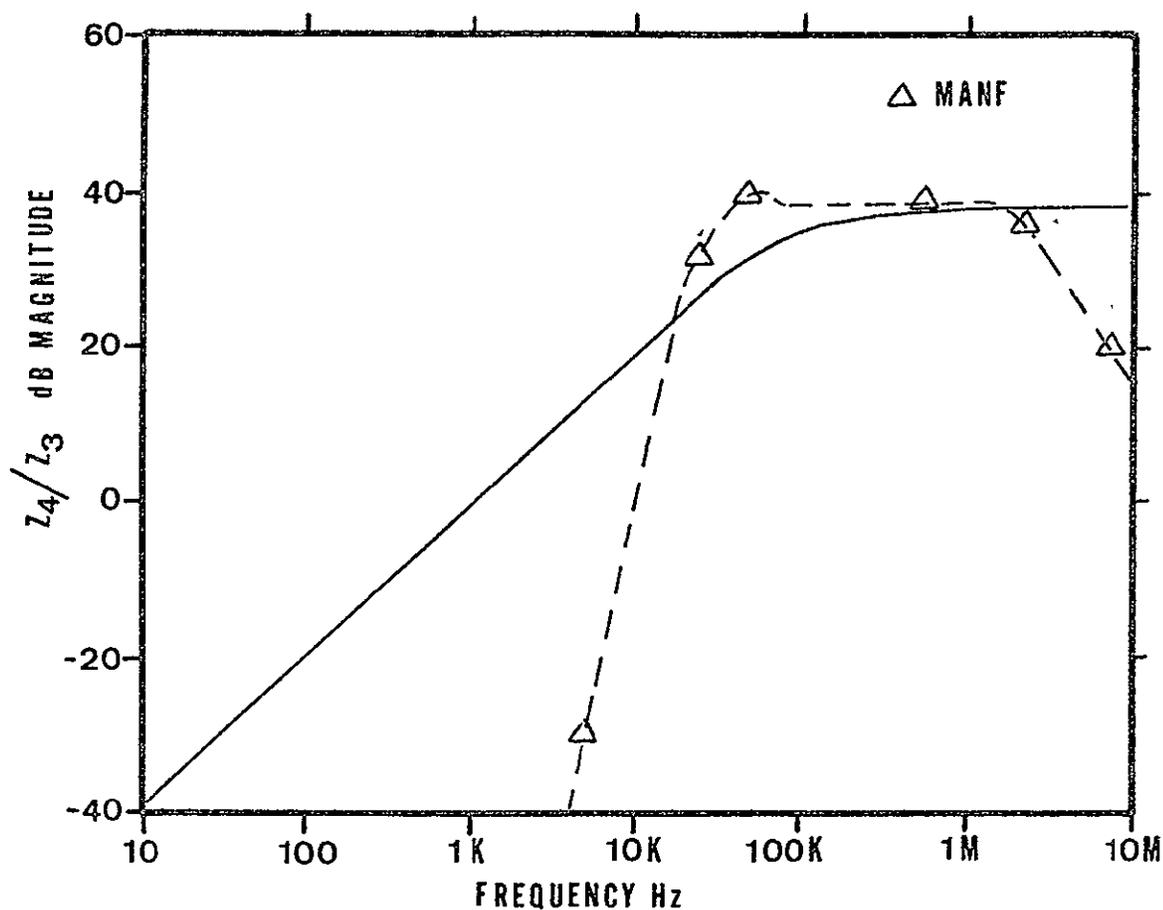
COMPONENT: Amplifier and filter

TYPE: Dunegan/Endevco Model 2649

MODEL EQUATION:

$$\frac{Z_4}{Z_3} = \frac{F_{filter}^{D}}{D + \dfrac{\omega}{F1}}$$

where

$$F_{filter} = 100.0$$

$$\omega_{F1} = 4,500 \times 2\,\pi$$

Figure 38 Amplifier and filter characteristics and model for Dunegan/Endevco Model 2649 system.

Transducer

The first transducer model had a single degree of freedom as used in the analytical development in Chapters II and III and the value for f_n was taken from the manufacturer's literature. When the spark discharge repeatability experiments were conducted (discussed in detail in the next section), the Fourier spectrum of the recorded trace was seen to have two or three predominate frequencies near the transducer f_n value. See Figures 47 and 52. The deconvolution plots using the manufacturer's value for f_n were not considered acceptable and a better value for f_n was located from the Fourier spectrum plots. After several trials two of the predominate frequencies on these plots were selected as representative of the transducer and were used for the mathematical model coefficients. The model equation is as follows:

$$\frac{Z_3}{Z_2} = \frac{F_{PU}\omega_{P1}^2\omega_{P2}^2}{(D^2+2\zeta_1\omega_{P1}D+\omega_{P1}^2)(D^2+2\zeta_2\omega_{P2}D+\omega_{P2}^2)} \tag{21}$$

The coefficients and frequency response plots for the models of the three transducers used are shown in Figures 39 to 41. The response curve suggested by the manufacturer's information is also included on each plot for reference purposes.

Compact Tensile Test Specimen

The model developed for the aluminum plate compact tensile specimen is an approximation arrived at as follows.
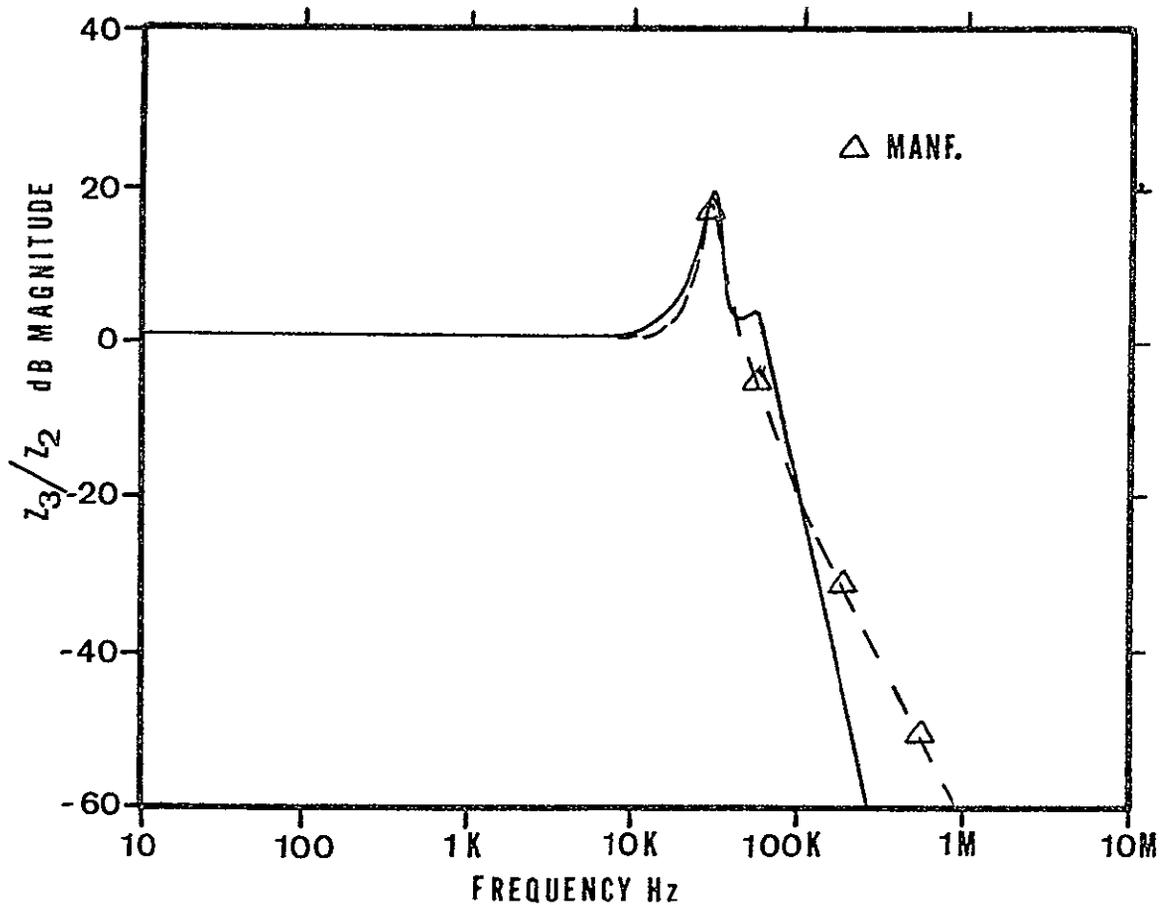
COMPONENT: Accelerometer transducer

TYPE: Bruel and Kjaer Model 4339 s/n 349554

MODEL EQUATION:

$$\frac{Z_3}{Z_2} = \frac{F_{pu} \, \omega_{P1}^2 \, \omega_{P2}^2}{(D^2 + 2\zeta_1 \omega_{P1} D + \omega_{P1}^2)(D^2 + 2 \zeta_2 \omega_{P2} D + \omega_{P2}^2)}$$

where

$$F_{pu} = 1.2 \ mV / M/ s^2$$

$$\omega_{P1} = 28,500 \times 2 \pi$$

$$\omega_{P2} = 68,000 \times 2 \pi$$

$$\zeta_1 = 0.01$$

$$\zeta_2 = 0.01$$

Figure 39 Transducer characteristics and model for Bruel and Kjaer Model 4339 accelerometer.
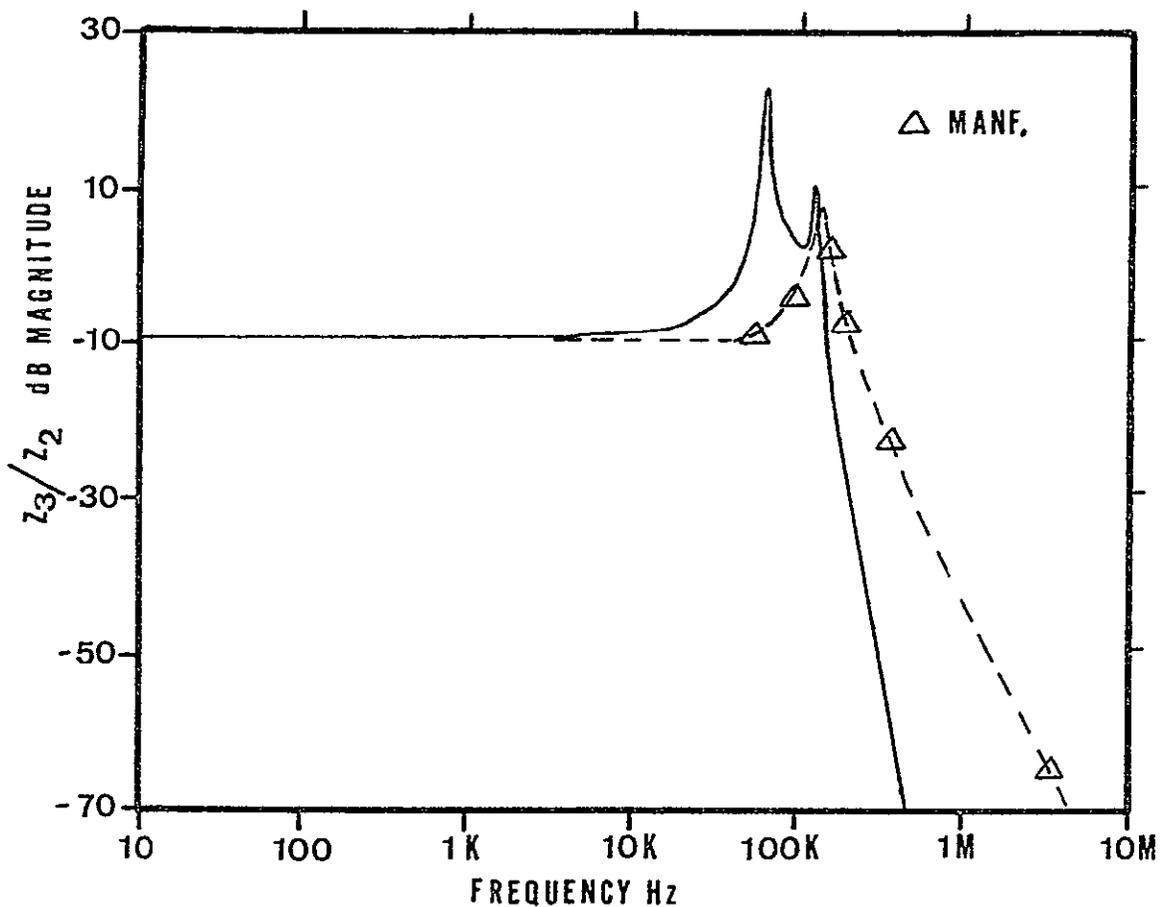
COMPONENT: Accelerometer transducer

TYPE. Bruel and Kjaer Model 4344 s/n 552940

MODEL EQUATION:

$$\frac{Z_3}{Z_2} = \frac{F_{pu}\, \omega_{P1}^2\, \omega_{P2}^2}{(D^2 + 2\zeta_1 \omega_{P1} D + \omega_{P1}^2)(D^2 + 2\zeta_2 \omega_{P2} D + \omega_{P2}^2)}$$

where F_{pu} = 0.324 mV / m/ s

ω_{P1} = 70,000 x 2 π

ω_{P2} = 128,000 x 2 π

ζ_1 = 0.01

ζ_2 = 0.01

Figure 40 Transducer characteristics and model for Bruel and Kjaer Model 4344 accelerometer.
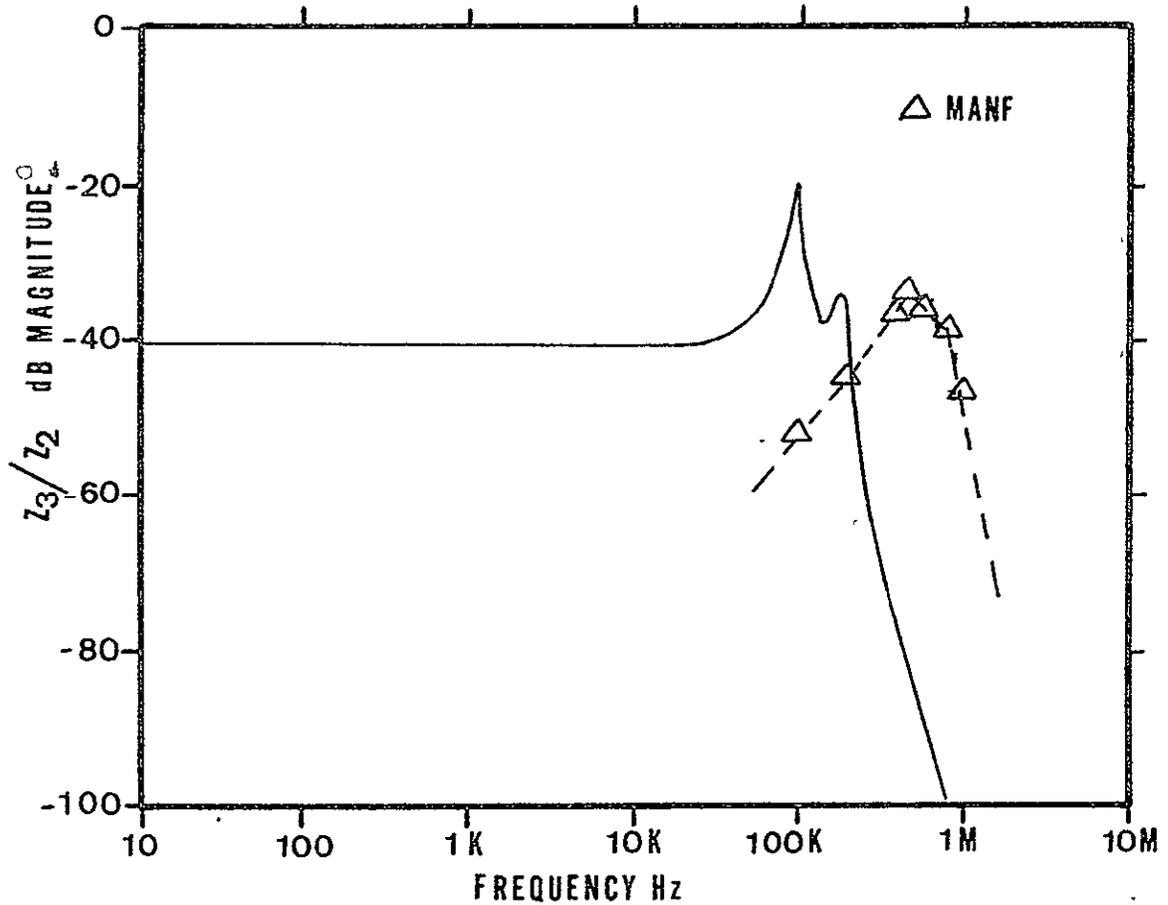
COMPONENT: Acoustic Emission Transducer

TYPE: Dunegan/ Endevco D 9202 s/n AB11

MODEL EQUATION:

$$\frac{Z_3}{Z_2} = \frac{F_{pu}\,\omega_{P1}^2\,\omega_{P2}^2}{(D^2 + 2\zeta_1\,\omega_{P1}\,D + \omega_{P1}^2)(D^2 + 2\zeta_2\,\omega_{P2}\,D + \omega_{P2}^2)}$$

where
F_{pu} = 95.0 x 10^{-4}

ω_{P1} = 98,000 x 2 π

ω_{P2} = 180,000 x 2 π

ζ_1 = 0.05

ζ_2 = 0.05

Figure 41 Transducer characteristics and model for Dunegan/Endevco Model D9202 acoustic emission transducer.

1. All of the test traces recorded on the compact tensile specimen with the Dunegan/Endevco transducer were deconvoluted to the base of the transducer (Z_2 in Figure 33). These included traces from the repeatability experiment, different transducers experiment and discrimination between AE sources experiment.

2. A frequency spectrum of each deconvolution trace was computed.

3. Dominant frequencies were identified which appeared in most of the frequency spectra. These were assumed to be resonant frequencies excited by different experiments and thus inherent frequencies in the plate.

4. Another deconvolution step was performed with a model using the frequencies selected. If the frequency spectrum of this deconvolution trace approached the pattern of the frequency spectrum signatures shown in Chapters II and III for analytical pulses, then it was considered to be a viable model for the test specimen.

This model was not considered to be developed enough to give the true deconvolution of the wave shape at the initiation site, but it does serve as an approximation. The model equation for an approximation of the specimen is as follows:

$$\frac{Z_2}{Z_1} = \frac{\omega_{S1}^2 \, \omega_{S2}^2}{(D^2 + 2\zeta_{S1}\omega_{S1}D + \omega_{S2}^2)(D^2 + 2\zeta_{S2}\omega_{S2}D + \omega_{S2}^2)} \tag{22}$$

The frequencies used for the model and the response curves are shown in Figure 42.
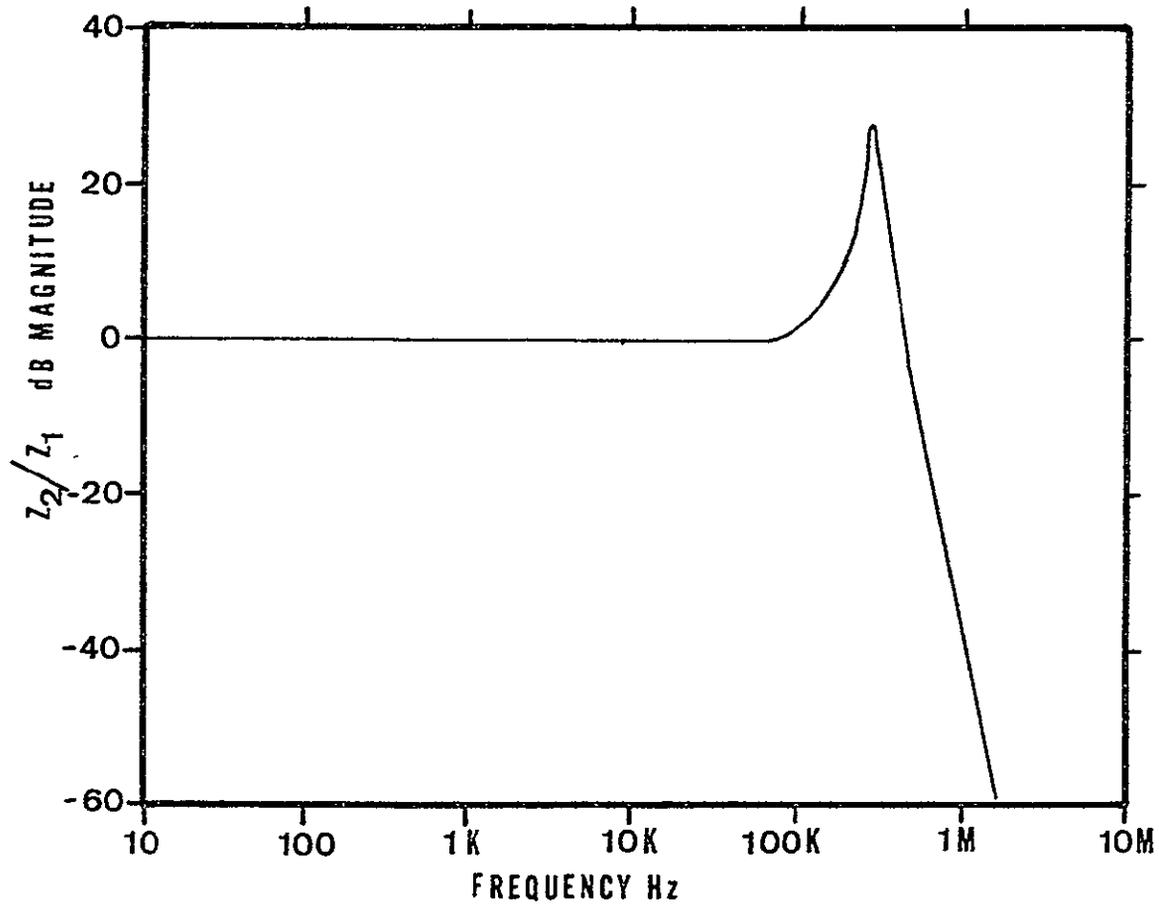
COMPONENT: Compact Tensile Specimen

MODEL EQUATION:

$$\frac{Z_2}{Z_1} = \frac{\omega_{S1}^2 \, \omega_{S2}^2}{(D^2 + 2\zeta_{S1} \omega_{S1} D + \omega_{S1}^2)(D^2 + 2\zeta_{S2} \omega_{S2} D + \omega_{S2}^2)}$$

where

$$\omega_{S1} = 300{,}000 \times 2\pi$$

$$\omega_{S2} = 348{,}000 \times 2\pi$$

$$\zeta_{S1} = 0.01$$

$$\zeta_{S2} = 0.01$$

Figure 42   Flat plate model and characteristic curve derived from the Fourier frequency spectrum curves.

Discussion of the Influence of Deconvolution Procedure with Experimental Traces

Deconvolution is similar to passing a signal through a transfer function that is the inverse of the frequency plots shown in Figures 35 to 42. When this is done, the areas that are attenuated are amplified and vice versa. Thus any noise that is on the tape recording of the pulse will be magnified, particularly if it is at 1 Hz or below. The corrections provided by deconvolution modeling are as much as 200 dB at 1 Hz.

High frequencies such as the digitization frequency and its submultiples are well above the frequency range of the measuring system components, but the deconvolution process picks them up and amplifies these signals by 100 dB or more for frequencies above 2 mHz. This accumulation of high-frequency 'information' was detected during the present work and the low-pass filter was added to attenuate signals above 300 kHz.

As the fall-off rate on the high frequency end of a model and the rise rate on the low frequency end are given steeper slopes in the more complex models to match the experimental response curves, the consequences are an increase in the very high frequency 'information', and an effect similar to DC drift in the very low frequencies. Until these problems are overcome it seems prudent to stay with the simpler models.

Low-Pass Filter

Clusters of high frequency were observed above 400 kHz in the traces after deconvolution through the modules listed above. To keep these from masking possible lower frequency information, a low-pass filter stage was introduced. An extremely rapid roll-off filter was used,

$$\frac{z_{lp}}{z_1} = \frac{\omega_{lp2}^{12}}{(D^2 + \zeta\omega_{lp2}D + \omega_{lp2}^2)^3 (D+\omega_{lp2})^6} \tag{23}$$

It should be noted that this step was not a deconvolution but a means of clearing out frequency information above 300 kHz that was considered to be superfluous. The frequency response of the low-pass filter at one-third the roll-off rate shown in Figure 43.

A block diagram of the executive section of the computational routine is shown in Figure 44.

Construction of models which will duplicate the dynamic behavior of measurement systems is complicated, and the models can become very complex. Models were created that were better fits to the Bode plots shown in the previous figures, but they were not used because of the adverse effects on the pulse information.
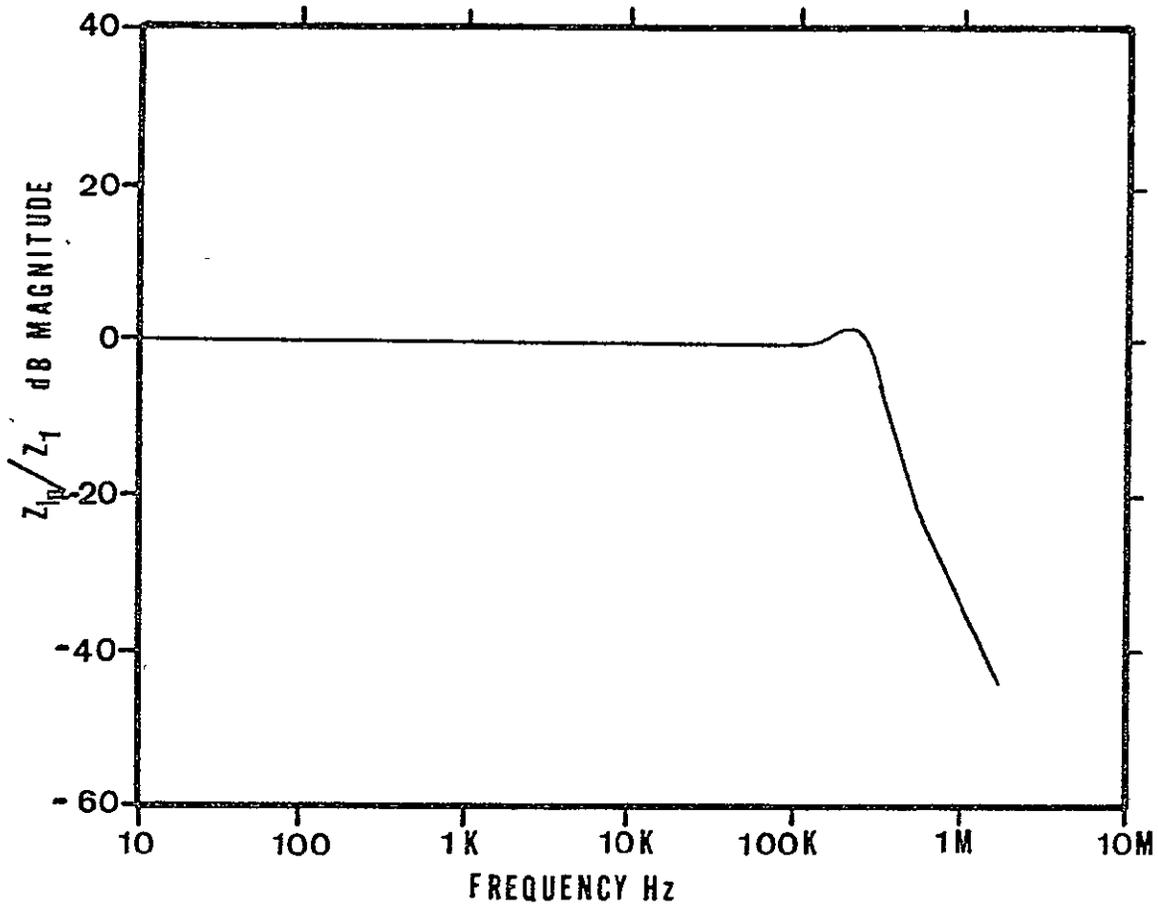
COMPONENT: Filter for Digitization Frequencies

MODEL EQUATION:

$$\frac{Z_{LP}}{Z_1} = \frac{\omega_{LP}^4}{(D^2 + 2\zeta_{LP}\omega_{LP}D + \omega_{LP}^2)(D + \omega_{LP})^2}$$

where

$$\omega_{LP} = 300,000 \times 2\pi$$

$$\zeta_{LP} = 0.2$$

Figure 43 Low-pass filter characteristics and model used for attenuation of digital event recorder frequencies.

START

READ PULSE DATA

$Z_6 \longleftarrow$

$T \longleftarrow$

Add twenty zeros before Z_6 data and
add twenty points at end of data
equal to the last data point of Z_6

CALL DIGITAL EVENT RECORDER
DECONVOLUTION

$Z_6 \longrightarrow$

$Z_5 \longleftarrow$

CALL TAPE RECORDER DECONVOLUTION

$Z_5 \longrightarrow$

$Z_4 \longleftarrow$

CALL AMPLIFIER AND FILTER DECONVOLUTION

$Z_4 \longrightarrow$

$Z_3 \longleftarrow$

CALL TRANSDUCER DECONVOLUTION

$Z_3 \longrightarrow$

$Z_2 \longleftarrow$

CALL STRUCTURE DECONVOLUTION

$Z_2 \longrightarrow$

$Z_1 \longleftarrow$

CALL LOW-PASS FILTER

$Z_1 \longrightarrow$

$Z_{LP} \longleftarrow$

CALL FOURIER FREQUENCY SPECTRUM

$Z_{LP} \longrightarrow$

$Y \longleftarrow$

Remove the last twenty-five computed
points from Z_{LP}

CALL PLOTS

$Z_6 \longrightarrow$

$Z_{LP} \longrightarrow$
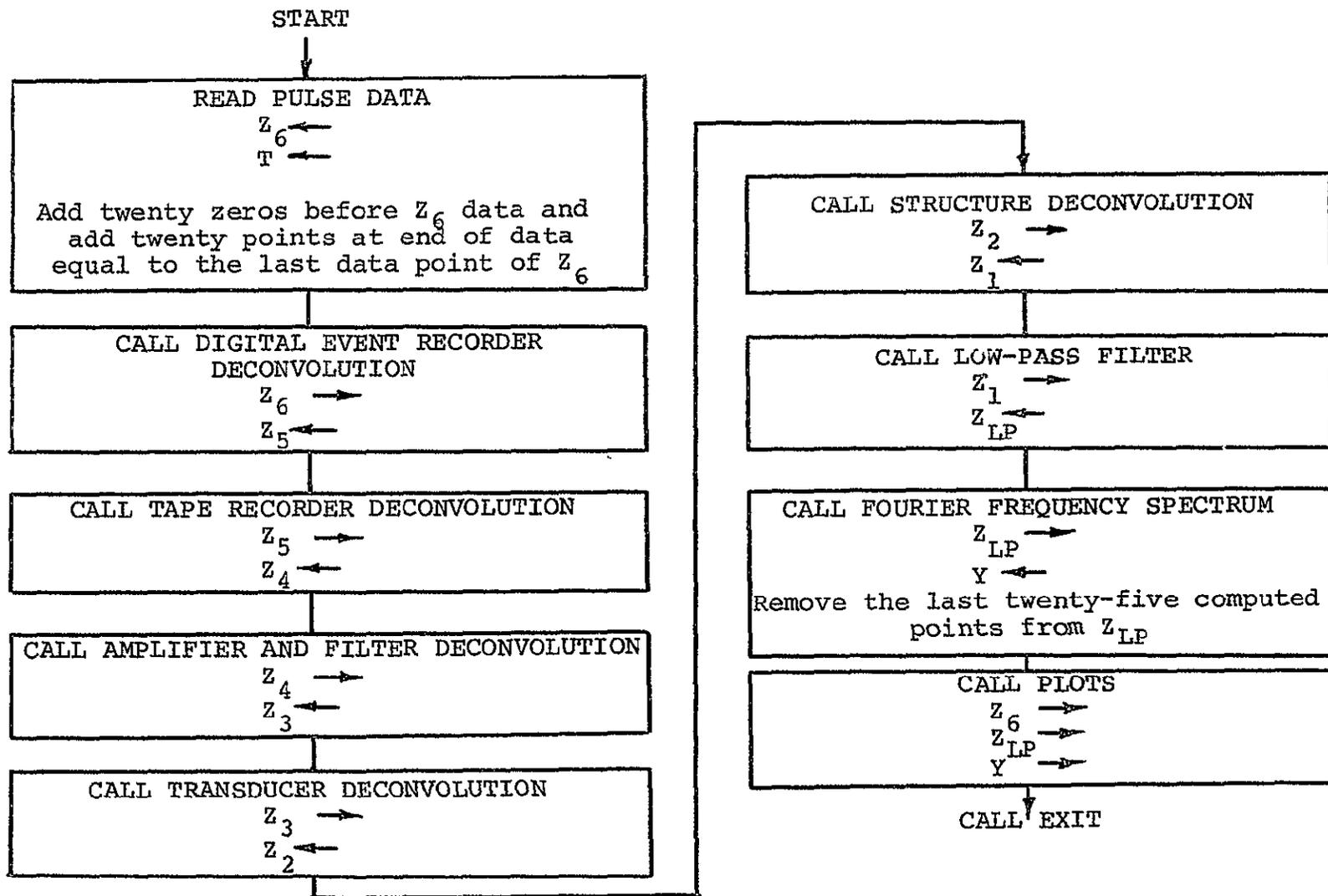
$Y \longrightarrow$

CALL EXIT

Fig. 44. Block diagram of the master computational routine.

Repeatability Experiment

The objective of this experiment was to determine if the output of a transducer has a similar shape when excited by one type of AE generator (Question 2, Chap. II, p. 79). Several records were made of the same event with three different transducer systems. As an example of how repeatable the input pulses were, a set of spark discharge data from the D/E transducer measurement system was computed and the results are shown in Figures 45 to 48. The first figure is of three traces as they are received and the following figures are the frequency spectrum of the as-received traces and the deconvoluted signature of the same traces. Comparing the two figures one would say that the as-received pulses are more alike than the deconvoluted pulses. The overall image of the pulses in Figure 47 is similar and the small disparities are attributed to the fact that no two of the spark discharge inputs are exactly alike. A Fourier spectrum of the deconvoluted signatures is shown in Figure 48 and a shock spectrum ratio relative to Run No. 3.1002 is shown in Figure 49. The shock spectrum ratio results is a straight horizontal line for identical pulses and in Figure 49 one can see some horizontal sections in the curve. The frequency band from 0 to 250 kHz is representative of signatures from pulses from a similar AE source. The signatures above 250 kHz show large variation and will be ignored for the present.

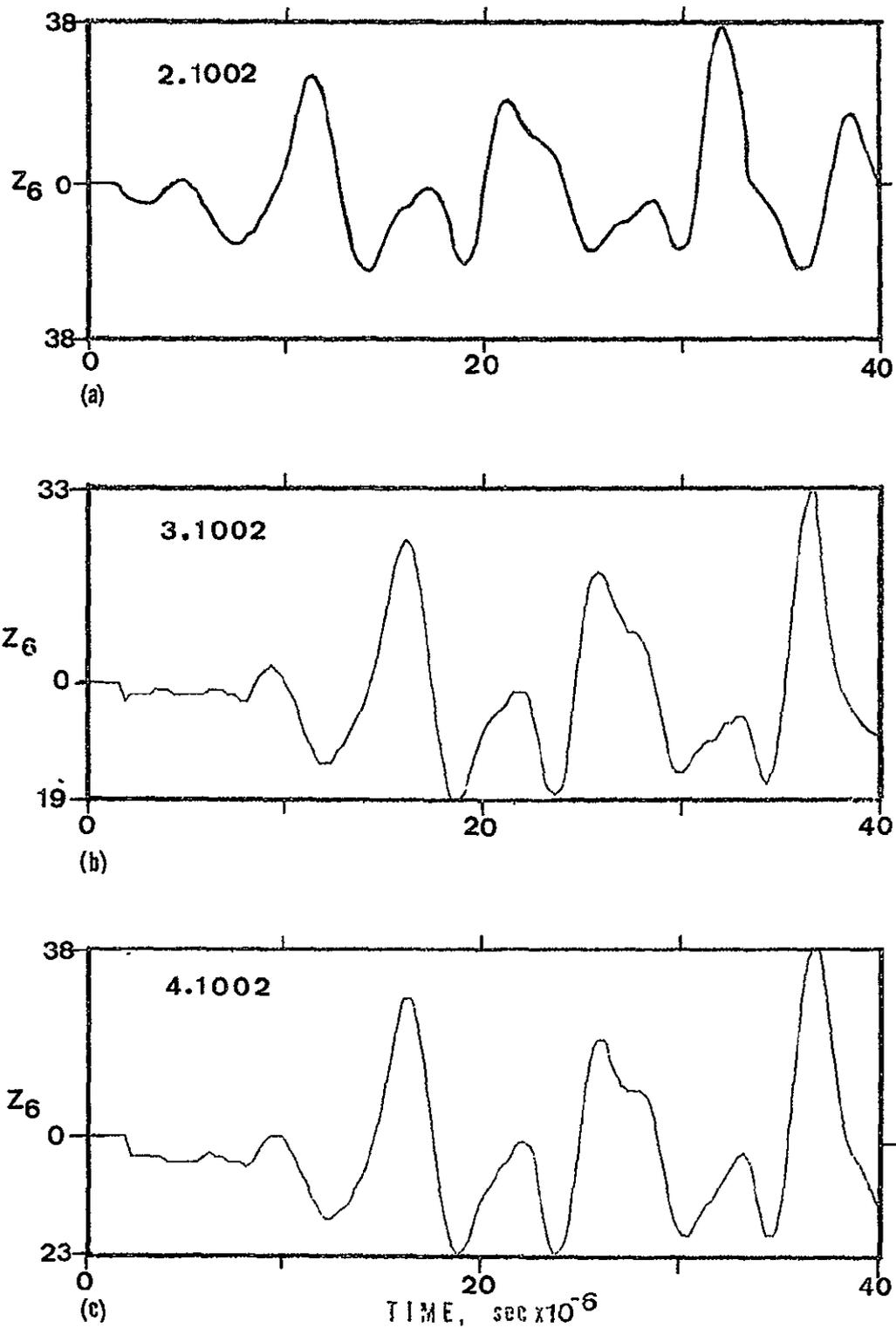Fig. 45. As-received time domain trace for three
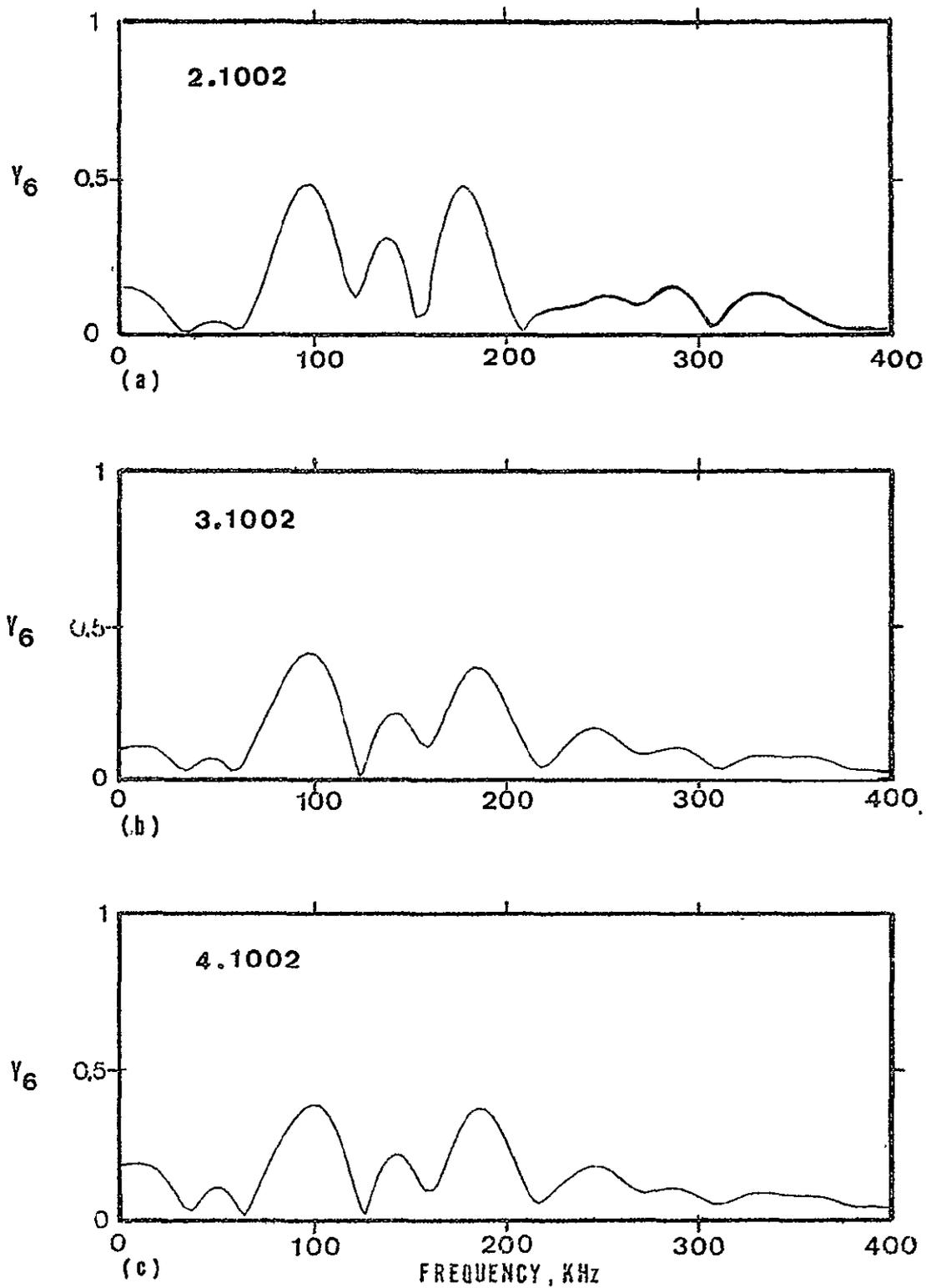spark discharges from the Dunegan/Endevco transducer.

Fig. 46   Frequency spectrum of pulses shown in
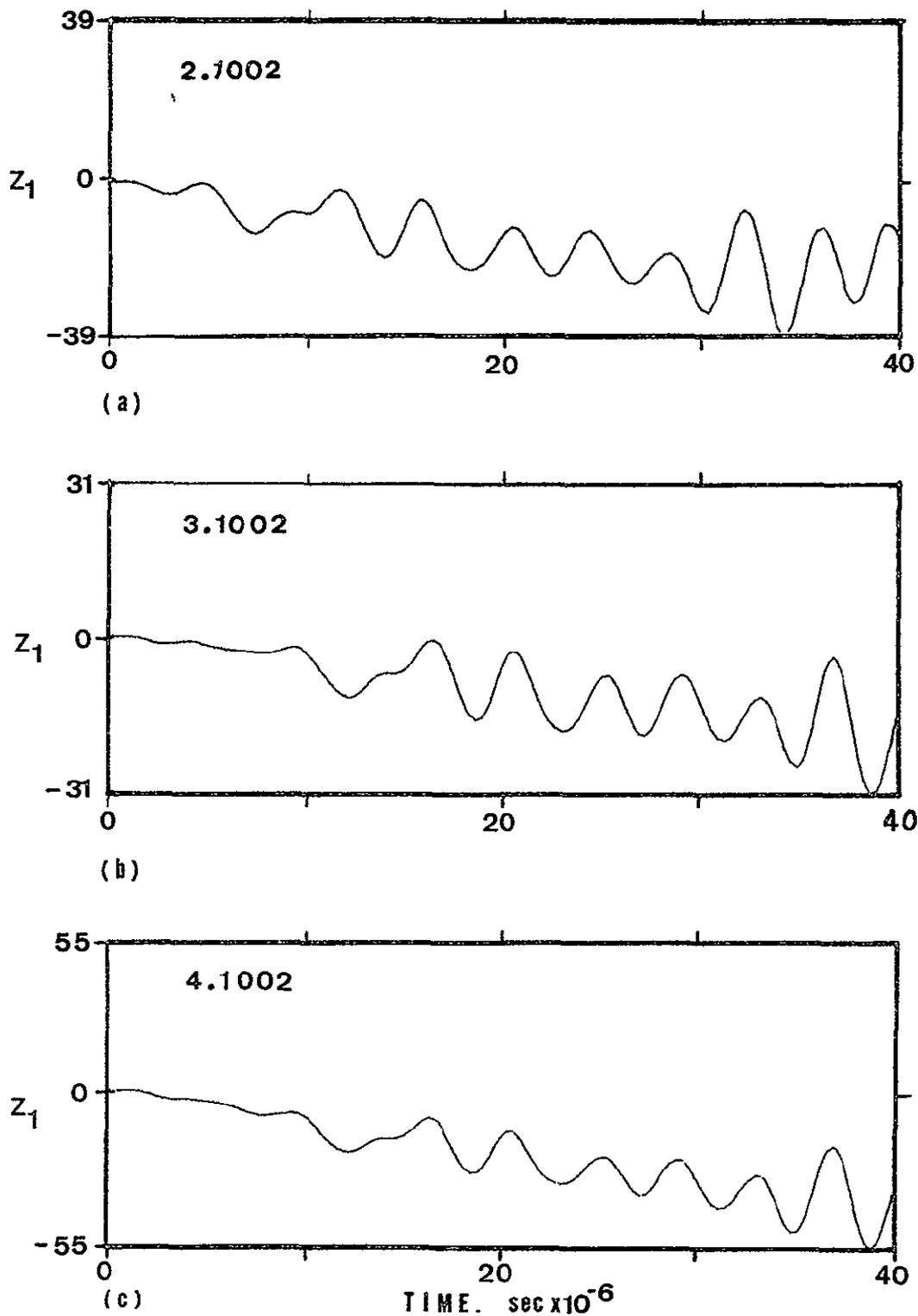Figure 45.

Fig. 47. Deconvolution through the flat plate model
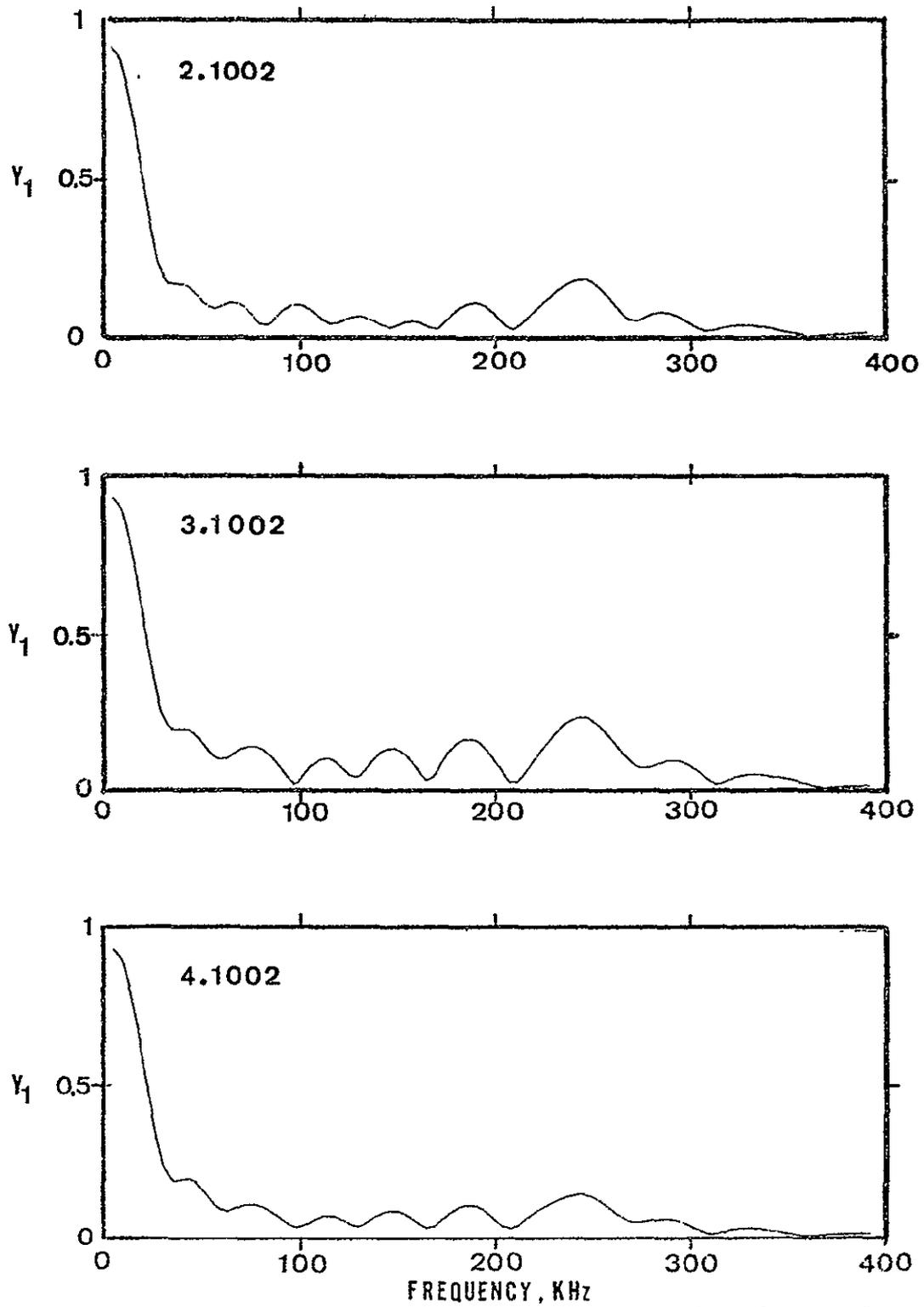of the results shown in Figure 45.

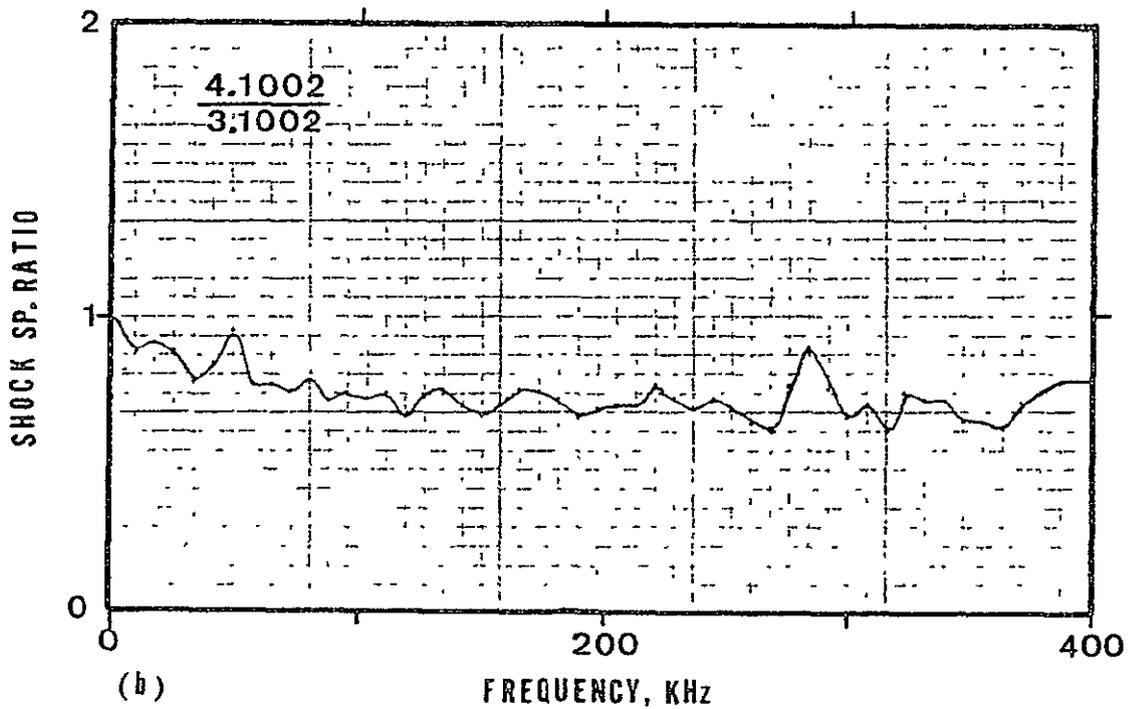Fig. 48. Frequency spectrum of the pulse deconvolutions shown in Figure 47.
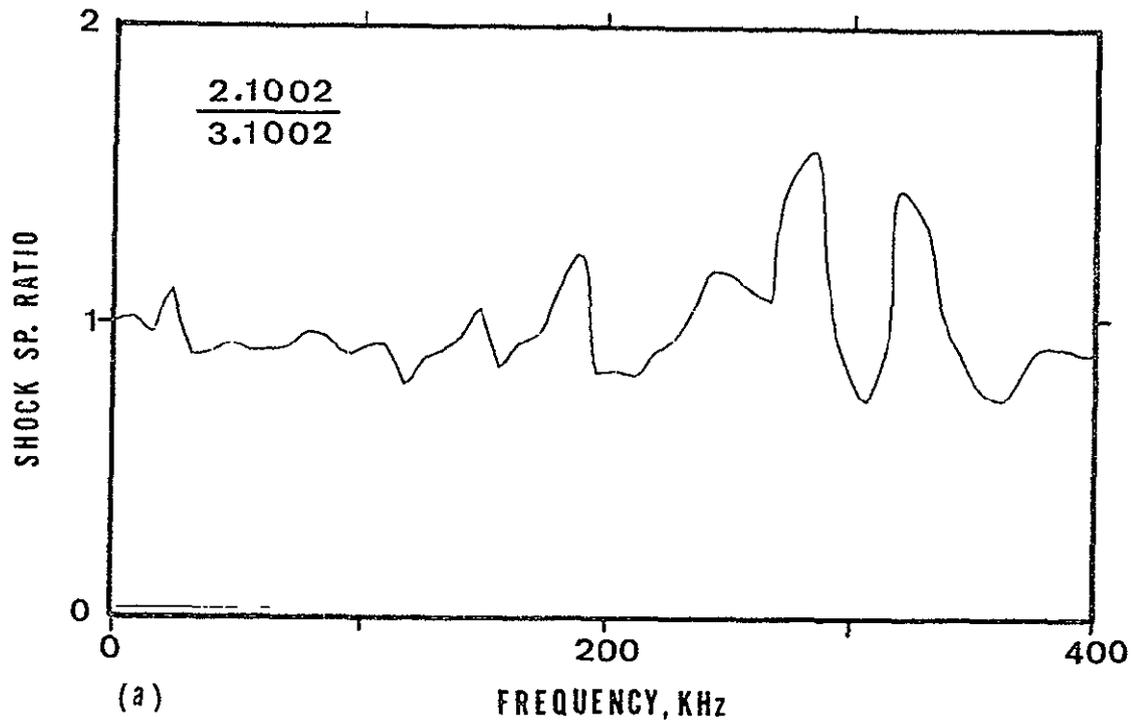
Fig. 49. Shock spectrum ratio of similar deconvolution pulses shown in Fig. 47.

In general, the spark discharge equipment was found to be very repeatable within the first 60 to 100 µs from the leading edge of the pulse recording. For the sake of close examination of the best information about the AE source, it was necessary to confine the signature to the first 40 µs of the pulse. It seems that after this time, large signals appear which dwarf the initial information of the pulse signature. These large signals may be higher energy packages traveling in a different mode of vibration, or they may be built-up reflections.

Deconvolution with Different Transducers Experiment

The objective of this experiment was to answer the question: "Will deconvolutions through transducers with different designs have a signature shape which indicates a common AE source?" Four transducers were selected and cemented to a compact tensile specimen used for fracture mechanics crack-growth studies. This specimen type was selected because it could be used for the experiment that followed this one as a generator of AE signals as a crack that is growing. A fatigue crack had already been grown in the specimen used, and the spark discharge probe was mounted at a location just above the crack tip. The transducers were mounted in a radius approximately 25 mm from

the crack tip as shown in the photograph in Figure 50. They are identified more specifically in Table 3.

Samples of the leading edge of pulses from a spark discharge AE source for three different transducer measuring systems are shown in Figure 51. The pulse recording from the PCB 392A transducer is not shown, because the transistor circuit mounted in the transducer's case behaved as if it were overloaded by the electromagnetic waves that were broadcast from the spark discharge probe. Thus it was disqualified from this experiment. The pulse outputs from the B & K Type 4339 accelerometer, the D/E D9202 acoustic emission pickup and the B & K Type 4344 accelerometer are shown in Figure 51, plots (a), (b) and (c) respectively. The natural frequencies of the transducers are the major waves that are seen in these recordings. The Fourier frequency spectrum of the three pulses are shown in Figure 52, and the major high points of the spectrum are noticed at the natural frequencies. Deconvolution of each of the pulses from the three transducers through the model for the specimen is shown in Figure 53. Figures 53(b) and (c) of the transducer deconvolution signatures could be attributed to a similar AE source. Figure 53(a) looks different and this is attributed to the low natural frequency of the transducer. This conclusion could not have been made on the basis of Figure 51 aone. The frequency spectrum of the deconvolution signatures in Figure 53 is shown in Figure 54. Judging from the deconvolution
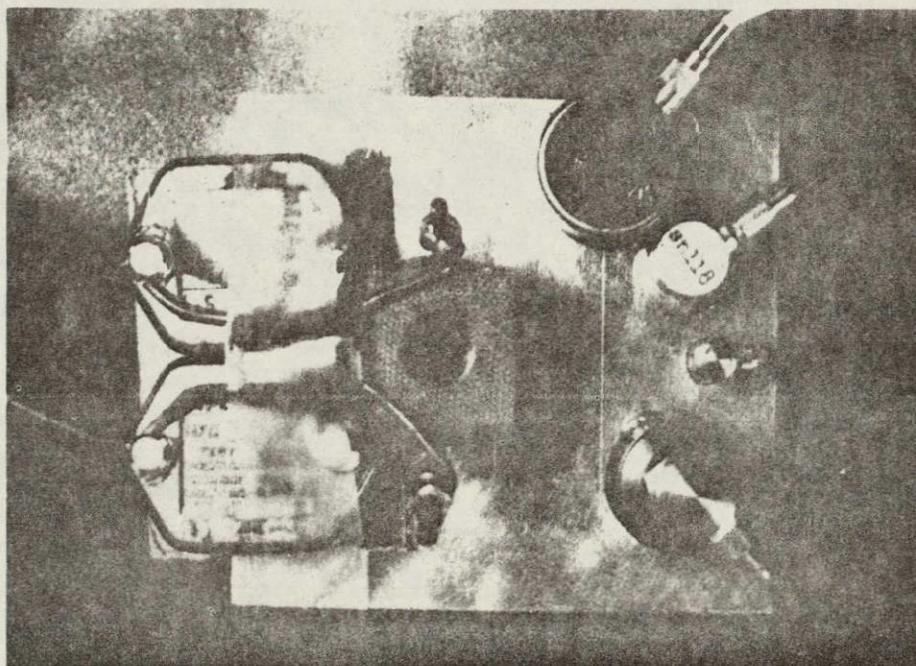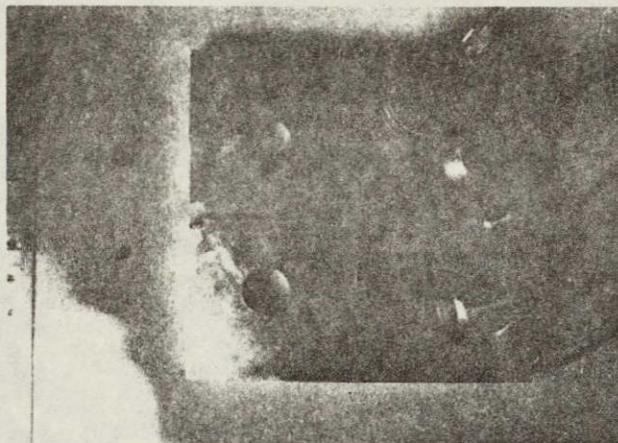
Fig. 50. Relative locations of the transducers on a
single edge cracked compact tensile fracture specimen and
the spark probe.
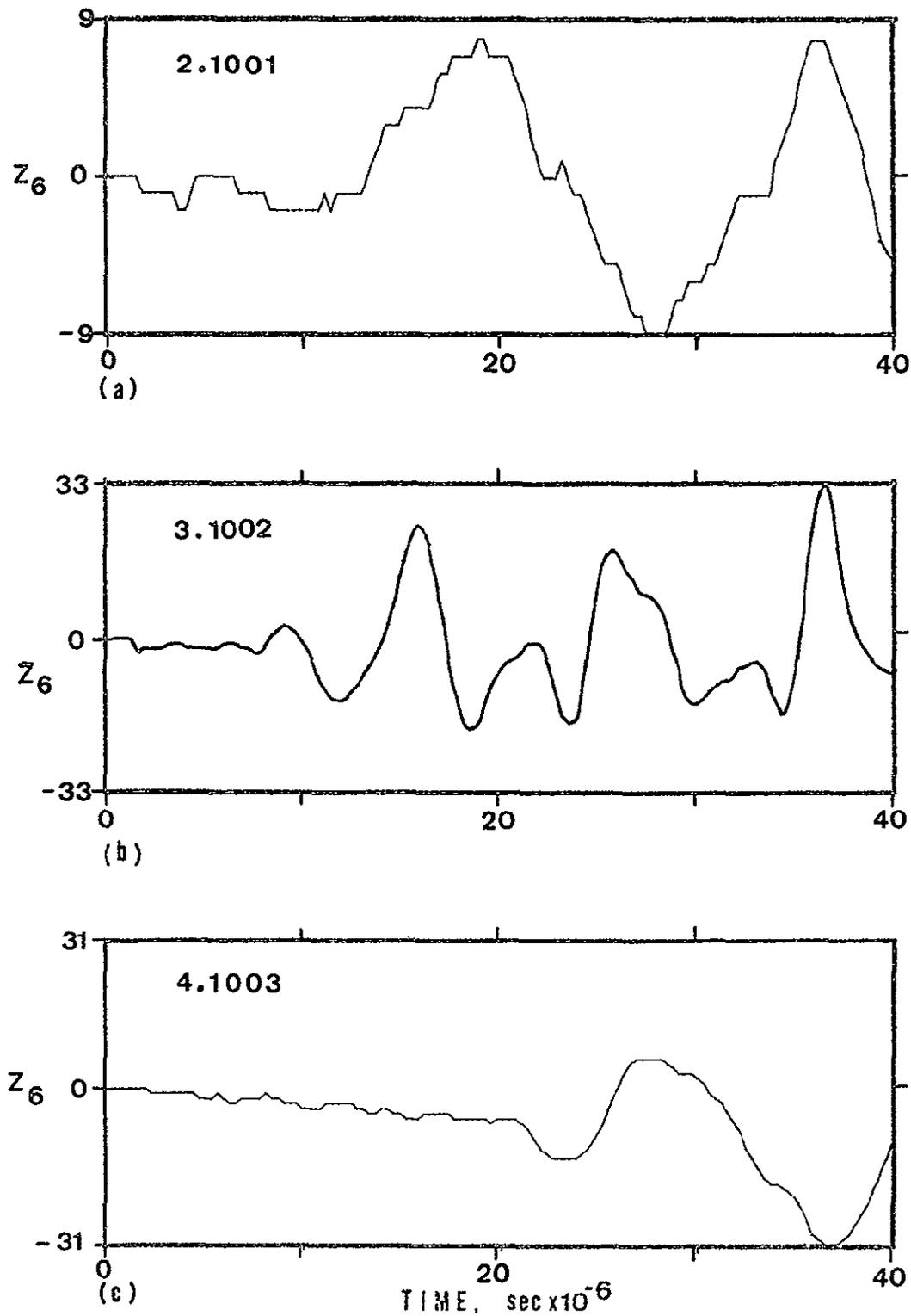
Fig. 51. As-received time domain trace for spark discharges received by three different transducers.

Fig. 52. Frequency spectrum of pulses shown in Figure 51.

Fig. 53. Deconvolution through the flat plate model for the pulse shown in Figure 51.
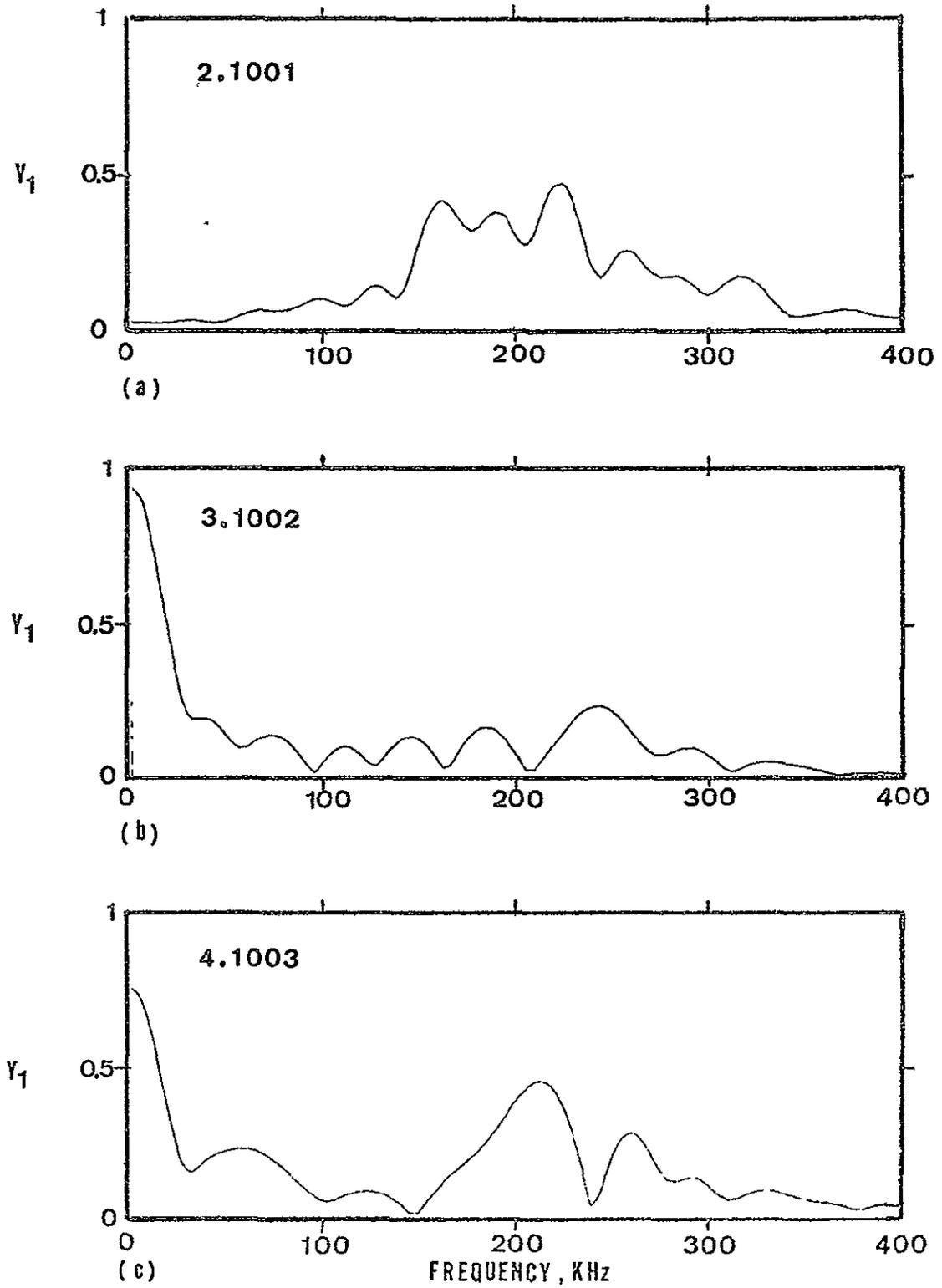
Fig. 54. Frequency spectrum of the pulse deconvolutions shown in Figure 53.

plots presented in Figure 53(b) and (c), the method of analy-

sis can give approximately equivalent shapes in the time do-

main, and the AE transducer appears to give good results.

Thus, for the remaining experiments discussed in this chapter,

the AE (D/E) transducer was selected for recording the pulses

and for computation of a deconvolution signature.

Discrimination between AE Sources
Experiment

The objective of this experiment was to determine how

sensitive an AE transducer and the deconvolution signature

method are in detecting differences between pulses from

different AE generators. The three sources of acoustic

emissions were: 1) the electrical discharge probe; 2) a

steel ball impacting the specimen surface; 3) a crack grow-

ing within the specimen. The steel ball impacting on the

specimen was accomplished by rolling a 1.01 gm ball down a

slight incline; at the end of the channel the ball fell

10 mm, struck the specimen near the tip of the fatigue crack

and then bounced off the edge of the specimen. A smaller

ball (see Figure 50(a)) was also dropped on the specimen,

but the signals from the transducers were small, so that

this data was not prepared for examination. Acoustic emis-

sions from a growing crack were obtained by pulling the spec-

imen apart in an Instron screw-driven tensile testing mach-

ine. The rate of deformation in the testing machine was

0.013 mm/minute.

Sample plots of the as-received data from (a) a spark discharge, (b) a ball impacting the plate and (c) a growing crack are shown in Figure 55; the frequency spectrum of the respective pulse is shown in Figure 56. The deconvolution of the AE data and their frequency spectrum are shown in Figures 57 and 58 respectively.

Figure 57 clearly demonstrates that there are three different pulse trains for three different AE sources. Figure 57(c) is similar to 57(a) which is not unexpected, since a crack growing is a pulse of short duration similar to the sound wave from the electric spark discharge. Yet there are enough differences that one can say that the AE generator for (a) is not the same as for (c). The frequency spectra shown in Figure 58 are helpful in that they point out the difference between the three different AE sources.

Discrimination between Sound and Defective Ball Bearings

A test rig design was selected for this experiment that would load thrust ball bearings and would have a minimum number of moving parts. The configuration of the completed rig is shown in the photographs in Figure 34(a) and (b). An axial force on the bearings is controlled with the hydraulic cylinder seen on the right side of the loading frame in Figure 34(a). Of the two bearings that are operating during a test, the smaller bearing is the one expected to fail, and it is located on the right side of the rotating

Fig. 55. As-received time domain traces from the following acoustic emission sources: a) spark discharge, b) ball impacting and c) a growing crack in a tear test.
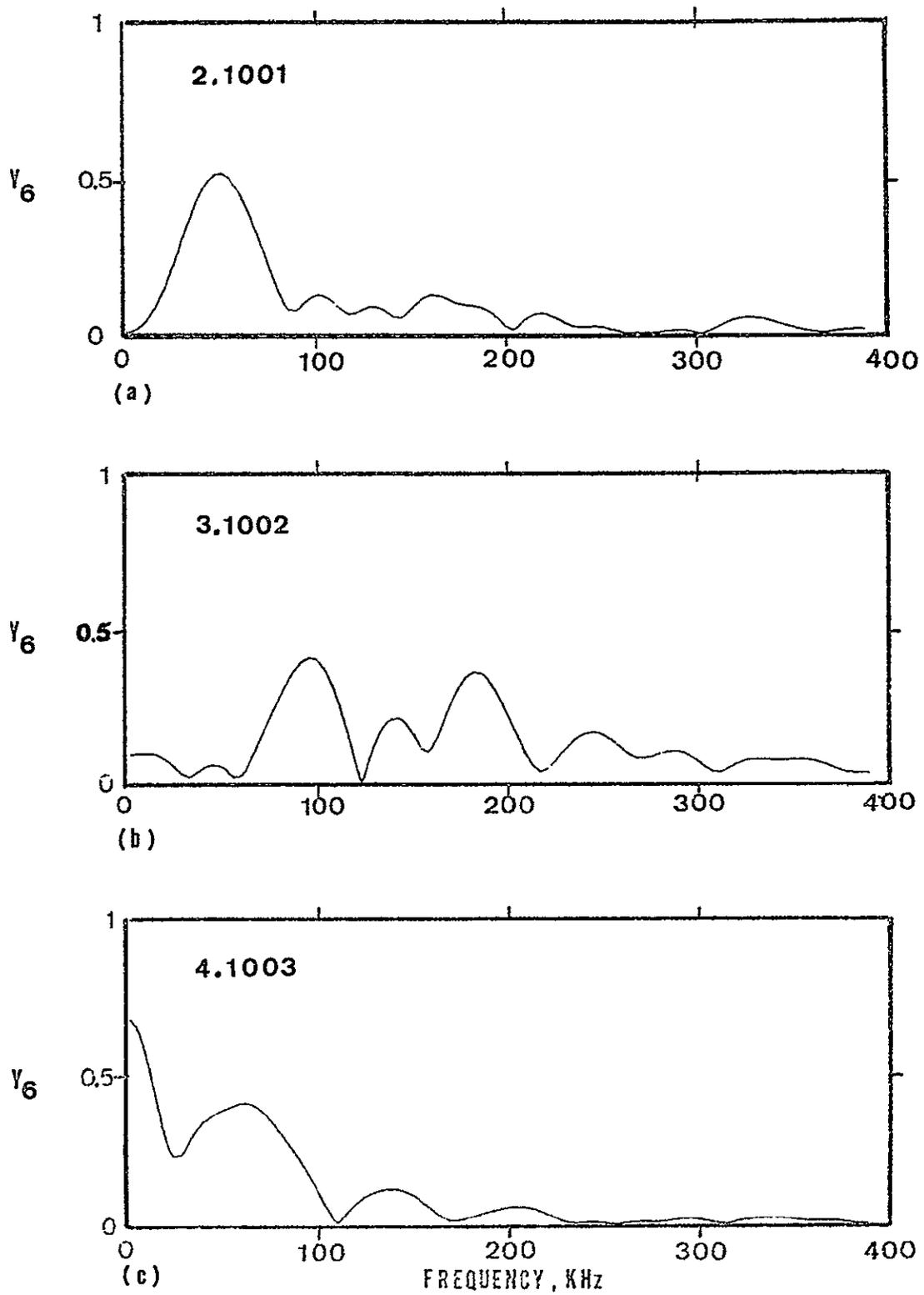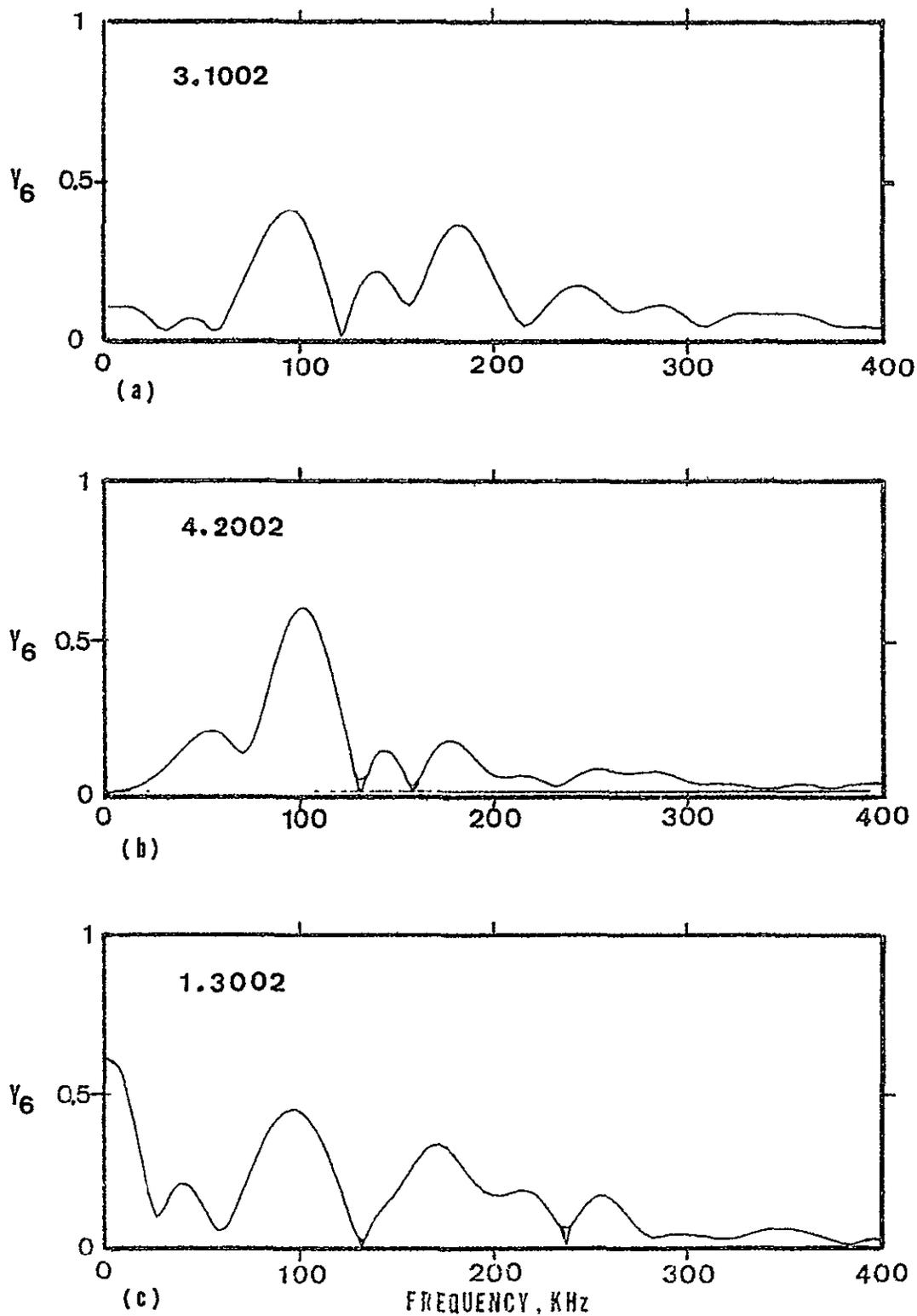
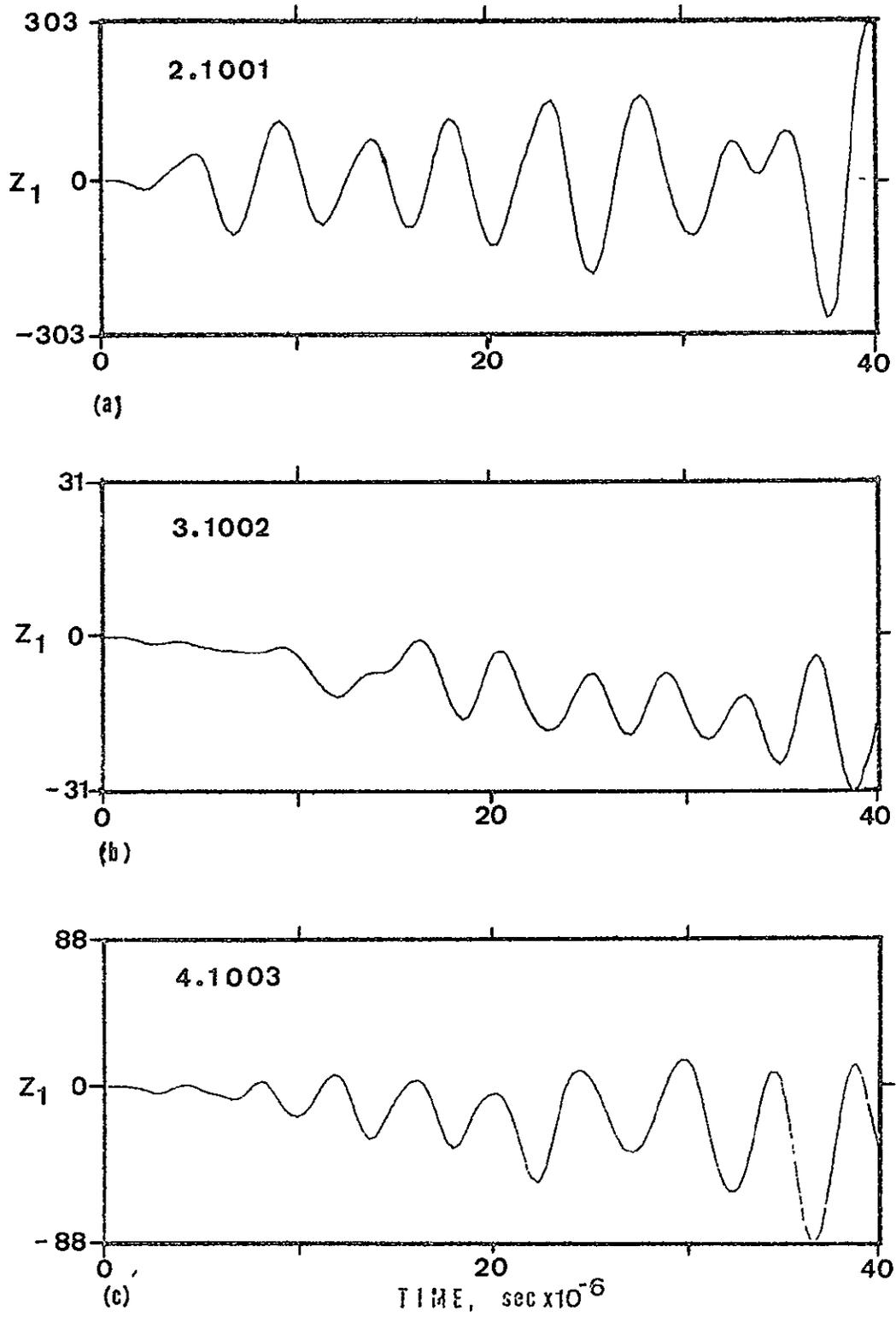Fig. 56. Frequency spectrum of pulses shown in Figure 55.

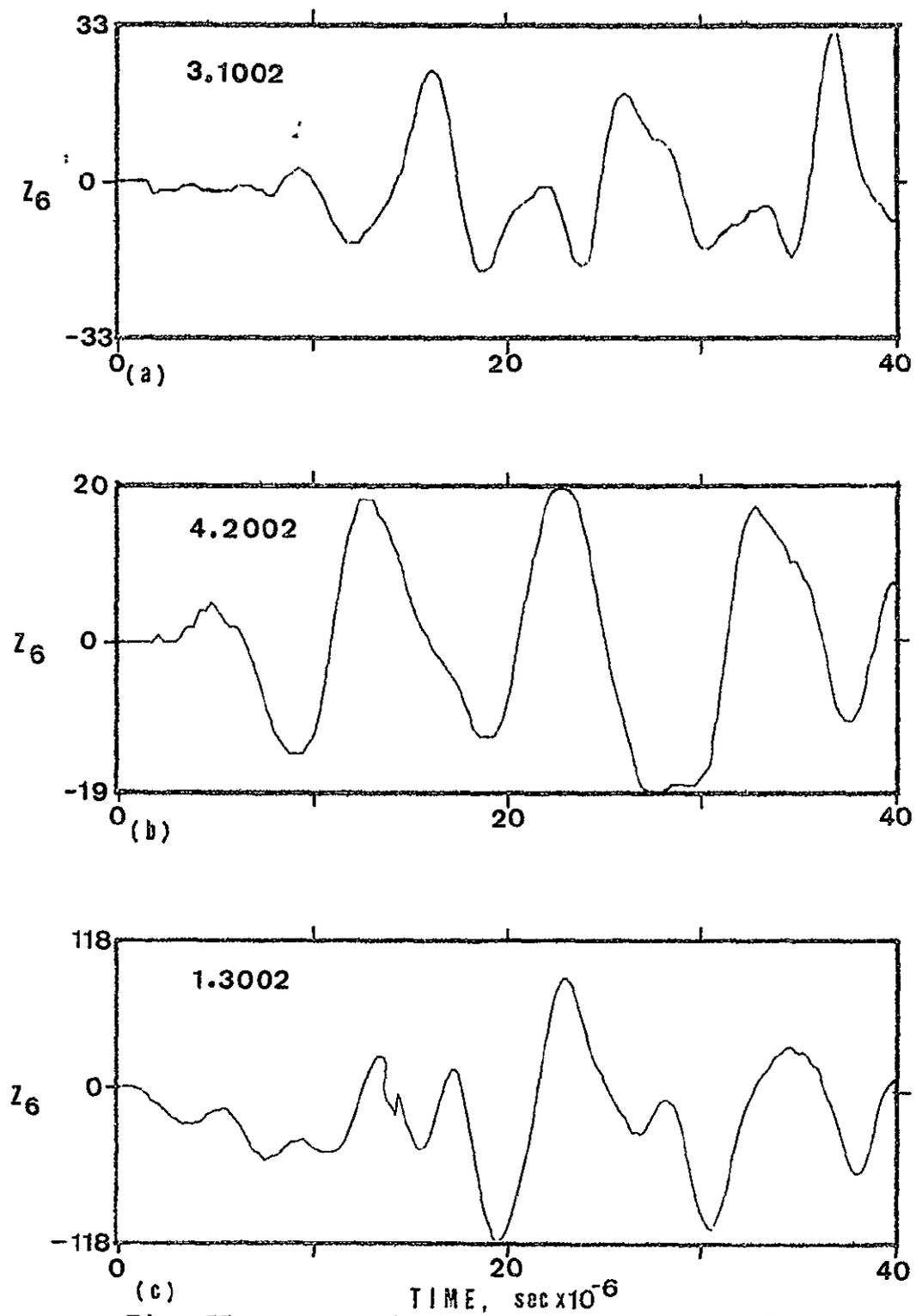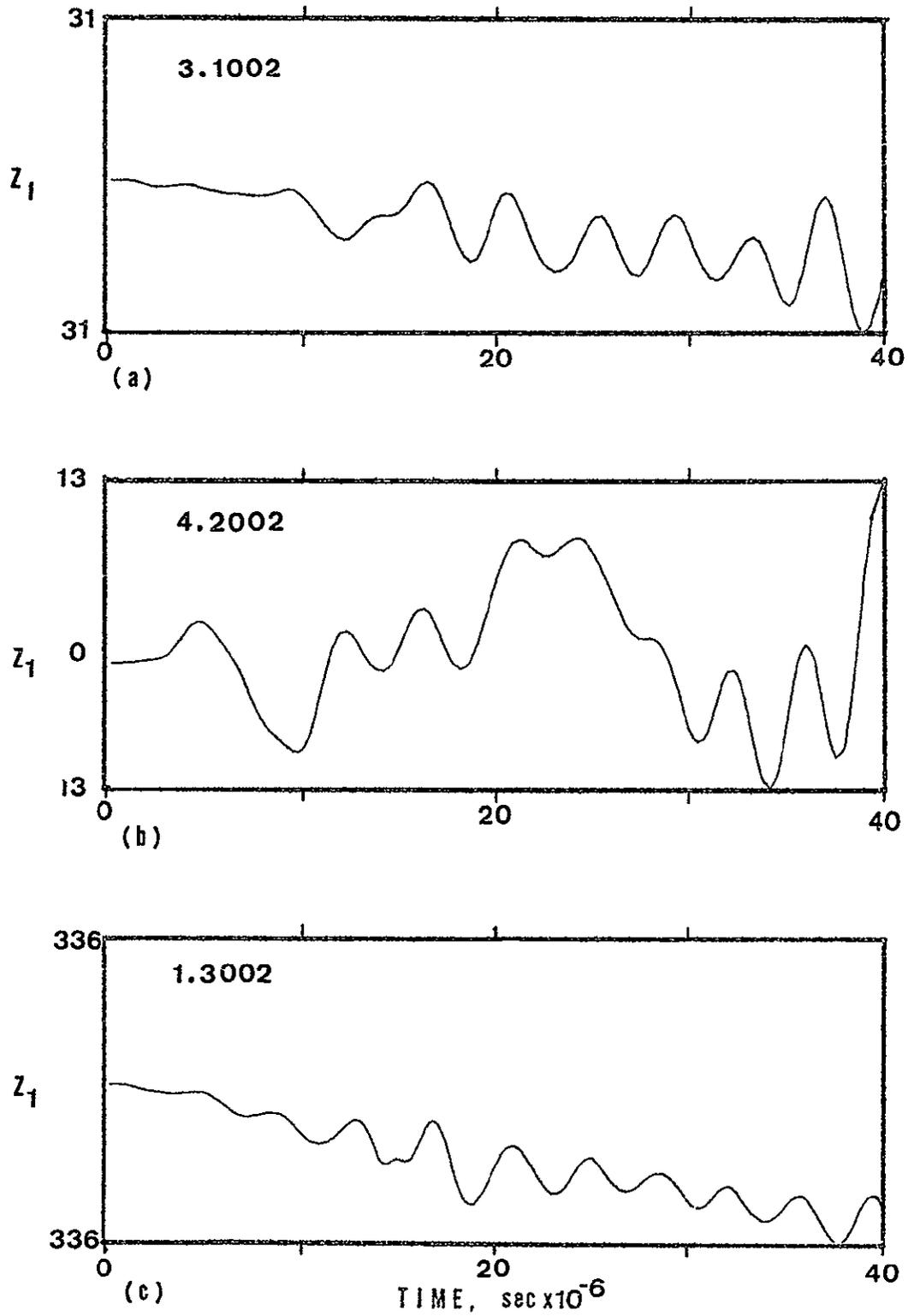Fig. 57. Deconvolution through the flat plate model of the results shown in Figure 55.
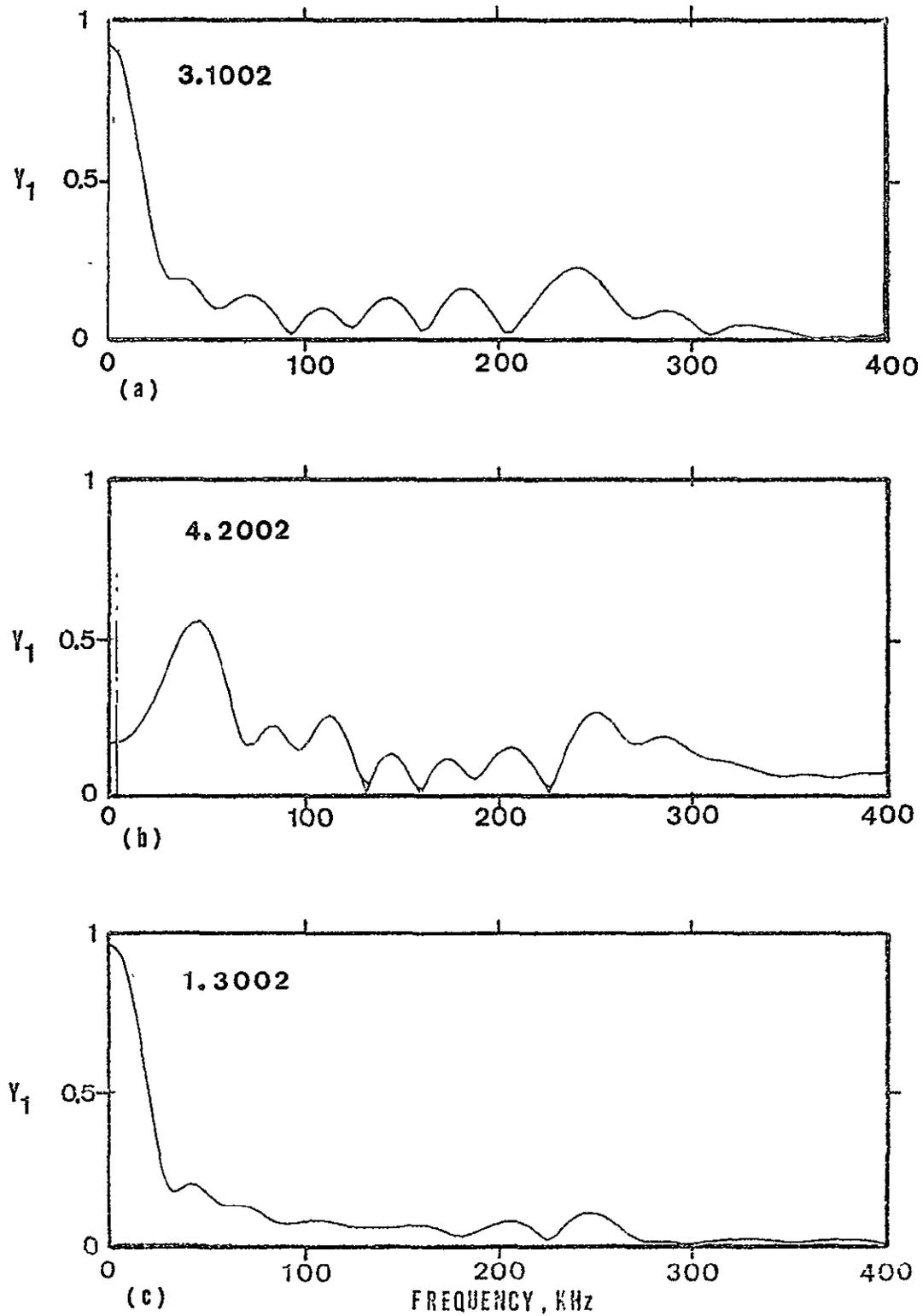
Fig. 58. Frequency spectrum of the pulse deconvolutions shown in Figure 57.

cylindrical block. The larger bearing on the left side is a backing bearing to balance the thrust forces and allow the middle block to rotate freely. The torque to rotate the middle block comes through a 12.5 mm shaft on the central axis of the system. The motor is on the right side of the assembly. Two motors were used to run the ball bearings. A 1/3 horsepower 1875 rpm motor was used for fatigue damaging bearings. A variable speed motor was used for recording AE data in order to spread out the time between AE bursts by running at low speeds.

The test bearings were Nice Type 1009. These bearings have twelve 1/4 in diameter balls and the ball race diameter is 1½ inches, ID is 1 inch, and OD is 1.95 inches.

For the experiments reported here one test bearing was artificially damaged by cutting a slot at right angles to the direction of ball travel in the race. Another bearing was artificially damaged by cutting a slot in one of the balls. Each slot was made with an electric discharge machine and was 0.15 mm wide. The backing or support bearing was a Dixie Bearing, Inc., GT 18. This bearing has eighteen 1/4 inch diameter balls and the ball race diameter is 2.1 inches, ID is 1 and 5/8 inches and OD is 2 and 5/8 inches. The design load for the small diameter thrust bearing is 2475 lbs and the design load for the larger diameter bearing is 3243 lbs.

The model for the ball bearing support structure which transmits the AE signal from the bearing to the Dunegan/ Endevco transducer was derived following the procedure described earlier for the compact tensile specimen. The model equation and the frequency response are shown in Figure 59.

The results of the bearing test experiments are shown in Figures 60 through 72. The figures for individual signal recordings are presented in three formats as follows. Figure (a) is the digitized signal from the tape recording, $Z_6(t)$. Figure (b) is the deconvoluted output for the signal shown in (a), $Z_1(t)$. Figure (c) is the Fourier spectrum of the deconvolution signal, $Y_1(f)$. The background noise for the electronic equipment recorded with the bearing stationary is shown in Figure 60.

The scale on the ordinate axis of (a) is digital steps and the scale on (b) is proportional to the calibration factors of the different components in the measurement system. The units for the Z_1 axis may be assumed to be 0.1 M/s^2 times the number shown. The frequency spectrum of the background noise appears to be random and high frequency as is expected for electronic noise. There is a large component above 400 kHz. This large component seems to be a consistent feature of the deconvolution model in all of the bearing experimental results, and it may be attributable to the digitizer
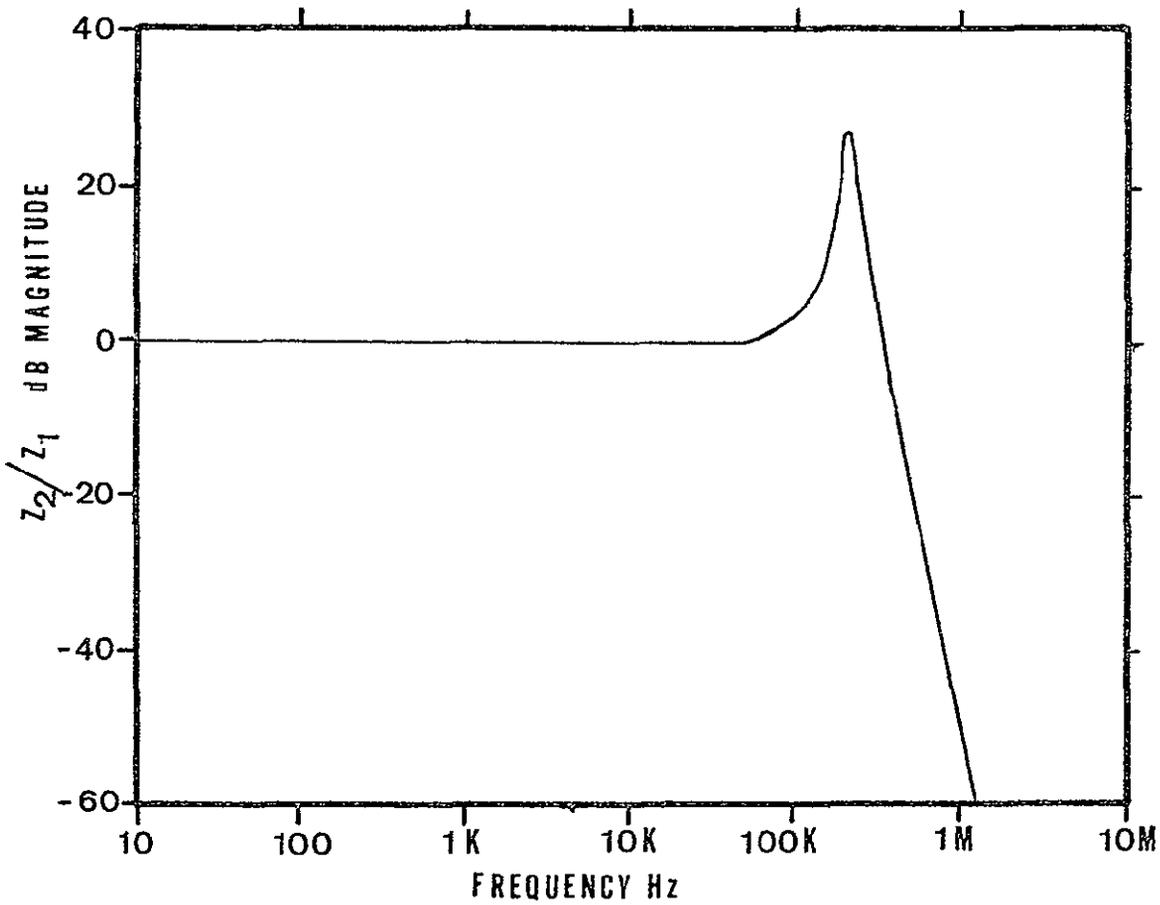
COMPONENT: Ball Bearing Mount

MODEL EQUATION:

$$\frac{Z_2}{Z_1} = \frac{\omega_M^2 \, \omega_M^2}{(D^2 + 2\zeta_{M1}\omega_{M1}D + \omega_{M1}^2)(D^2 + 2\zeta_{M2}\omega_{M2}D + \omega_{M2}^2)}$$

where

$$\omega_{M1} = 226{,}000 \times 2\pi$$

$$\omega_{M2} = 290{,}000 \times 2\pi$$

$$\zeta_{M1} = 0.01$$

$$\zeta_{M2} = 0.01$$

Figure 59   Bearing mount model and characteristic curve derived from the Fourier frequency spectrum curves.
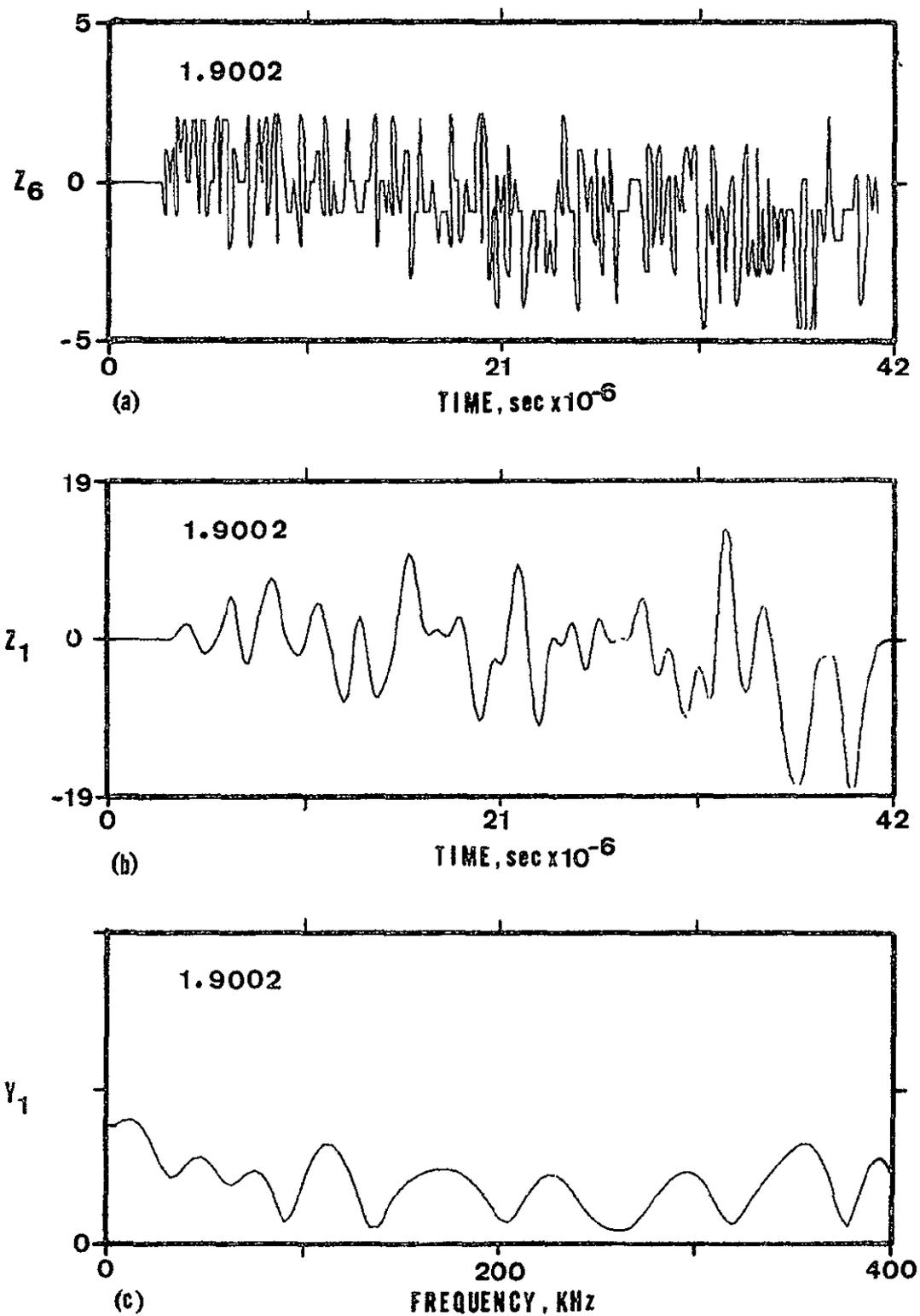
Fig. 60. Background signal with the bearing stationary.
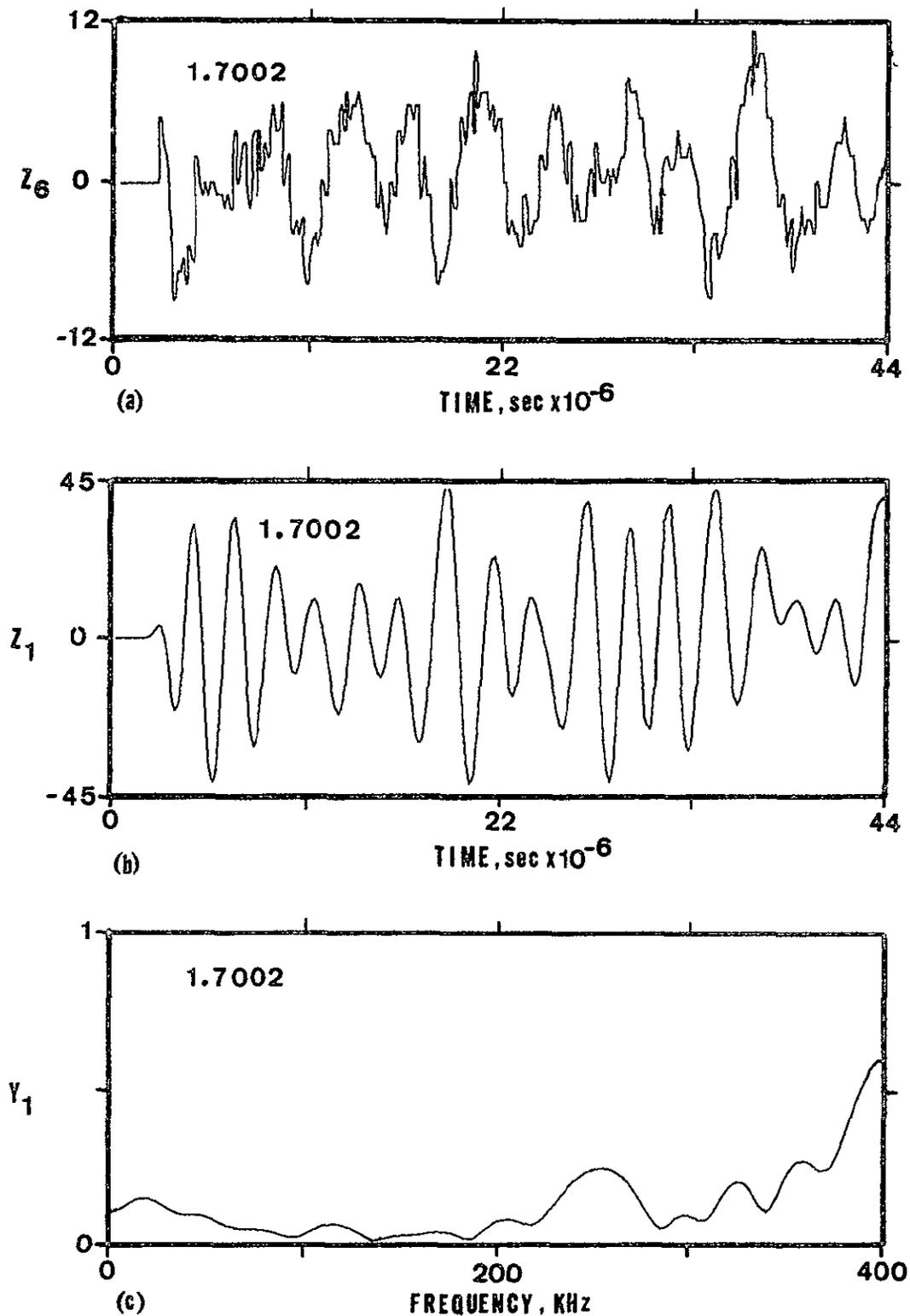
Fig. 61. Acoustic emission from a clean well lubri-
cated bearing running with a 700 lb load.
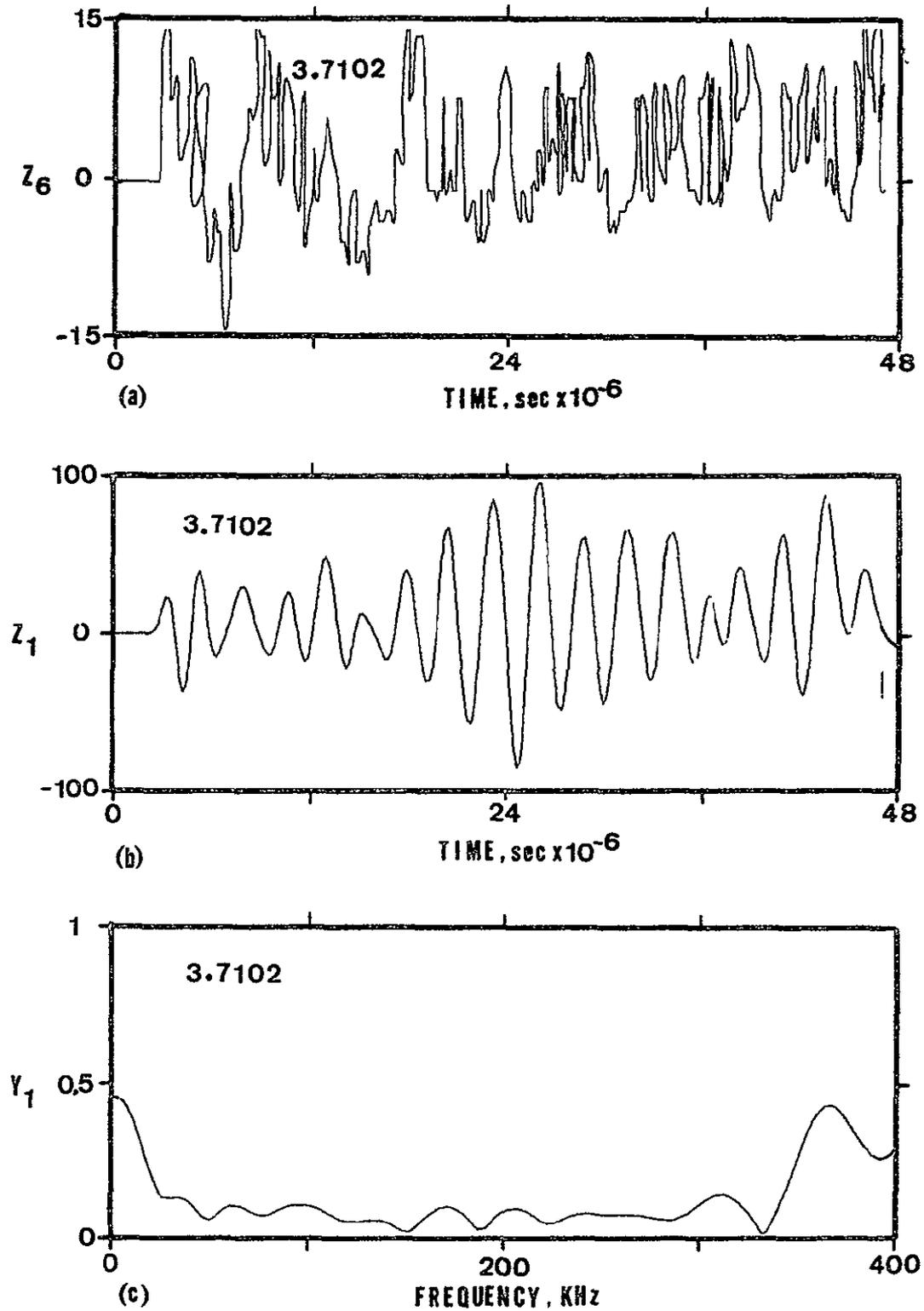
Fig. 62. Acoustic emission from a clean well lubricated bearing with a load of 700 lb.
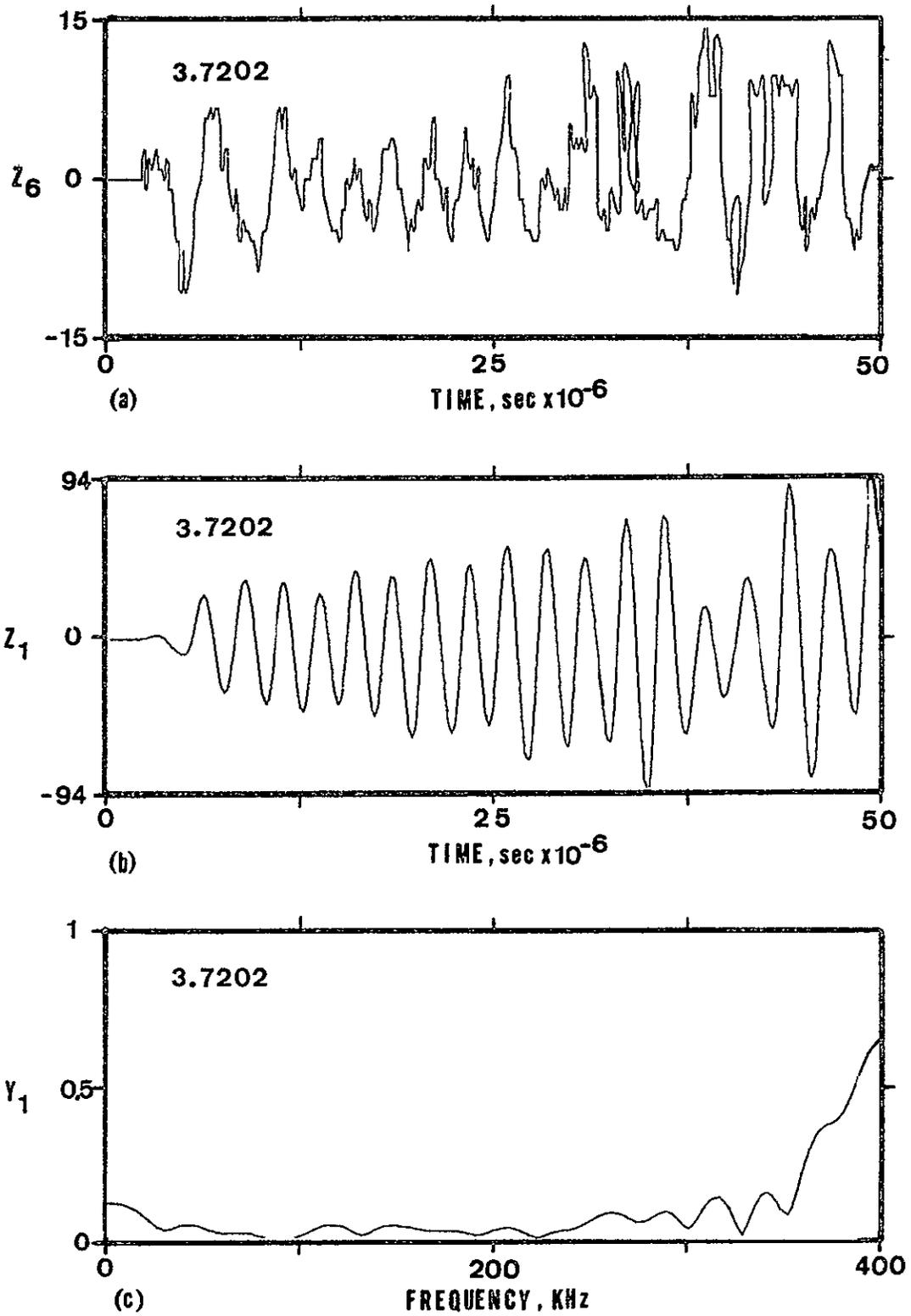
Fig. 63. Acoustic emission from a clean well lubri-
cated bearing with a 700 lb thrust.
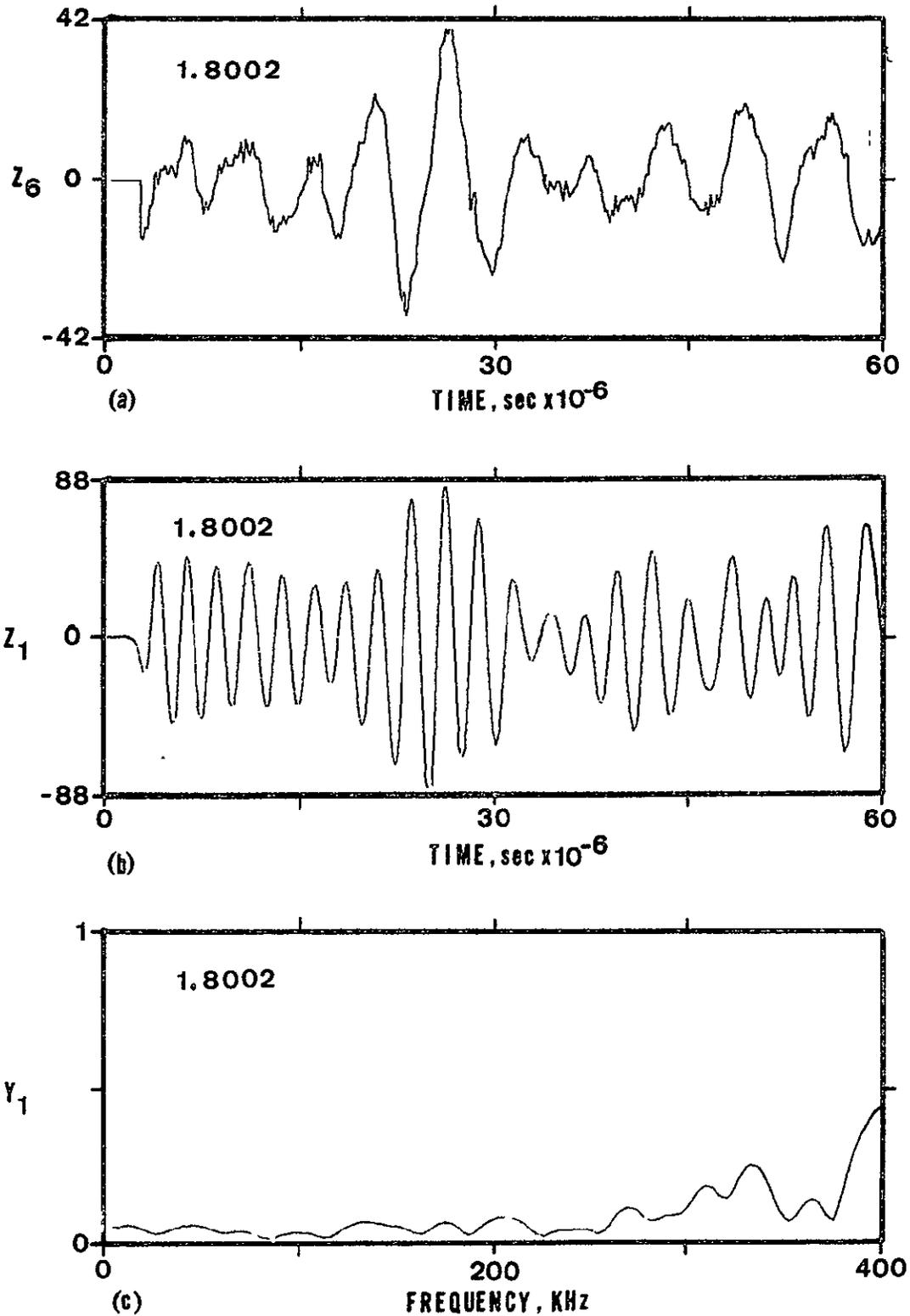
Fig. 64. Acoustic emission from a bearing with a cut in the race; 700 lb thrust.
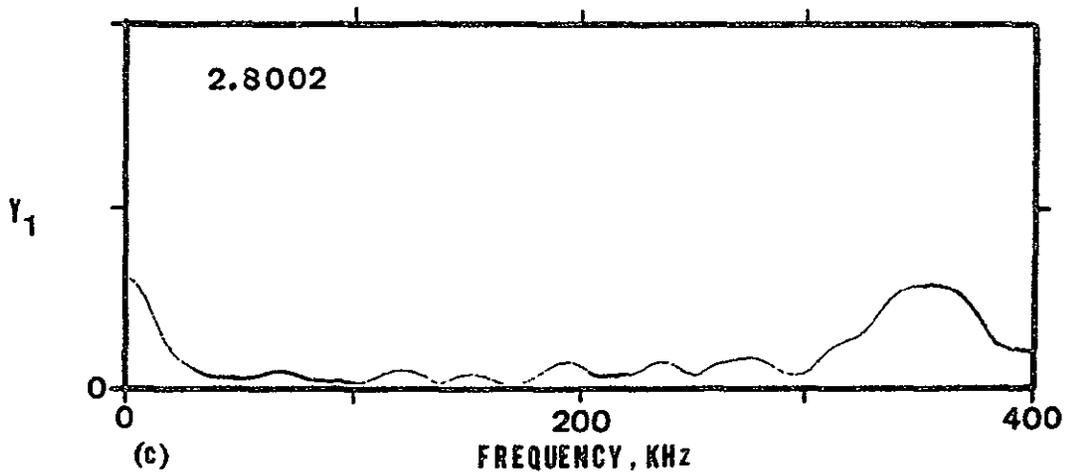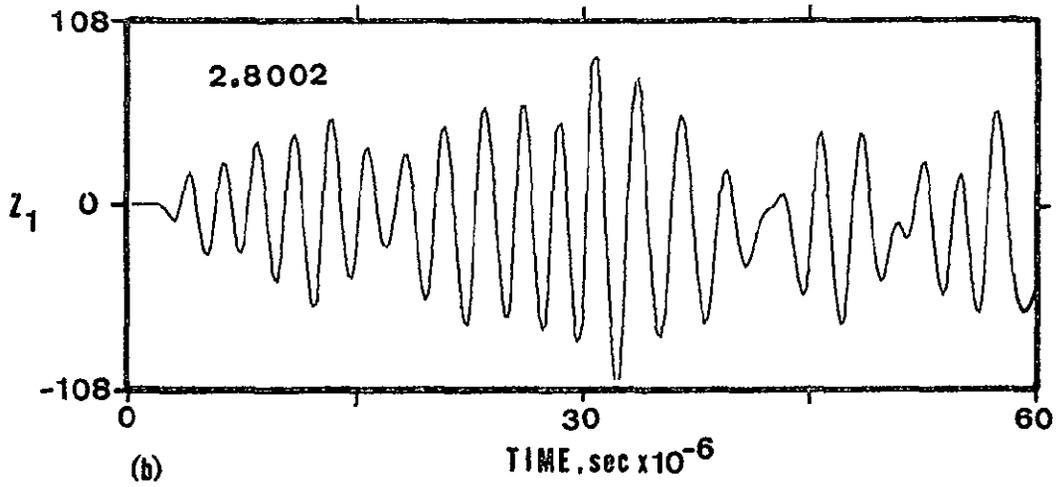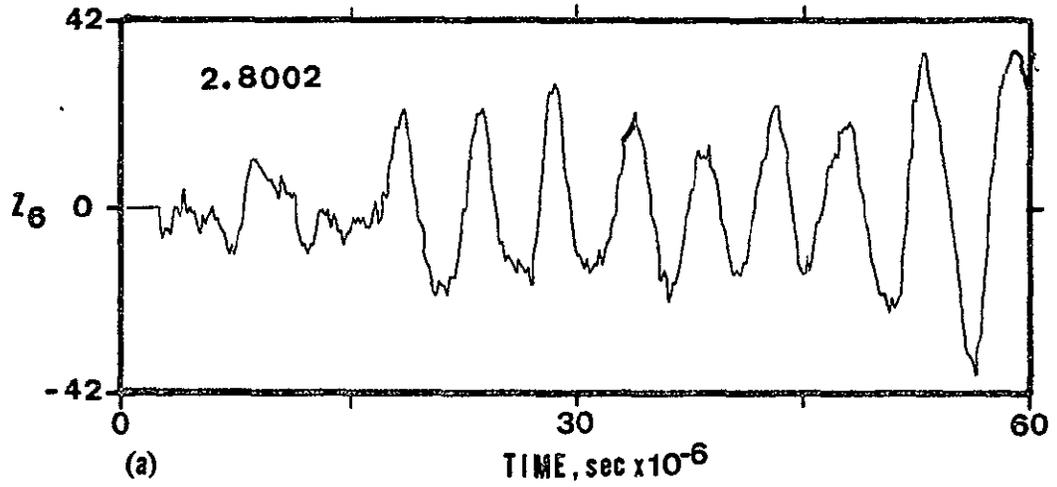
Fig. 65. Acoustic emission from a bearing with a cut in the race; 700 lb thrust.
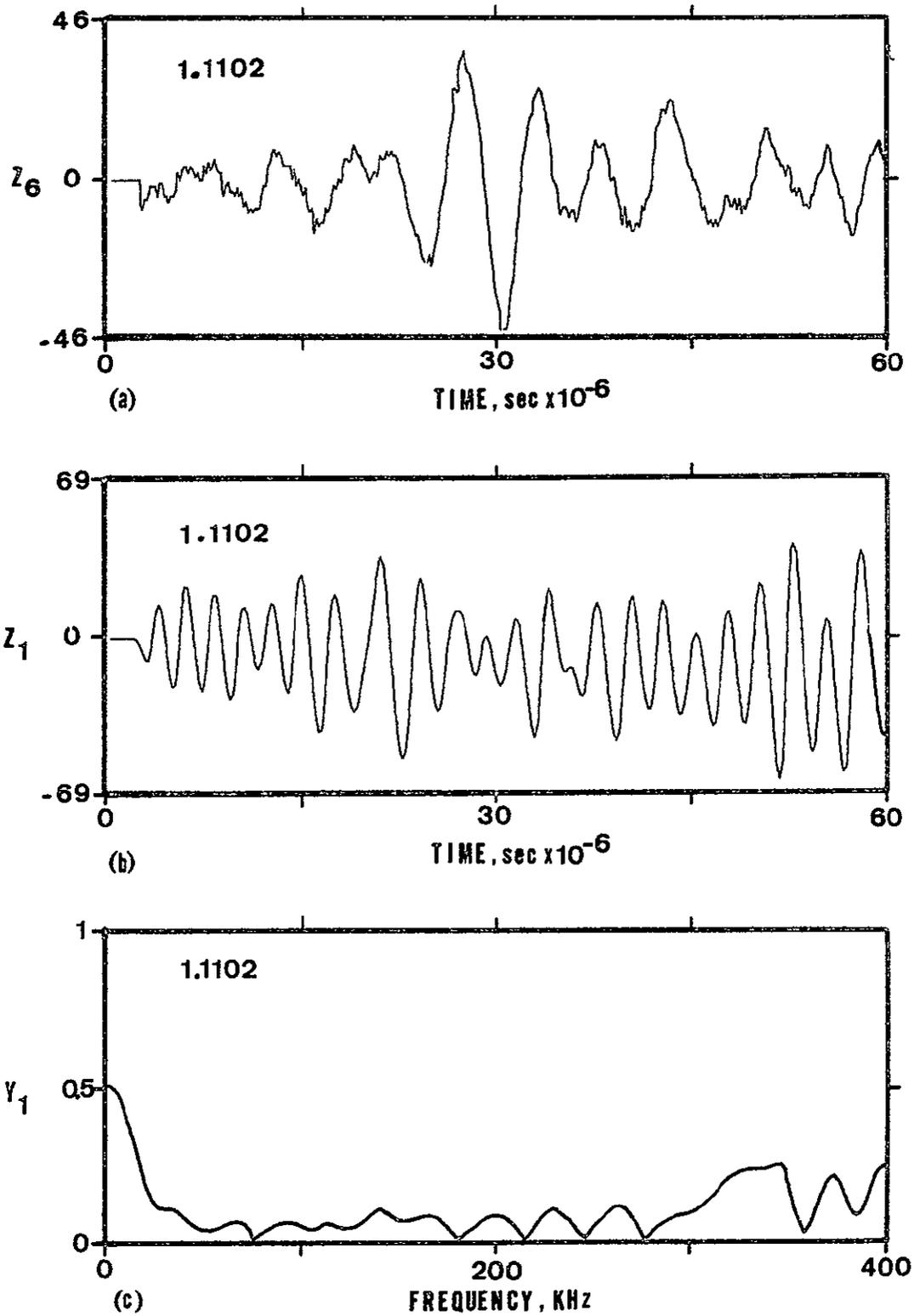
Fig. 66. Acoustic emission from a bearing with a cut in one ball; 700 lb thrust.
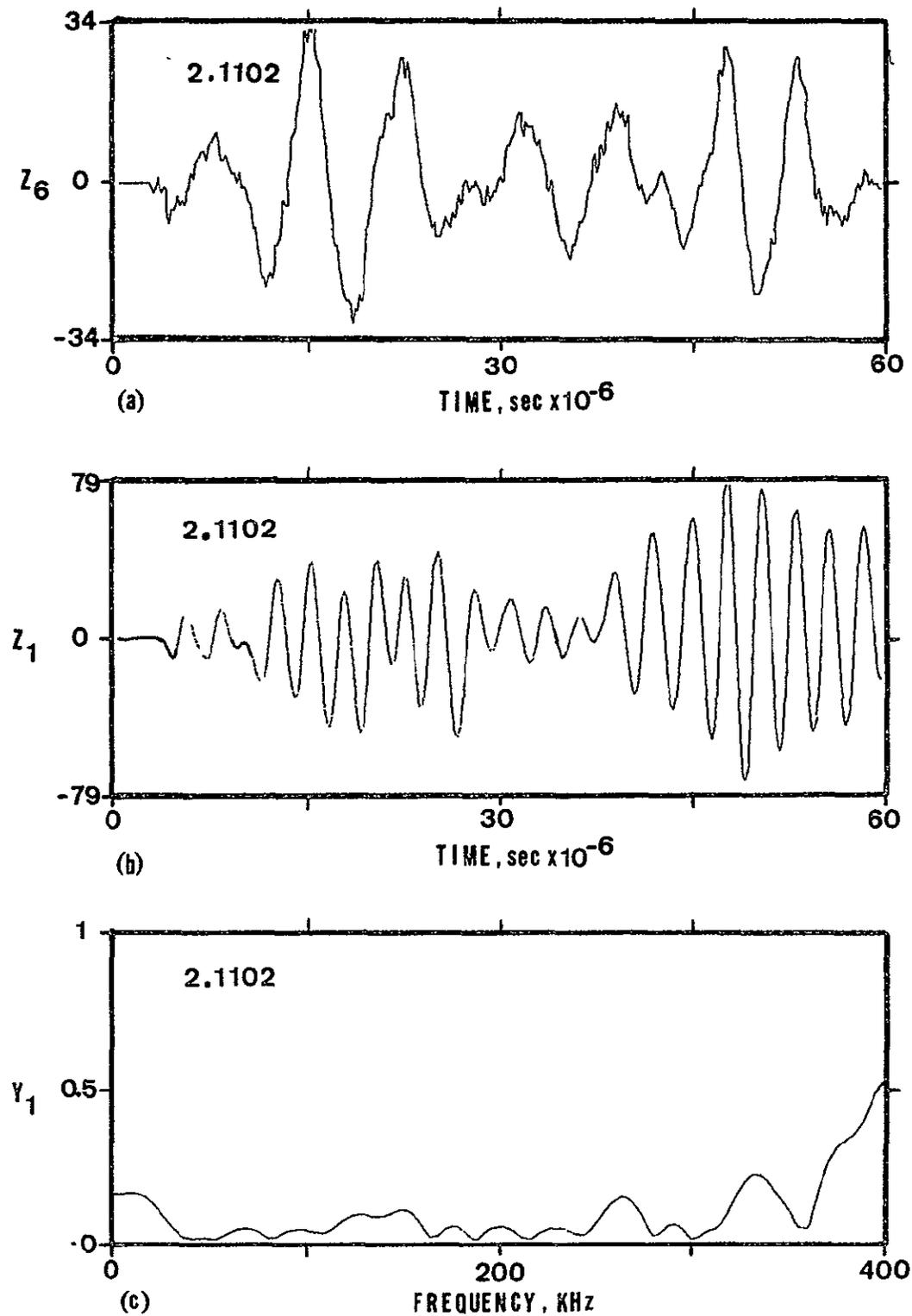
Fig. 67. Acoustic emission from a bearing with a cut in one ball; 700 lb thrust.
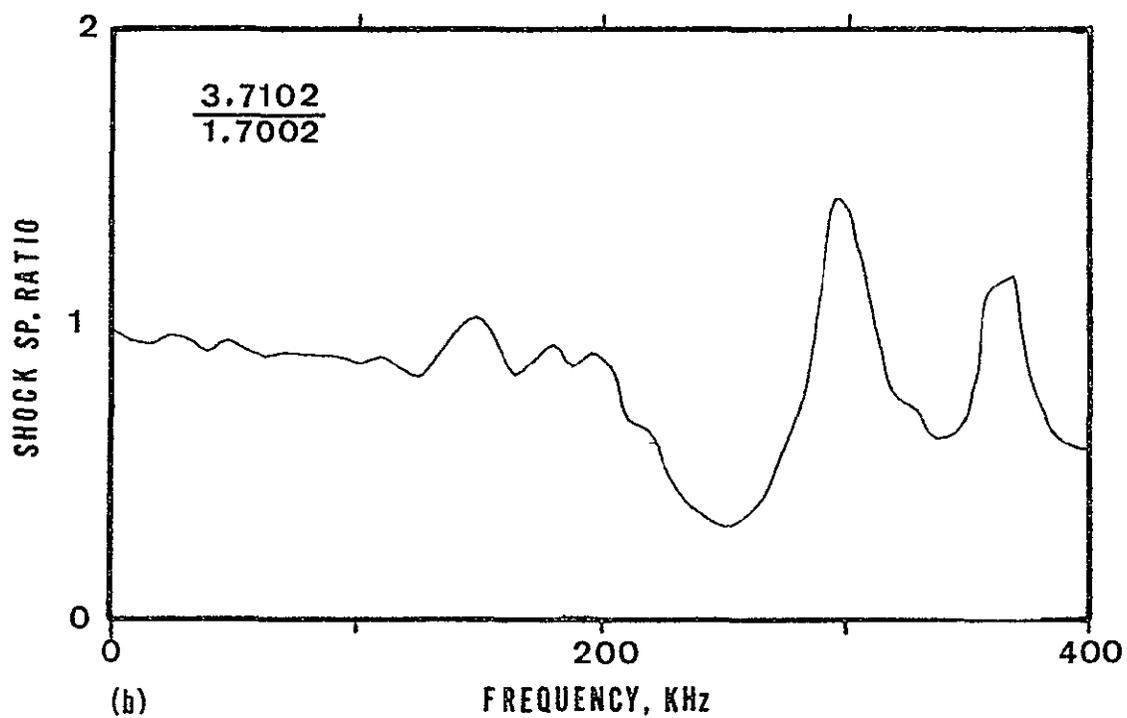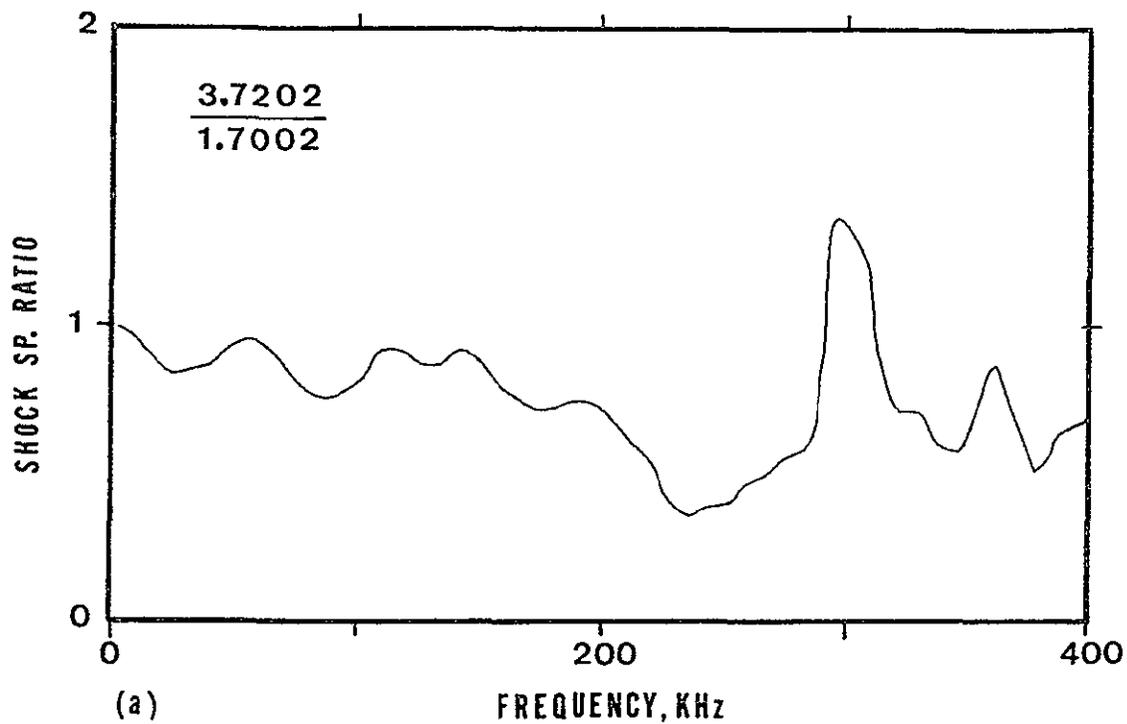
Fig. 68. Shock spectrum ratio of deconvoluted traces of a clean bearing relative to the acoustic emission shown in Figure 61(b).
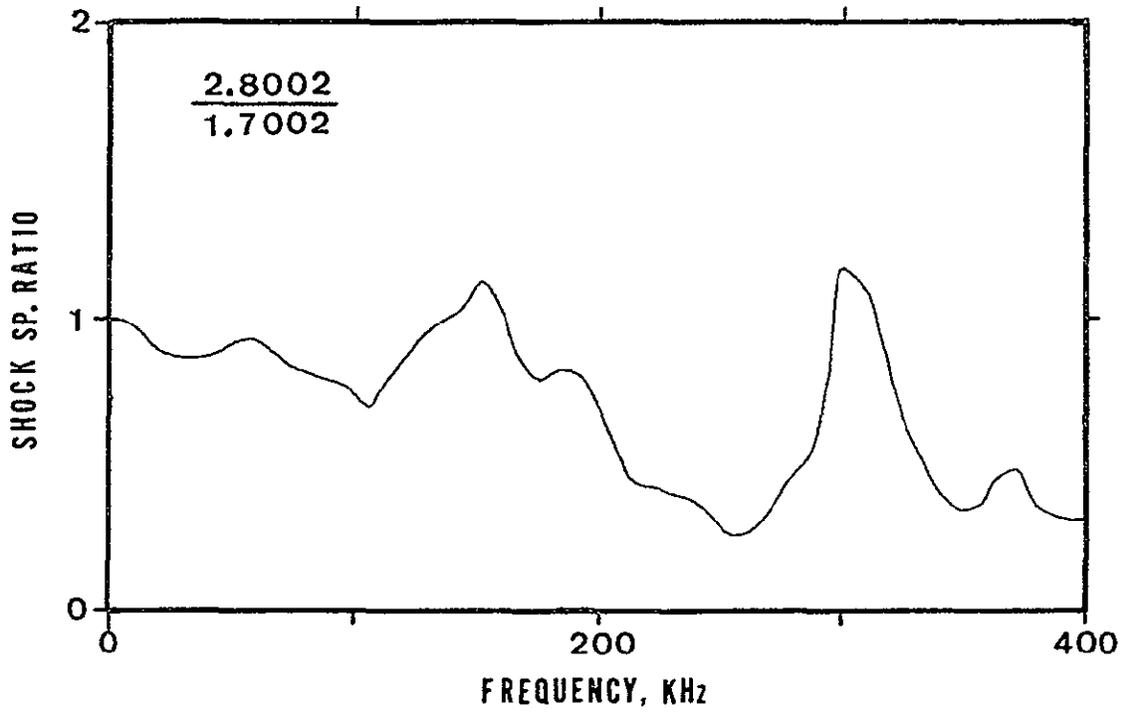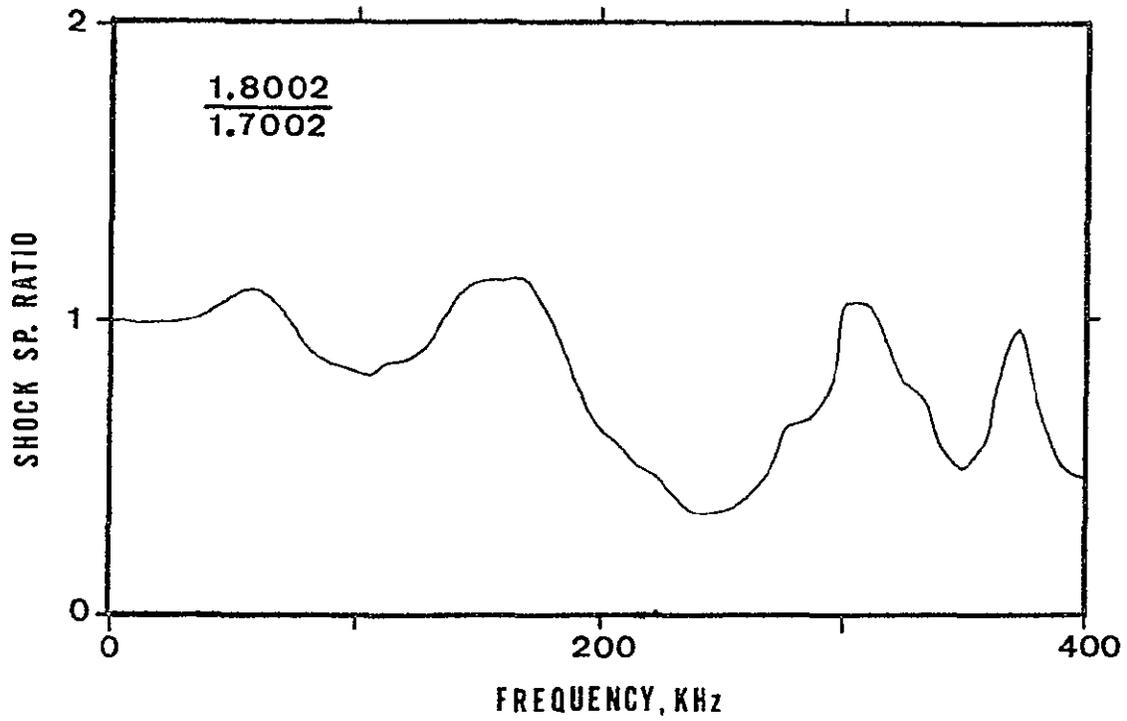
Fig. 69. Shock spectrum ratio of deconvoluted traces
of a bearing with a cut in the race relative to the trace in
Figure 61(b).
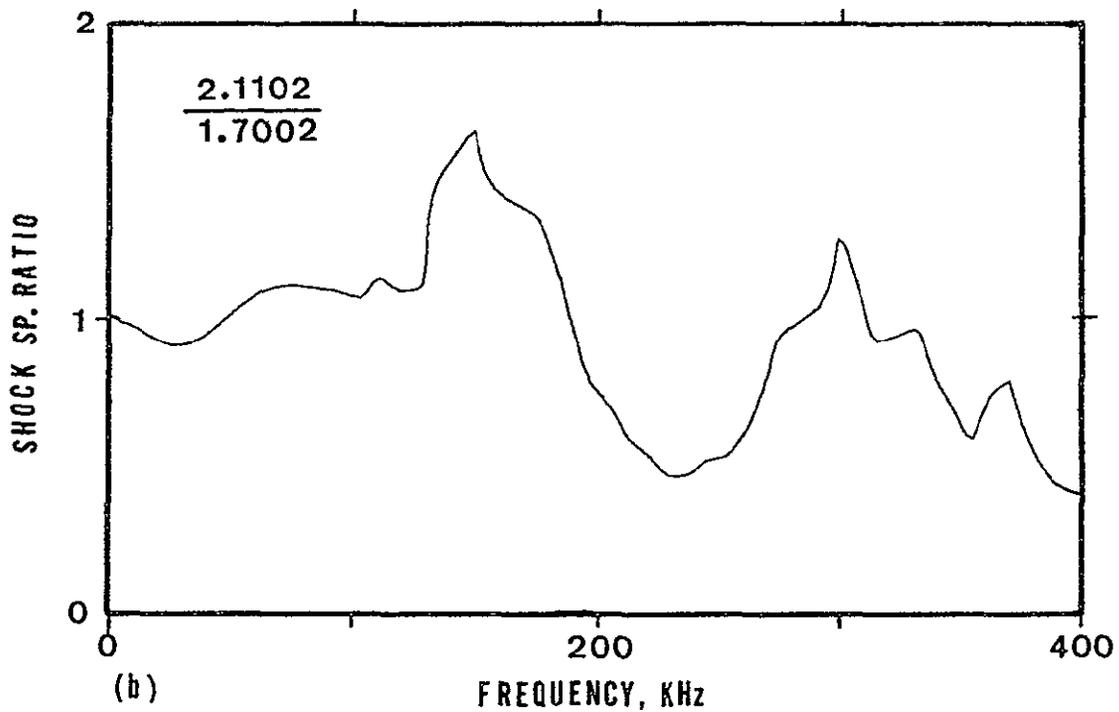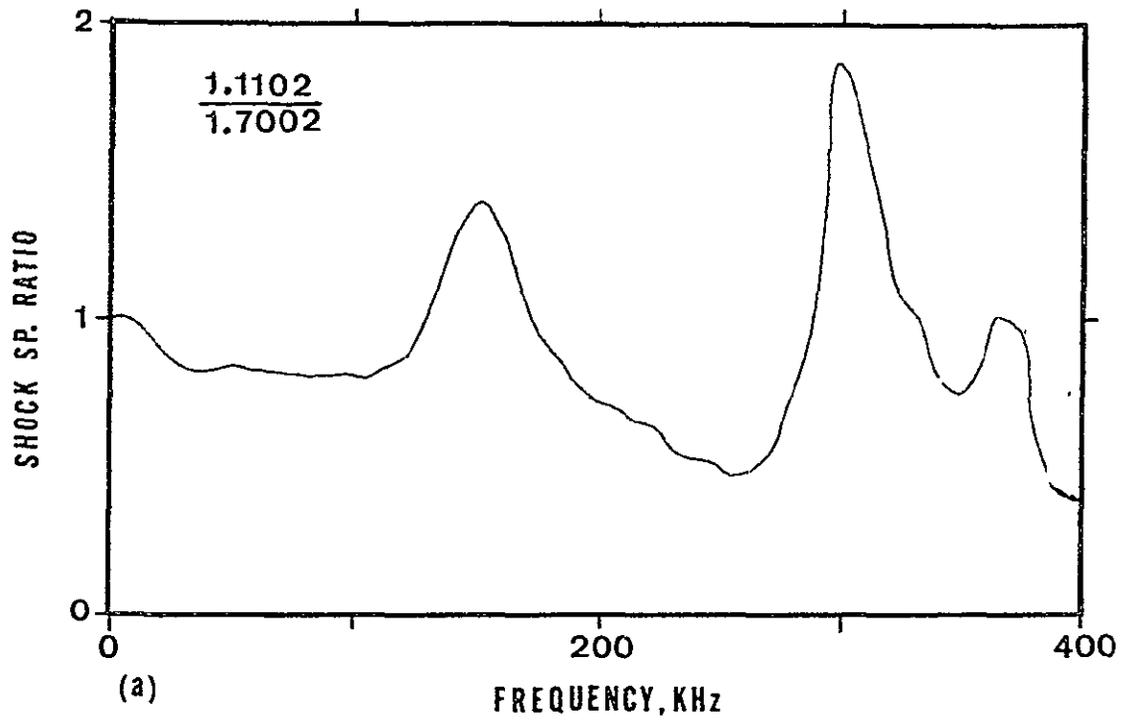
Fig. 70. Shock spectrum ratio of deconvoluted traces of a bearing with a cut in one ball relative to the trace in Figure 61(b).

(a)

(b)
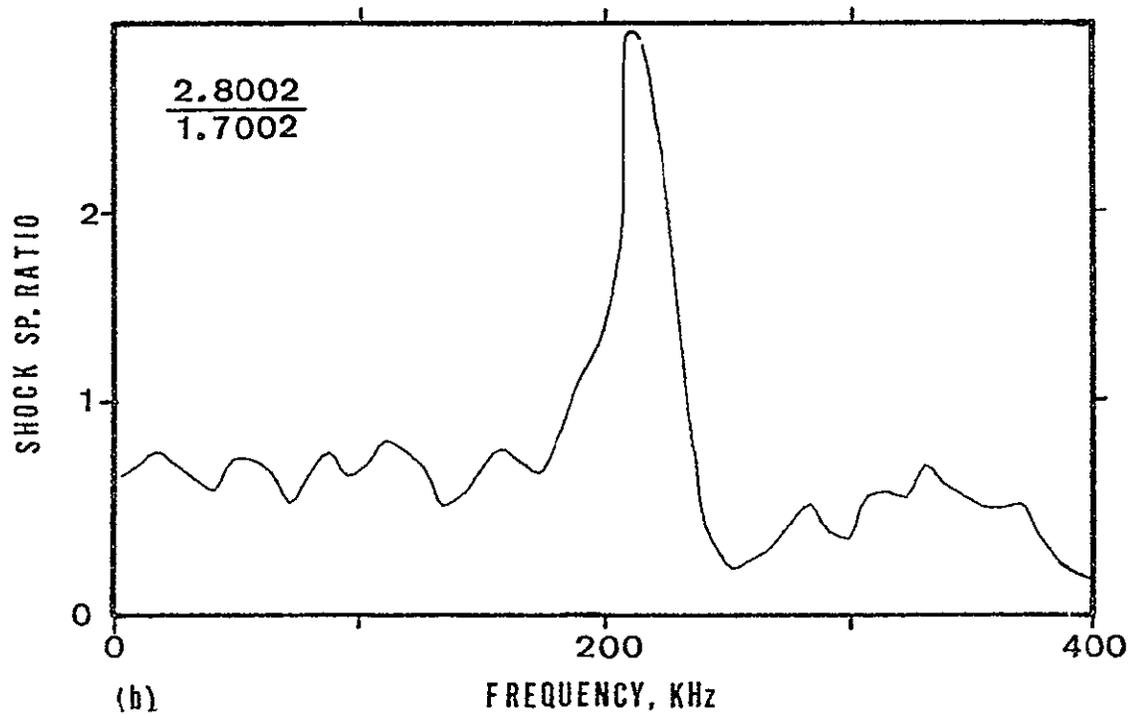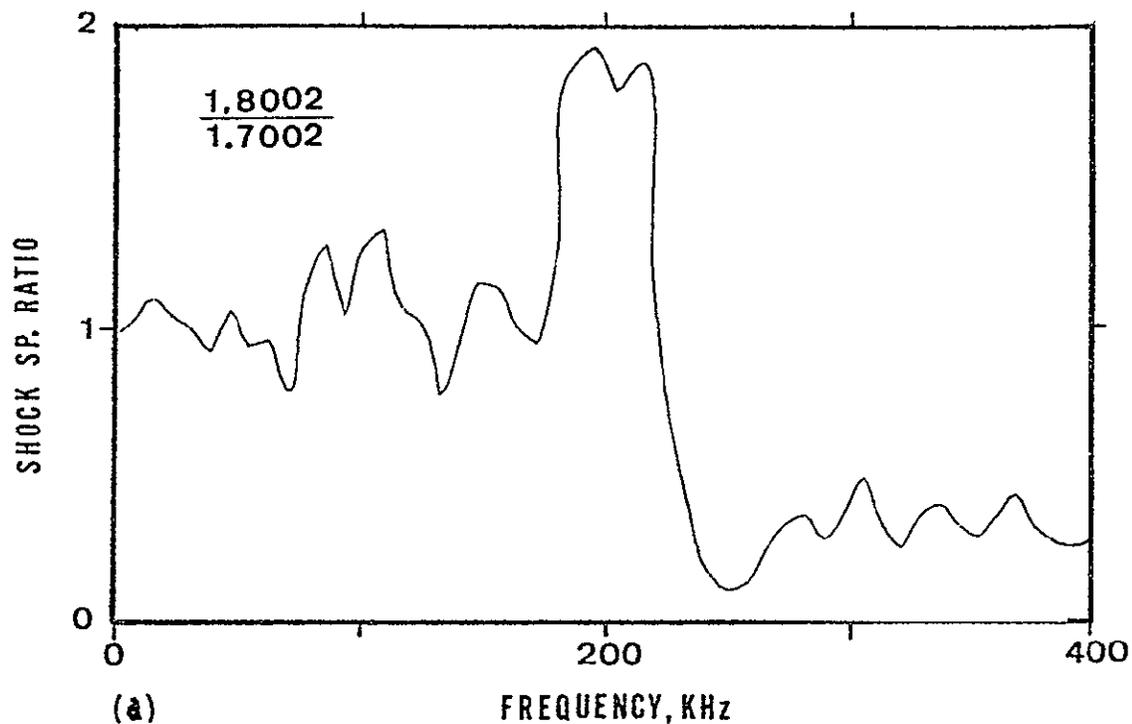
Fig. 71. Shock spectrum ratio of as-received traces of a bearing with a cut in the race relative to the trace in Figure 61(a).
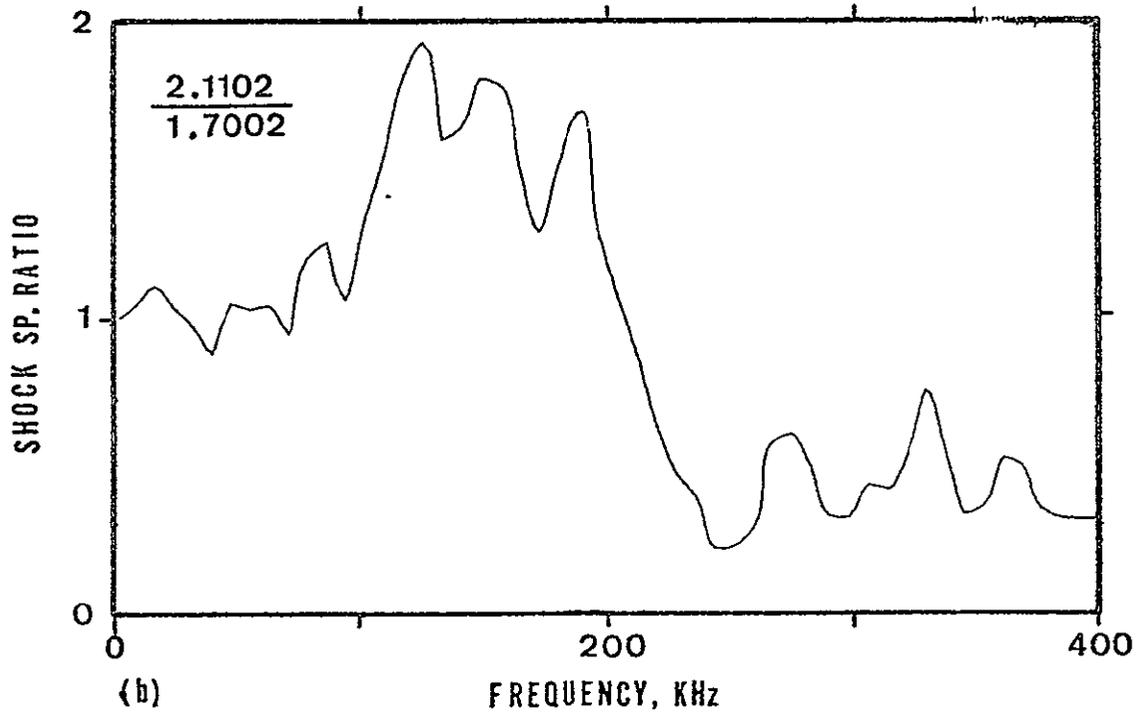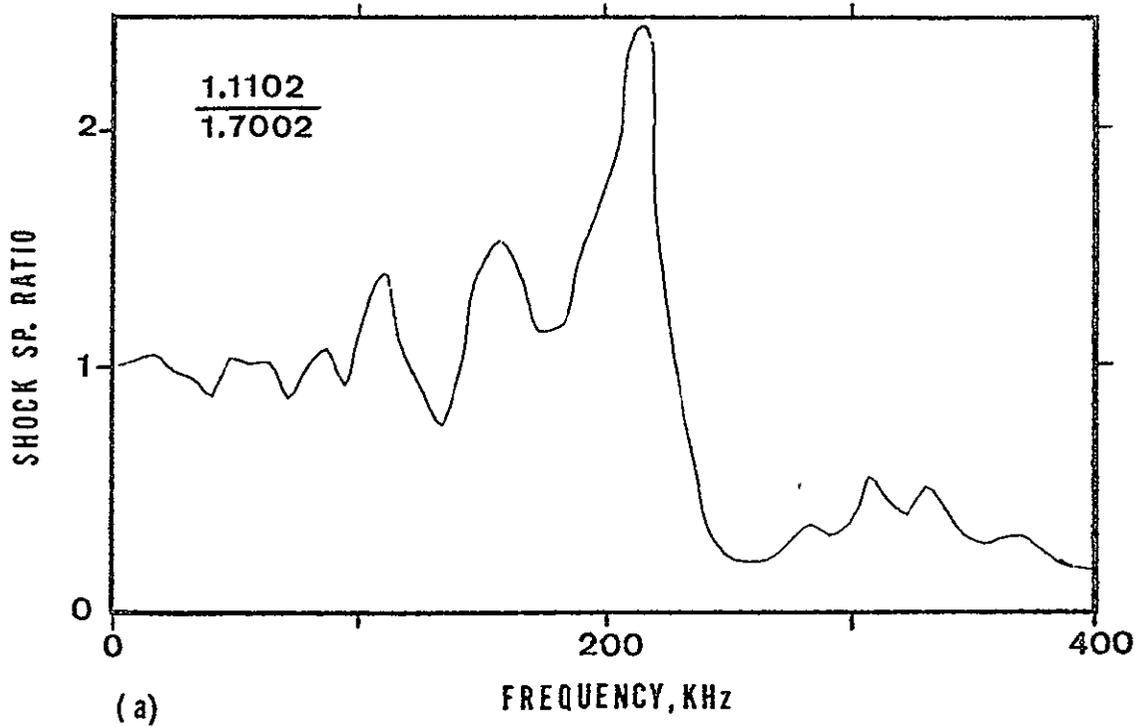
Fig. 72. Shock spectrum ratio of as-received traces of a bearing with a cut in one ball relative to the trace in Figure 61(a).

and its interaction with the high frequency electronic noise plus bearing noises.

The first moving bearing tests were for a good bearing running with an axle load of 700 lb_f. This load is equivalent to a B10 life of 8.8×10^6 cycles. Several AE type bursts could be detected above the steady state level of vibration signals coming from the bearing. Two of these signals have been presented in Figures 61 and 62. The steady state running signal level can be seen as well as the electronic noise in Figure (a). The deconvolution signal in (b) is larger than Z_1 in Figure 60 and the same large 450 kHz component is dominating the picture.

The second test was for a bearing with a slot cut in the race and the results for two AE signals taken from that test are shown in Figures 64 and 65. These tests were also conducted with a 700 lb_f axle load on the bearing. Notice in Figure (a) that the AE signal is significantly higher but the signature of the pulse in either Figure (b) or (c) is not particularly different from the undamaged bearing.

The last test was for a bearing with one ball cut and a load of 700 lb_f. Figures 66 and 67 show two AE signals, selected from the tape recording and the results are about as uninformative as the other tests.

It was pointed out in Chapter II that when there were small perturbations superimposed on a larger pulse, then the Fourier transform or the shock spectrum ratio might show the

presence of the perturbation. This technique of pulse signature analysis was tried on the ball bearing experiment and the results are shown in Figures 68 to 70. The first pair of shock spectra shows what might be expected for a good bearing AE signals. The spectrum seems to be uniform and approximately flat from 0 to 200 kHz. The shock spectrum ratio for the bearings with a crack in the race is shown in Figure 69 and there is a distinctive hump in the spectrum between 120 and 200 kHz. The shock spectrum for the tests of a crack in a ball relative to a good bearing acoustic emission is shown in Figure 70. The hump is in the same frequency band as was seen with the crack in the race but significantly higher.

To complete the argument, a computation of the shock spectrum ratio similar to the Figures 69 and 70 was made for the input signals Z_6 and the results are shown in Figures 71 and 72. From these results it is clear that deconvolution methods are necessary for cleaning up the signal before the methods of spectrum analysis can be applied to obtain meaningful results.

The contrast in the shock spectrum ratios for the deconvoluted traces and the as-received traces is significant. The shock spectrum ratios of the as-received pulses, Figures 71 and 72, show a high magnitude in the 200 kHz region which is near one of the transducer resonant frequencies, 180 kHz, but, other than this, none of the signatures is similar to

another. The shock spectrum ratios of the deconvoluted traces, Figures 69 and 70, are similar in shape and show enough individuality to indicate one type of AE source from another.

The significance is apparent when the shock spectrum ratio plots are superimposed as shown in Figure 73. The (a) part of Figure 73 is the shock spectrum ratios of the as-recorded acoustic emissions from the ball bearing experiments. A clean bearing result, 3.71, is also included in the (a) plot. Part (b) of Figure 73 is the shock spectrum ratios of the deconvoluted traces from the bearing experiments. The symbol identifications are the test numbers shown in the upper left corner of the plots, Figures 68 to 72.

There is a noticeable increase in the orderliness of the plots in Figure 73(b) compared to the plots in Figure 73(a). The most important feature about (b) is the peaks that occur at approximately 170 kHz. In this frequency zone there is a noticeable commonality of plots from the same experimental condition and there is a change in the peak height for different conditions. The two plots with the highest peaks are from tests with a cut in the ball; the two dotted plots with intermediate peak heights are from tests with a cut in the race; the two plots with low peaks are from the clean bearing. Note that there was some source of acoustic emissions from the clean bearing tests. It is significant that the shock spectrum ratio plots presented in
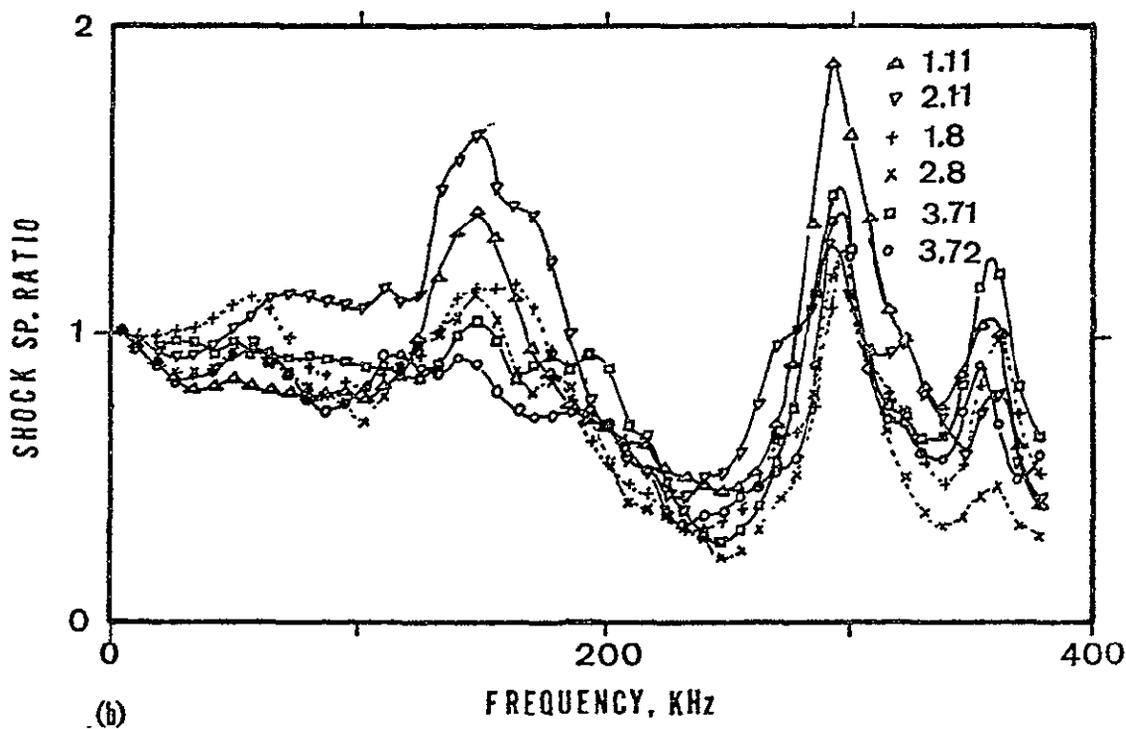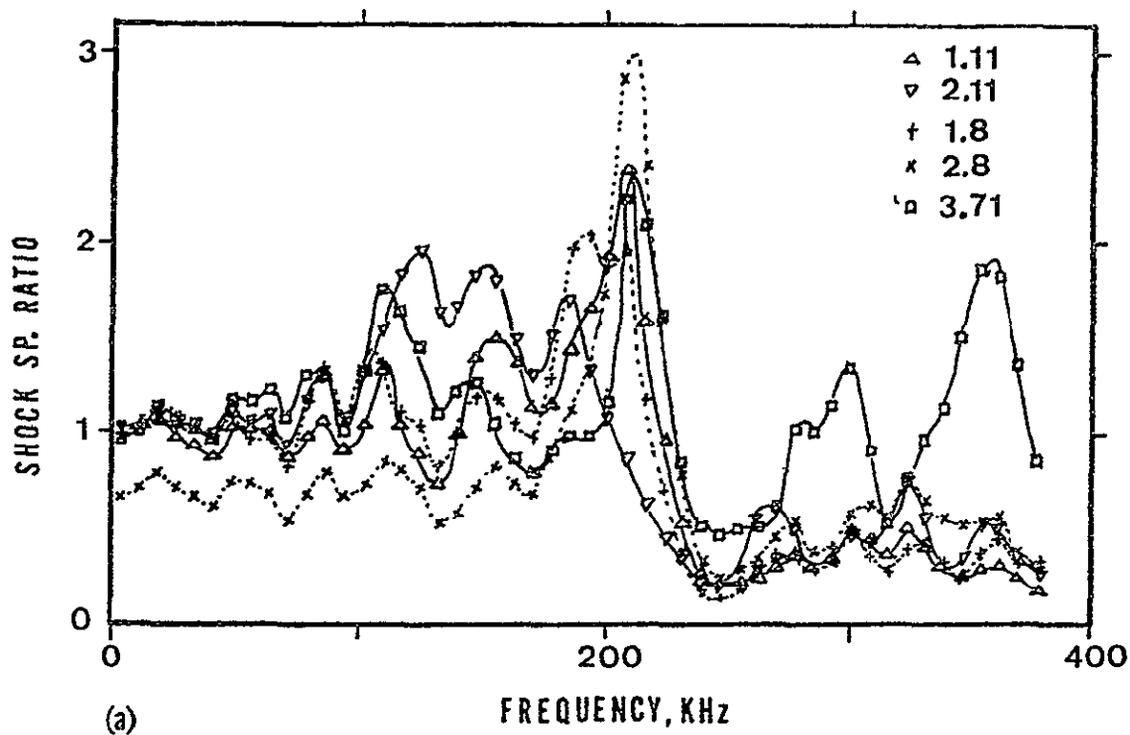
Fig. 73. Bearing tests: superimposed shock spectrum
a) as-received traces, b) deconvoluted traces.

Figure 10 of Chapter II indicated similar shapes for small perturbations on the side of a triangular pulse. The peak of the shock spectrum ratio changed in proportion to the perturbation height. It appears that the signature analysis of experimental pulses from known defects within the ball bearing is approaching the level of performance seen in the analytical studies.

In summary, the experimental studies have demonstrated that a technique for signature analysis has been developed that is capable of distinguishing between experimental acoustic emission sources.

CHAPTER V

CONCLUSIONS AND RECOMMENDATIONS

Based on the analytical and experimental program, the following conclusions can be drawn.

1. The output signal from a transducer-filter-measurement recording system for a family of differently shaped AE pulses cannot distinguish the height and shape of the pulses. The distinguishing characteristics of the Fourier spectrum for simple pulse shapes are modified significantly by passage of the pulse through the measurement system; thus the transducer-filter system is the major deterrent to the development of a definitive signature from AE signals emanating from defects.

2. For simple pulse shapes and measurement systems, the deconvolution process produces recognizable signals that relate to the input signals. Fourier transforms, shock spectra, Fourier transfer functions and shock spectrum ratios of deconvoluted pulses were useful methods for analysis of pulses. The shock spectrum ratio of deconvoluted pulses is the most useful for analyzing and comparing experimental pulses of all the signature analysis techniques examined.

3. Optimal design of transducer natural frequencies and filter corner frequencies did not appear to be essential for the particular deconvolution studies done for this research using the Dunegan/Endevco transducer for pulse analysis. However, the improvements that would occur in the deconvoluted traces when an optimal system is used are predicted to be significant. The optimal design study has shown that, for the best pulse shape deconvolution, the damping of the transducer should be substantially overdamped, the high-pass filter corner should be above the resonant frequency, and the transducer natural frequency should be more than six times the pulse width. At the present time, there is no manufacturer that can make an acoustic emission transducer to meet the optimized specifications.

4. With different transducers, deconvolution will display if the AE signals recorded are from a similar source. The lowest natural frequency of the transducer should be above approximately 50 kHz.

5. The spark discharge probe produces repeatable deconvoluted AE signals for transducer excitation. Various lengths of signal time from 10 to 200 μs were tried for examination of the deconvoluted signals. After approximately 40 μs from the initial rise, the signal height suddenly became two or more times larger, apparently from reinforcement of vibrations internal to the plate. After these large signals appeared, the similarity of the wave trains under

examination was lost. Thus it was concluded that the significant signature information is found in the first 40 µs of the spark discharge generated pulse.

6. Discrimination between different AE sources is possible when deconvolution of the signal trace is used. A steel ball dropping on a plate can be distinguished from a growing crack. A spark discharge AE signal has features that look like those of a crack growing. This may be due to the short time period which is common to these two AE sources. Without deconvolution, all three AE sources appear to be the same due to the dominant influence of the resonant frequencies in the transducer.

7. The ball bearing experiments demonstrated the problems with detecting an AE signal hidden in background noise. The deconvolution traces from different AE sources were all very similar. Signature analysis of the deconvoluted traces with the shock spectrum ratio method was shown to be capable of showing up the significant difference between the individual sources of AE. By superimposing the traces, a significant peak was found at one frequency which indicated the severity of the defect in the bearing.

Recommendations for Future Research

Experimental verification of models

A carefully controlled frequency response analysis of the different components in the measurement system needs to

be conducted. With a Bode amplitude and phase angle plot, it would be possible to select the number of poles and zeros required and the location of the corner frequencies. Square wave input signals could also be used and the output signal could be recorded on the digital event recorder. Then the deconvolution model could be fine-tuned to recreate the input wave shape.

Experiment with a known input
pulse shape

A measurement of the displacement wave form at the point where the acoustic emission transducer is located could be set up with a capacitance transducer as in Reference (23). Then the deconvoluted wave shape at the base of the transducer could be verified and the model parameters modified as indicated.

Finite element model of the
structure

A visco-elastic finite element model of the plate used for receiving acoustic emissions from a growing crack should be developed. The dynamic response of the plate with known boundary interactions could then be solved and a dynamic model could be created to approximate the results. This is a necessary step in building a model that will describe how a crack grows.

Optimization to find a model of
the structure

A set of arbitrarily selected poles, zeros, and complex
poles could be hypothesized as a structural model. Then,
with a defined input pulse shape and a well-defined output
pulse shape, the coefficients of the model could be moved
around until an optimum is found. The degree of complexity
of the model could be increased and/or decreased until the
lowest standard error of estimate was located. This may be
the method that will need to be perfected for use in deconvo-
lution signature analysis in nondestructive testing applica-
tions.

Deconvolution by analog computer

With an analog computer model of the deconvolution
equations, it should be possible to see the deconvolution
signature in real time. A digital memory oscilloscope is re-
quired to hold acoustic emission pulses for examination of
the leading edge of the pulse package. As soon as a pulse is
examined, the screen is cleared for the next available pulse.
This type of development will be valuable for practical ap-
plications in nondestructive testing.

Evaluation of digital event
recorder

More work is needed to determine the amplitude dis-
tortions and the additional frequencies that have been added
to the data by the presence of a digital event recorder.

Would there be a significant improvement in the deconvolution result if an analog to digital converter of increased accuracy is used? Can the influence of the digitizer steps be modeled and deconvoluted adequately out of the data? These are some of the questions about digitization of data that have been partially addresssed in this work, but a more detailed study should be conducted.

Transducer for pulse recording

Design and build a transducer with the optimum damping and natural frequency. Test this transducer alongside of an acoustic emission pulse counting transducer and determine if the results would justify another transducer for pulse signature analysis.

APPENDIX 1

SOLUTION OF ORDINARY DIFFERENTIAL EQUATIONS
BY NUMERICAL METHODS

The construction of a mathematical model for most
dynamic processes begins with the formulation of the dif-
ferential equation of motion. In cases involving transient
motion or a pulse-like signal, ordinary differential equa-
tions are sufficient for the model for the description of
the system. The solution when transients are the inputs to
dynamical systems is known for many second and third order
differential equations when the pulse is reduced to simple
geometrical segments. But, in general, the solution of a
differential equation for the dynamic outputs given a random
input pulse shape is difficult to obtain by classical cal-
culus techniques. Fortunately there are numerical methods
which can be used to solve ordinary differential equations,
and there is no restriction on the configuration of the
input forcing function.

Numerical solutions of differential equations are
approximations and the results will be subject to trunca-
tion errors, stability of the solution and step size selec-
tion. The numerical technique used for this work on pulse
analysis is a predictor-corrector version of the Runge-Kutta

Preceding page blank

method. It was developed to provide accuracies equivalent to using the higher order terms of Taylor's expansion of a differential equation with less computation.

A Runge-Kutta method attributed to Gill (20) was used with a modification by the author. Gill's equations are a single step method with an intermediate calculation at half way across the step. The Runge-Kutta subroutines in many computer-program libraries employ the equations with Gill constants. The equation for calculation of $Z_{i+1}(t,X,Z)$ at one step ahead of Z_i (h and dt are the step increment) is as follows:

$$Z_{i+1} = Z_i + h/6 \ (K_1 + 2G_1K_2 + 2G_2K_3 + K_4) \tag{24}$$

where:

h = step size along t axis, dt

G_1 = first Gill constant

  $= 1 - 1/(2)^{\frac{1}{2}}$

G_2 = second Gill constant

  $= 1 + 1/(2)^{\frac{1}{2}}$

$K_1 = f(t_i, \ X_i, \ Z_i)$, functional expression for the highest derivative in the differential equation to be solved

$K_2 = f(t_i + h/2, \ X_{i+\frac{1}{2}}, \ Z_i + K_1h/2)$

$K_3 = f(t_i + h/2, \ X_{i+\frac{1}{2}}, \ Z_i + (G_2 - 3/2) \ K_1h + G_1K_2h)$

$K_4 = f(t_i + h, \ X_{i+1}, \ Z_i - K_2h/2^{\frac{1}{2}} + G_2K_3h)$

X_i = forcing function at beginning of step

X_{i+1} = forcing function at end of step

$X_{i+\frac{1}{2}} = (X_i + X_{i+1})/2$

In the first trials with numerical solutions of differential equations with a forcing function, the value of X in the function $f(t,X,Z)$ was fixed at the beginning of the step. That is to say, as the next step i+1 was calculated, the driving function term X in the K_1, K_2, K_3 and K_4 terms defined above was fixed at the X_i value. Trial runs were made on the following differential equation:

$$\frac{Z}{X} = \frac{D^n}{(D^2 + 2\zeta\omega D + \omega^2)(D + \omega_{hp})^n} \tag{25}$$

where:

D = the differential operator d/dt

n = integer powers, i.e., 0, 1, 2, ...

$\zeta, \omega, \omega_{hp}$ = constants of the equation.

Deconvolutions of the differential equation were calculated next, and the results were compared with the input driving function shape X. The comparison was made by calculating the standard error of estimate, TDEV, as mentioned in Chapter III. These trial runs were made for square, triangular, and cosine shaped input pulses with the differential equation shown in equation (25). The equations that were selected for numerical differentiation were the central difference form, and they are listed in Table 4. Note that for the eighth

TABLE 4

EQUATIONS FOR DIFFERENTIATION OF INPUT FUNCTIONS
FOR RUNGE-KUTTA ALGORITHM

Derivative	Equation (Derivative centered around point i)
dx/dt	$(X_{i+1} - X_{i-1})/2\Delta t$
d^2x/dt^2	$(X_{i+1} - 2X_i + X_{i-1})/\Delta t^2$
d^3x/dt^3	$(X_{i+2} - 2X_{i+1} + 2X_{i-1} - X_{i-2})/2\Delta t^3$
d^4x/dt^4	$(X_{i+2} - 4X_{i+1} + 6X_i - 4X_{i-1} + X_{i-2})/\Delta t^4$
d^5x/dt^5	$(X_{i+3} - 4X_{i+2} + 5X_{i+1} - 5X_{i-1} + 4X_{i-2}$ $- X_{i-3})/2\Delta t^5$
d^6x/dt^6	$(X_{i+3} - 6X_{i+2} + 15X_{i+1} - 20X_i + 15X_{i-1} - 6X_{i-2}$ $+ X_{i-3})/\Delta t^6$
d^7x/dt^7	$(X_{i+4} - 6X_{i+3} + 14X_{i+2} - 14X_{i+1} + 14X_{i-1}$ $- 14X_{i-2} + 6X_{i-3} - X_{i-4})/2\Delta t^7$
d^8x/dt^8	$(X_{i+4} - 8X_{i+3} + 28X_{i+2} - 56X_{i+1} + 70X_i$ $- 56X_{i-1} + 28X_{i-2} - 8X_{i-3} + X_{i-4})/\Delta t^8$

derivative, the function needs to be defined four steps in front of the point i and four steps behind. The results of the first trial for six cases are shown in Table 5.

The modification that was incorporated into Gill's equations is the changes in the driving function term X. Examination of the terms K_1, K_2 etc. indicates that the differential equation and its integrals are solved at four locations as follows: 1) at the present step i, K_1; 2) at a step half way across the increment length with a correction to Z_1, K_2; 3) at the same half-way location with a second correction to Z_i, K_3; and 4) at the next step location i+1 with a third correction to Z_i, K_4. After considerable data analysis it became clear that the calculation of K_2, K_3 and K_4 would be better predictions of the values at the i+½ and i+1 locations if the forcing function part, X_i, of Z_i was permitted to change. The changes were the average value of X_i and X_{i+1} at the i+½ location and the X_{i+1} value in the K_4 calculation. It was noted that the time term,- t, changes in a similar manner in the K_2, K_3 and K_4 calculations. This relatively simple change in point of view as to how the driving function is treated had a dramatic effect on the results.

The results of the final runs with the modification of the Gill's equations is shown in Table 6 for selected cases. With the changing of X in the calculation of the K's in equation (24), the TDEV calculation for a cosine pulse input

TABLE 5

STANDARD ERROR OF ESTIMATE FOR DIFFERENTIAL EQUATION SOLVER
AND DECONVOLUTION ALGORITHM WITH GILL'S EQUATIONS

n	ζ	f_{hp}/f_n	TDEV		
			Cosine	Square	Triangle
0	0.01	0.1	0.006238	0.03709	0.005640
1	0.01	0.1	0.01250	0.05588	0.01119
2	0.01	0.1	0.01243	0.05579	0.01256
3	0.01	0.1	0.01247	0.05539	0.01117
5	0.01	0.1	0.01253	0.05537	0.01123
6	0.01	0.1	0.01254	0.05350	0.01120
0	1.66	1.45	0.005894	0.02606	0.005273
1	1.66	1.45	0.01276	0.06212	0.01144
2	1.66	1.45	0.01239	0.05797	0.01109
3	1.66	1.45	0.01256	0.05546	0.01123
5	1.66	1.45	0.01253	0.05509	0.01121
6	1.66	1.45	0.01251	0.05660	0.01122

Note 1.   Pulse length, $f_n T_p = 8.0$; increment size,
$\Delta t f_n = 0.1$.

Note 2.   All calculations for n greater than 2 must be
done in double precision.

TABLE 6

STANDARD ERROR OF ESTIMATE FOR DIFFERENTIAL EQUATION SOLVER
AND DECONVOLUTION ALGORITHM FOR EQUATION (25)

| n | ζ | f_{hp}/f_n | TDEV | | |
			Cosine	Square	Triangle
0	0.01	0.1	0.0001060	0.02049	0.0006679
1	0.01	0.1	0.0002916	0.03138	0.001067
2	0.01	0.1	0.0004053	0.03417	0.001100
3	0.01	0.1	0.0005310	0.03719	0.001470
5	0.01	0.1	0.0007273	0.03927	0.001661
6	0.01	0.1	0.0006546	0.03810	0.001593
0	1.66	1.45	0.0001216	0.01537	0.0005176
1	1.66	1.45	0.0002335	0.02625	0.0008320
2	1.66	1.45	0.0003152	0.03020	0.0009995
3	1.66	1.45	0.0004904	0.03467	0.001295
5	1.66	1.45	0.0005937	0.03596	0.001438
6	1.66	1.45	0.0005330	0.03610	0.001380

Note 1. Pulse length, $f_n T_p = 8.0$; increment size, $\Delta t f_n = 0.1$.

Note 2. All calculations for n greater than 1 must be done in double precision.

improved by a factor of 50:1, and, for a triangular and a square pulse, the improvement was 12:1 and 2:1 respectively.

[▼] One significant reason for the improvement in the results is the influence of phase shift on the TDEV results. This modification of Gill's equations has solved most of the phase shift problems between the input pulse and the deconvolution pulse and thus there was a significant lowering of the TDEV results for the cosine and the triangular pulses.

The square pulse test did not show as good an improvement in TDEV with the modified equations because of the large error of estimate in the ±2 increments on either side of the step changes. Thus, for square pulses, the TDEV is primarily a function of the increment step size of the computation.

A sample of the computer subroutines used in Fortran IV language to solve a differential equation is shown in Figures 74 and 75.

```
0001          SUBROUTINE RKGILL(X,XMAX,Y,XINCR,M,N,C,IMAX,IFUNCT,Z1)
0002          INTEGER LP,CR
0003          DIMENSION C(1),X(1),Z1(1),YC(10),F(10) ,Y(500,6)
0004          COMMON LP,CR,DT,TPULSE
0005          J = 2
0006          XC = X(1)
0007          DO 5 I = 1,N
0008      5   YC(I) = Y(1,I)
0009      8   IF (XC - XMAX ) 6,6,7
0010      6   CALL RUNGE (N,YC,F,XC,XINCR,M,K)
0011          GO TO (10,20),K
0012      10  CONTINUE           -
0013          GO TO (101,102,103,104,105),IFUNCT
0014      101 CALL FUNCT1(J,M,C,YC,FHIGHD,Z1,IMAX)
0015          GO TO 30
0016      102 CALL FUNCT2(J,M,C,YC,FHIGHD,Z1,IMAX)
0017          GO TO 30
0018      103 CALL FUNCT3(J,M,C,YC,FHIGHD,Z1,IMAX)
0019          GO TO 30
0020      104 OUTPUT 'FUCTION 4 MISSING'
0021          CALL EXIT
0022      105 CALL FUNCT5(J,M,C,YC,FHIGHD,Z1,IMAX)
0023      30  CONTINUE
0024          F(1) = FHIGHD
0025          DO 15 I = 2,N
0026      15  F(I) = YC(I-1)
0027          GO TO 6   ‥
0028      20  DO 25 I = 1,N
0029      25  Y(J,I) = YC(I)
0030          X(J) = XC
0031          J = J + 1
0032          GO TO 8
0033      7   CONTINUE
0034          RETURN
0035          END


0001          SUBROUTINE RUNGE (N,Y,F,X,H,M,K)
0002      C   THIS ROUTINE PERFORMS RUNGE-KUTTA CALCULATIONS BY GILLS METHOD
0003          DIMENSION Y(1),F(1),Q(10)
0004          M = M + 1
0005          GO TO (1,4,5,3,7),M
0006      1   DO 2 I = 1,N
0007      2   Q(I) = 0.0
0008          A = 0.5
0009          GO TO 9
0010      C   A = 1. + 1./(2)**0.5   ----SECOND GILLS CONSTANT
0011      3   A = 1.7071067811865475244
0012      4   X = X + 0.5*H
0013      5   DO 6 I = 1,N
0014          Y(I) = Y(I) + A*(F(I)*H - Q(I) )
0015      6   Q(I) = 2.*A*H*F(I) + (1. - 3.*A)*Q(I)
0016      C   A = 1. - 1./SQRT(2.) ----  FIRST GILLS CONSTANT
0017          A = 0.292832188134524756
0018          GO TO 9
0019      7   DO 8 I = 1,N
0020      8   Y(I) = Y(I) + H*F(I)/6. - Q(I)/3.
0021          M = 0
0022          K = 2
0023          GO TO 10
0024      9   K = 1
0025      10  RETURN
0026          END
```

Fig. 74. Subroutines, R.K. Gill and Runge

```
0001                SUBROUTINE LPFILT(C,N,X,Z2,ZDECCN)
0002                INTEGER CR,LP
0003                DIMENSION C(1),X(1),Z2(1),ZDECCN(1)
0004                COMMON LP,CR,DT,TPULSE, Y(500,6)
0005                FLPASS = 300000.0
0006                WL = FLPASS*6.283185
0007                WLTH = 8.*WL
0008                ZLP = 0.05
0009                ZLP = 0.2
0010                C(1) = 2.*(1.+ZLP)/(WL*WL*WL)
0011                C(2) = 2.*(1.+2.*ZLP)/(WL*WL)
0012                C(3) = 2.*(1.+ZLP)/WL
0013                C(4) = 1.0
0014                C(5) = WL*WL*WL*WL
0015                C(6) = 1./(WLTH**4.)
0016                C(7) = 4./(WLTH**3.)
0017                C(8) = 6./(WLTH*WLTH)
0018                C(9) = 4./WLTH
0019                IFUNCT = 5
0020                DO 5 I = 1,10
0021      5         ZDECON(I) = 0.0
0022                NM5 = N - 5
0023                DO 8 I = NM5,N
0024      8         ZDECON(I) = 0.0
0025                XMAX = X(N)
0026                M = 0
0027                NVAR = 4
0028                DO 10 J=1,NVAR
0029      10        Y(1,J) = 0.0
0030                CALL RKGILL(X,XMAX,Y,DT,M,NVAR,C,N,IFUNCT,Z2)
0031                DO 20 I = 1,N
0032      20        ZDECON(I) = Y(I,4)
0033                NM20 = N - 20
0034                DO 40 I = NM20,N
0035      40        ZDECON(I) = 0.0
0036                OUTPUT FLPASS   ,ZLP
0037                RETURN
0038                END
```

Fig. 75. Subroutine low-pass filter

```
0001              SUBROUTINE FUNCT5(J,M,C,Y,F,Z2,N)
0002              DIMENSION C(1),Y(1),Z2(1)
0003              INTEGER LP,CR
0004              COMMON LP,CR,DT
0005              I = J - 1
0006              NM5 = N- 5
0007              IF(I.LE.5) I = 5
0008              IF(I.GE.NM5) I = NM5
0009              Z2D1C= (Z2(I+1) - Z2(I-1))/(2.*DT)
0010              Z2D2C=(Z2(I+1) - 2.*Z2(I) +Z2(I-1))/(DT*DT)
0011              Z2D3C= (Z2(I+2)-2.*Z2(I+1)+2.*Z2(I-1)-Z2(I-2))/(2.*DT**3.)
0012              Z2D4C= (Z2(I+2)-4.*Z2(I+1)+6.*Z2(I)-4.*Z2(I-1)+Z2(I-2))/DT**4.
0013              Z2D1C1 = (Z2(I+2) - Z2(I))/(2.*DT)
0014              Z2D2C1 = (Z2(I+2) - 2.*Z2(I+1) +Z2(I))/(DT*DT)
0015              Z2D3C1 =(Z2(I+3)-2.*Z2(I+2)+2.*Z2(I)-Z2(I-1))/(2.*DT**3.)
0016              Z2D4C1 = (Z2(I+3)-4.*Z2(I+2)+6.*Z2(I+1)-4.*Z2(I)+Z2(I-1))/DT**4.
0017    C    THREE DIFFERENTIAL STEPS FOR R-KUTTA
0018              Z2ONE = Z2D4C *C(6) + Z2D3C *C(7)+Z2D2C *C(8)+Z2D1C *C(9) + Z2(I)
0019              Z2THRE =Z2D4C1*C(6) + Z2D3C1*C(7)+Z2D2C1*C(8)+Z2D1C1*C(9)+Z2(I+1)
0020              Z2ONE = Z2(I)
0021              Z2THRE = Z2(I+1)
0022              Z2TWO = (Z2ONE + Z2THRE)*C.5
0023              GO TO (1,2,2,3),M
0024    1         F = C(5)*(Z2ONE  -C(1)*Y(1) - C(2)*Y(2) - C(3)*Y(3) - C(4)*Y(4))
0025              GO TO 5
0026    2         F = C(5)*(Z2TWO  -C(1)*Y(1) - C(2)*Y(2) - C(3)*Y(3) - C(4)*Y(4))
0027              GO TO 5
0028    3         F = C(5)*(Z2THRE -C(1)*Y(1) - C(2)*Y(2) - C(3)*Y(3) - C(4)*Y(4))
0029    5         RETURN
0030              END
```

Fig. 75. Continued.

```
0001            SUBROUTINE FUNCT5(J,M,C,Y,F,Z2,N)
0002            DIMENSION C(1),Y(1),Z2(1)
0003            INTEGER LP,CR
0004            COMMON LP,CR,DT
0005            I = J - 1
0006            NM5 = N- 5
0007            IF(I.LE.5) I = 5
0008            IF(I.GE.NM5) I = NM5
0009            Z2D1C= (Z2(I+1) - Z2(I-1))/(2.*DT)
0010            Z2D2C=(Z2(I+1) - 2.*Z2(I) +Z2(I-1))/(DT*DT)
0011            Z2D3C= (Z2(I+2)-2.*Z2(I+1)+2.*Z2(I-1)-Z2(I-2))/(2.*DT**3.)
0012            Z2D4C= (Z2(I+2)-4.*Z2(I+1)+6.*Z2(I)-4.*Z2(I-1)+Z2(I-2))/DT**4.
0013            Z2D1C1 = (Z2(I+2) - Z2(I))/(2.*DT)
0014            Z2D2C1 = (Z2(I+2) - 2.*Z2(I+1) +Z2(I))/(DT*DT)
0015            Z2D3C1 =(Z2(I+3)-2.*Z2(I+2)+2.*Z2(I)-Z2(I-1))/(2.*DT**3.)
0016            Z2D4C1 = (Z2(I+3)-4.*Z2(I+2)+6.*Z2(I+1)-4.*Z2(I)+Z2(I-1))/DT**4.
0017     C    THREE DIFFERENTIAL STEPS FOR R-KUTTA
0018            Z2ONE = Z2D4C *C(6) + Z2D3C *C(7)+Z2D2C *C(8)+Z2D1C *C(9) + Z2(I)
0019            Z2THRE =Z2D4C1*C(6) + Z2D3C1*C(7)+Z2D2C1*C(8)+Z2D1C1*C(9)+Z2(I+1)
0020            Z2ONE = Z2(I)
0021            Z2THRE = Z2(I+1)
0022            Z2TWO = (Z2ONE + Z2THRE)*C.5
0023            GO TO (1,2,2,3),M
0024     1      F = C(5)*(Z2ONE  -C(1)*Y(1) - C(2)*Y(2) - C(3)*Y(3) - C(4)*Y(4))
0025            GO TO 5
0026     2      F = C(5)*(Z2TWO  -C(1)*Y(1) - C(2)*Y(2) - C(3)*Y(3) - C(4)*Y(4))
0027            GO TO 5
0028     3      F = C(5)*(Z2THRE -C(1)*Y(1) - C(2)*Y(2) - C(3)*Y(3) - C(4)*Y(4))
0029     5      RETURN
0030            END
```

Fig. 75. Continued.

REFERENCES

1. Southworth, H.L., Steele, N.W. and Torelli, P.P. "Practical Sensitivity Limits of Production Nondestructive Testing Methods in Aluminum and Steel," AFML-TR-74-241, March, 1975.

2. Packman, P.F. "Status of Nondestructive Inspection Techniques with Special Reference to Welding Defects," in Significance of Defects in Welded Structures, Kanazawa T. and Kobayasi, A.S. eds., Proceedings of the Japan-U.S. Seminar 1973, Tokyo, University of Tokyo Press, 1974.

3. Liptai, R.G., Harris, D.O., Engle, R.B. and Tatro, C.A. "Acoustic Emission Techniques in Materials Research," Int. J. of NDT, 1971, vol. 3, pp 215-275.

4. Kaiser, J. "Untersuchugen uber das auftreten Geranshen beim Zugversuch," Ph.d Dissertation, Technische Hochoschule, Munich, 1950.

5. Schoefield, B.H. "Acoustic Emission under Applied Stress," WADC Technical Report, 1958.

6. Schoefield, B.H. "Acoustic Emission under Applied Stress," Technical Report No. ASD-TDR-63-509, Part I, Part II, 1964.

7. Chugh, Y.P., Hardy, H.R., and Stefanka, R. "An Investigation of the Frequency Spectra of Microsesmic Activity in Rock under Tension," Tenth Symposium on Rock Mechanics, The University of Texas, Austin, 1968.

8. Graham, L.J. and Alers, G.A. "Frequency Spectra of Acoustic Emissions Generated by Deforming Metals and Ceramics," IEEE Ultrasonic Symposium, Boston, 1972.

9. Graham, L.J. and Alers, G.A. "Spectrum Analysis of Acoustic Emission in A533-B Steel," Presented at ASNT Meeting, Los Angeles, 1973.

10. Ono, K., Stern, R., and Long, M. "Application of Correlation Analysis to Acoustic Emission," ASTM STP 505, 1973.

11. Beattie, A.G. "An Analysis of the Frequency and Energy Characteristics of Acoustic Emission Signals from Tensile and Structural Tests," SESA Spring Meeting, Chicago, 1975.

12. Liptai, R.G., Harris, D.O. and Tatro, C.A. _Acoustic Emission_, ASTM Special Technical Publication ASTM-STP 505, Philadelphia, 1972.

13. Dunegan, H.L., Harris, D.O. "Acoustic Emission Techniques," _Ultrasonics_, vol. 7, No. 3, 1969.

14. Dunegan, H.L., Harris, D.O. and Tatro, C.A. "Fracture Analysis by Use of Acoustic Emission," Eng. Fract. Mech., VI, No. 1, 1968, p. 105.

15. Clements, W.C.,Jr. and Schnelle, K.B.,Jr. "Mathematical Modeling of Dynamic Systems with Applications to Non-Ideal Systems," Technical Report No. 24, Environmental and Water Resources Engineering, Vanderbilt University, 1969.

16. Stockton, R.L. and Packman, P.F. "Analysis of Signals Associated with Defects Growing from Fastener Holes by Eddy Current Testing," Presented at ASM Fall Meeting, Detroit, 1974.

17. Packman, P.F. "Ultrasonic Indica Analysis." ARPA/AFML Workshop in _Advanced NDT_, AFML TR F4-238, Rockwell Int., 1974.

18. Thompson, W.T. _Vibration Theory and Applications_, Prentice Hall, N.J., 1965.

19. Houghton, J.R. "The Influence of Material Damping on a Shock Spectrum," ORNL Progress Report, Feb., 1975.

20. Carnahan, B., Luthur, H.A. and Wilkes, J.O. _Applied Numerical Methods_, J. Wiley, New York, 1969, pp 361-366.

21. Harris, C.M. and Crede, C.E. _Shock Vibration Handbook_, McGraw-Hill, N.Y., 1961, pp 12-18.

22. Fletcher, R. and Powell, M.J.D. "A Rapidly Convergent Descent Method for Minimization," _Computer J._, Vol. 6, 1963, pp 163-168.

23. Breckenridge, F.R., Tschiegg, C.E. and Greenspan, M. "Acoustic Emission: Some Applications of Lamb's Problem," _J. Acoust. Soc. Am._, V57, No. 3, March 1975, pp 626-631.

24. Bell, R.L. "Acoustic Emission Transducer Calibration:
    Transient Pulse Method," Paper presented at 32nd,
    Fall Conference of the American Society for Non-
    destructive Testing, October 1972 (Available from
    Dunegan/Endevco Corp.).

25. Feng, C.C. "Acoustic Emission Calibration: Spark
    Impulse Calibration Method," Engineering Report
    No. 74-7-C, Endevco Corporation, San Juan Capis-
    trano, September 1974.